UNIVERSITÀ DEGLI STUDI DI MILANO
Scuola di Dottorato in Scienze Biologiche e Molecolari
XXVI Ciclo

Smpx-deficient zebrafish embryos: a tool for studying ciliopathies and deafness

Anna Ghilardi
PhD Thesis

Scientific tutor: Dr. Luca Del Giacco

Academic year: 2013/2014

SSD: BIO/06

Thesis performed at the Biosciences Department of the University of Milan

Contents

Part I

Abstract

Firmly established as a model organism for embryonic developmental studies, zebrafish is now emerging as an effective system to elucidate the fundamental aspects of several human diseases. Despite the significant evolutionary distance, gene functions and pathways are often highly conserved between zebrafish and humans. Previous work has identified nonsense mutations, associated with hearing deficiency, in the *small muscle protein, X-linked (SMPX)* gene and a loss-of-function mechanism underlying this form of impairment has been proposed. *SMPX* encodes a cytoskeleton-associated protein that has been suggested being responsive to mechanical stress. The presence of *Smpx* in hair cells of the murine cochlea reinforces the thesis of its importance in ear functioning.

In this study we first provided an overview of the expression of *smpx* during zebrafish embryonic development. We showed that from the 4-somite stage, zebrafish *smpx* was first expressed in the ciliated organ Kupffer's vesicle (KV), responsible for the left-right organs asymmetry, and then, as in mammals, expressed in the heart and in the inner ear, among other territories. Knock-down of *smpx* in zebrafish embryos resulted in the reduced number of cilia in KV and, consequently, the left-right patterning of internal organs resulted compromised, mimicking human heterotaxy, a disorder of laterality. Moreover, *smpx* knock-down resulted in the marked decrease of the number of cilia in the ear macular regions, providing a possible explanation for the hearing loss in *SMPX*-mutated patients.

In conclusion, this study contributes to the comprehension of the link between *SMPX* and human hearing loss, delivers a novel heterotaxy-candidate gene, and finally provides a robust animal tool for the future elucidation of the mechanisms behind both deafness/hearing loss and heterotaxy.

State of the art

Cilia and ciliopathies

Cilia are antenna-like membrane-associated structures playing essential roles during development, as well as during the normal function of many cells throughout the embryo and adult body. Although these highly conserved structures are found across a broad range of species, a nearly ubiquitous appearance is observed only in vertebrates. Cilia can be structurally divided into sub-compartments (Fig. 1): (i) a basal body, that consists of nine triplets of microtubules arranged in a ring from which extend three microtubules; (ii) a transition zone, region from which a nascent cilium grows; (iii) the middle zone, composed of nine doublets consisting of just A and B filaments, and finally (iv) the axoneme, that terminates with the distal zone, comprised primarily of microtubule singlets. Most cell types assemble only one cilium (a monocilium or primary cilium), whereas some cells build cilia bundles that consist of 200-300 individual organelles (multiple cilia) (Fliegauf *et al.*, 2007). The formation of cilia comprises targeting of specific proteins to the basal body area where pre-assembly of axonemal substructure (such as outer dynein arms) occurs. The transport of proteins and multiprotein precursors across the ciliary compartment border and along the length of the axonemes to their functional assembly site is dependent on intraflagellar transport (IFT). Protein are loaded onto the IFT particles at the ciliary base within the cytoplasm and transferred across the ciliary compartment border in a process known as compartmentalized ciliogenesis.

Cilia can either be motile or immotile. The 9+2 axonemes of most motile cilia are assembled by nine peripheral doublet microtubules surrounding two central microtubules (central pair complex); 9+2 axonemes contain associated structures including inner and outer dynein arms, radial spokes and nexin links. The 9+0 axonemes, which are found in most non-motile cilia, lack of the two central microtubules and are devoid of dynein arms. Mutations in genes encoding proteins that participate in IFT cause ciliogenesis defects of both motile and immotile cilia.

Although there are many different classes of cilia with a diversity of variation, all cilia types share the basic structural units composed of the outer microtubules doublets and the ciliary membrane. Even though the basic structure of the different types of cilia is obviously similar, they exert various tissue-specific functions during development, tissue morphogenesis and homeostasis (Fliegauf *et al.*, 2007).

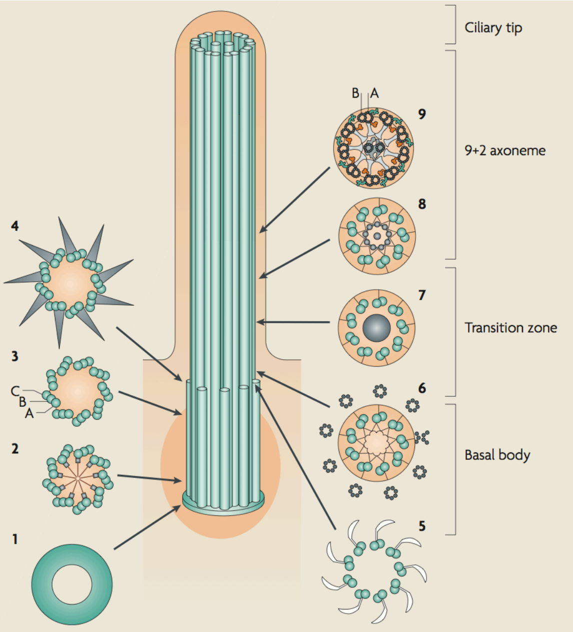

Figure 1. Ciliary sub-compartments (Modified from Fliegauf *et al.*, 2007).

Defective and dysfunctional functioning in motile and non-motile cilia affects multiple systems, causing blindness, deafness, chronic respiratory infections, kidney disease, heart disease, infertility, obesity and diabetes. These symptoms have significant impact on those affected; some are devastating, most are life-threatening. These so-called "ciliopathies" are usually genetically inherited, and at present there are few, if any cures.

Zebrafish models of ciliopathies

Zebrafish have emerged as useful organisms in which to explore the consequences of ciliary dysfunction and to model human ciliopathies. Zebrafish ciliary models with defects in various genes often display similar phenotypes of human ciliopathies.

Cilia dysfunction and defects during the embryonic establishment of left-right axis, for example, can lead to heterotaxy, the randomization of the left-right body asymmetry, possibly leading to malformation of the organs asymmetric along the left-right axis. Heterotaxy is tipically associated with heart malformations and anomalies of the visceral organs, as well as loss of normal organs asymmetry (Sutherland and Ware, 2009). It has been observed that half of individuals with primary ciliary dyskinesia (PCD) exhibit *situs inversus totalis* (also referred to as Kartagener's syndrome). A similar phenotype was observed in mice with recessive mutations in *Lrd*, the ortholog of *DNAH11*, a human axonemal dynein ß-chain gene. During early embryonic development (~7.5 days postcoitum), the rotational movement of nodal cilia at the ventral pole of the murine embryo creates a leftward fluid flow (nodal flow) that is thought to induce body symmetry breaking. Indeed, an artificially generated nodal flow independent from ciliary motility was found to be sufficient to determine laterality. Similar laterality breaking mechanisms, involving the Kupffer's vesicle (KV), have also been proposed for zebrafish (Fliegauf *et al.*, 2007).

In zebrafish, the KV is a transient spherical organ (Fig. 2) which originates from a group of approximately two-dozen cells, known as dorsal forerunner cells (DFCs); DFCs migrate at the leading edge of the embryonic shield (the zebrafish equivalent of the mouse node) during gastrulation. In contrast to other cells in this region, DFCs do not involute during gastrulation, but remain at the leading edge of epibolic movements. At the end of gastrulation, DFCs migrate deep into the embryo and organize to form KV. During subsequent somite stages, KV localizes ventrally to the forming notochord in the tailbud and adjacent to the yolk cell. It is now composed of two layers of cells having the cilia at both the dorsal roof and the ventral floor; all these cells possess monocilia (Essner *et al.*, 2005).

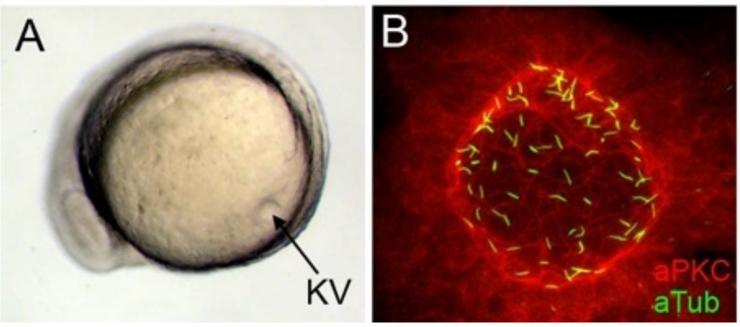

Fig. 2. Kupffer's vesicle is a ciliated organ in zebrafish. During somite stages of zebrafish development, Kupffer's vesicle (KV) forms in the tail region (A). Fluorescent immunostaining of KV cells (B) with atypical protein kinase C antibodies (red) to mark epithelial cells and acetylated tubulin antibodies (green) to label cilia. Each KV cell has a single cilium (www.amacklab.org).

A combination of laser ablations of DFCs which perturbs KV morphogenesis, embryological manipulations, analyses of mutants and antisense morpholinos against zebrafish *left-right dynein-related1* (*lrdr1*) injected either into all embryonic cells or specifically targeted to KV precursors, demonstrates that ciliated KV cells control LR development in different organs like, for instance, brain, heart, and gut (Essner *et al.*, 2005).

An example of human ciliopathies for which there is a zebrafish model is the Usher syndrome (USH). USH is the most frequent cause of deaf-blindness; it is a heterogeneous disease associated, in rare cases, with bronchiectasis, chronic sinusitis, and reduced nasal mucociliary clearance, indicative of ciliary dyskinesia. It is characterized by retinal degeneration, due to progressive loss of photoreceptors, and congenital deafness. The relevant USH proteins possibly function in sterocilia as well as in photoreceptor cilia (Fliegauf *et al.*, 2007). Although at least fourteen different chromosomal loci have been linked to USH, only eleven of the genes have been identified to date. Initially studies were concentrated on the Usher 1C gene (*USH1C*), which encodes a protein that has been proposed to function as a key scaffolding molecule to which most other Usher proteins can bind. Patients with mutations in *USH1C* exhibit a severe Usher pathology with profound congenital hearing impairment, vestibular dysfunction, and clinically appreciable retinal degeneration in childhood or early adolescence. Mouse models of USH1C, with mutations in the mouse *Ush1c* gene, exhibit profound deafness but fail to show notable retinal defects. Recent studies developed two zebrafish models for USH1C, both of which exhibit a strong deaf-blindness phenotype at early developmental stages. Young fish with depleted *ush1c* function have penetrant and specific visual defects as well as compromised hair cell development resulting in hearing and balance impairment (Phillips *et al.*, 2011).

Non-Syndromic Hearing Loss (NSHL)

As the most common sensory disorder in humans, hearing loss affects about 1 in 1000 newborns. It is assumed that at least half of the cases have a genetic basis, and more than two-thirds of this subset is classified as non-syndromic hearing loss (NSHL) because of the absence of additional symptoms. The vast majority of NSHL is caused by mutations in autosomal genes, while X-chromosomal inheritance accounts for only 1–5% of the cases (Huebner *et al.*, 2011). In this latter case, females often show later onset and less severe presentation than males thanks to random X-inactivation. Currently, there are five known chromosomal NSHL loci for X-linked deafness: *DFNX1* MIM# 304500, *DFNX2* MIM# 304400, *DFNX3* MIM# 300030, *DFNX4* MIM# 300066, and *DFNX5* MIM# 300614 (Abdelfatah *et al.*, 2013). DFNX can be either pre- or post-lingual, with an age of onset varying from congenital (DFNX1, DFNX2, and DFNX3), to childhood (DFNX4), or adolescence (DFNX5). The type of hearing impairment is sensorineural, except for DFNX2, that shows mixed hearing impairment, and DFNX5, which is accompanied by poor speech discrimination scores and poor understanding. In most patients hearing impairment is progressive and severely affecting all frequencies (Schraders *et al.*, 2011). Three papers were recently published which identified *SMPX (Small Muscle Protein X-*

linked) as the deafness-causative gene at the *DFNX4* locus in two Dutch families (Schraders *et al.*, 2011), one German family, one Spanish family (Huebner *et al.*, 2011), and two families of the Newfoundland island (Abdelfatah *et al.*, 2013).

Human and mouse *Smpx* Gene

The human *SMPX* gene, originally cloned from skeletal muscle, encodes an 88-amino acid protein with no known functional domains (Patzak *et al.*, 1999). *SMPX* was also identified in a screening for stretch-responsive skeletal muscle genes and shown to be highly upregulated in response to passive stretch *in vivo* (Kemp *et al.*, 2001). The gene consists of five exons (≥172, 57, 84, 148, ≥422 bp) and four introns (3639, 10410, 6052, 31134 bp), comprising together a 52.1 kb genomic region (Patzak *et al.*, 1999). SMPX is proline-rich and contain a potential nuclear localization signal, two casein kinase II phosphorylation sites (CKII), and a destabilizing sequence proline-, glutamic acid-, serine-, threonine-rich (PEST), that suggests SMPX undergoes rapid degradation (Schraders *et al.*, 2011).

As mentioned above, in four different family four nonsense mutations have been identified. A first paper showed like in a German family, sequence analysis revealed a p.Glu37X mutation (c.109G>T), while sequencing of the *SMPX* gene in a Spanish family disclosed a p.Gly59X mutation (c.175G>T) (Huebner *et al.*, 2011). Concurrently, a study of two additional families identified a large Dutch family with a p.Glu72X (c.214G>T) and a second one which had a single base pair deletion (c.130delG, Schraders *et al.*, 2011). At last, in two family of Newfoundland island, a novel same point deletion (c.99delC) has been found (Abdelfatah *et al.*, 2013) (Fig. 3).

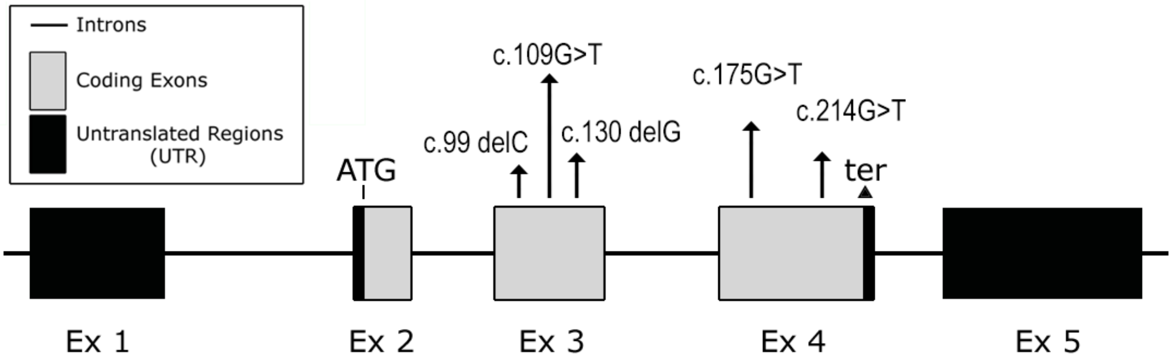

Figure 3. *SMPX* gene structure and identified NSHL-linked mutations (Modified from Abdelfatah *et al.* 2013).

The phenotype of all the *SMPX* mutations carriers is similar; it is also interesting to note that all the mutations associated with *SMPX* and related to hearing loss are null mutations resulting in a premature stop codon. This molecular feature suggests that the mutant transcripts may undergo nonsense-mediated mRNA decay (NMD), suggesting loss-of-function as the underlying mechanism of the hearing impairment, although further studies are needed to confirm it. Nonetheless, all these data support the association of *SMPX* to the DFNX4 locus (Abdelfatah *et al.*, 2013).

The first study of the expression pattern of *SMPX* was performed with human multiple tissue RNA blot and showed that *SMPX* was abundantly and specifically expressed in skeletal and heart muscle (Patzak *et al.*, 1999). Subsequently, since the identification of mutations in *SMPX* as a possible cause of non-syndromic hearing impairment, additional RT-PCR assays were performed. Results, in agreement with previous studies, confirmed the presence of abundant *SMPX* transcription in both fetal and adult skeletal muscle and heart and, in addition, showed relatively high *SMPX* transcripts levels in fetal inner ears (Fig. 4), supporting the involvement of *SMPX* in X-linked NSHL (Schraders *et al.*, 2011).

As a first step to identify a function of this gene, additional studies have been performed using murine models.

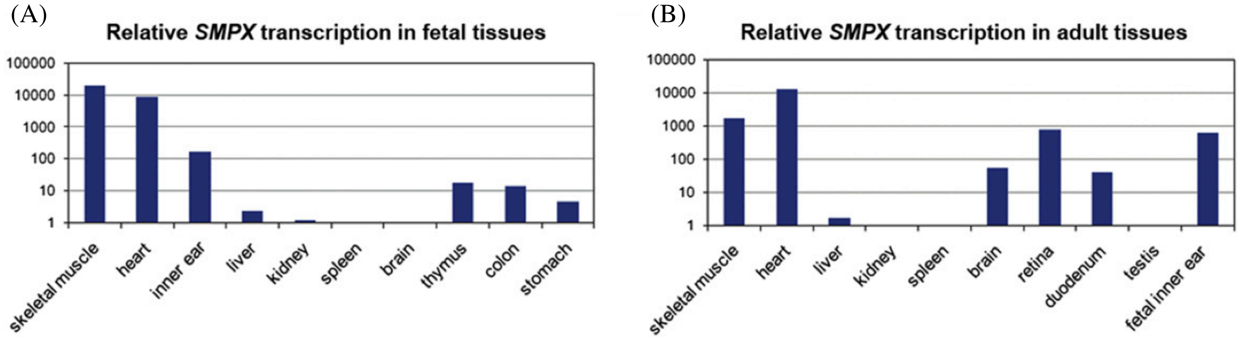

Figure 4. Relative *SMPX* mRNA expression as determined by quantitative PCR in fetal (A) and adult (B) human tissues (Modified from Schraders *et al.*, 2011).

The murine *Smpx* gene encodes an 85-amino acid protein, which is associated with actin and focal adhesion complexes and functions as a regulator of cytoskeletal dynamics (Kemp *et al.*, 2001; Schindeler *et al.*, 2005). Smpx displays 85% of identity with the human protein and, unlike *SMPX*, the gene consists of six exons and five introns comprising together 53,62 kb. Despite two amino acids that differ between the murine and the human proteins, the CKII consensus sequence is still maintained, supporting its candidature as a genuine site for phosphorylation. Indeed, it has been hypothesized that phosphorylation of Smpx may regulate its function and subcellular localization (Kemp *et al.*, 2001).

At first, RNase protection analysis of mRNA samples extracted from a variety of adult mouse tissues showed a strong signal of *Smpx* (also called *Chisel, Csl*) in heart, skeletal muscle, and tongue (Fig. 5A), with a weaker signal in lung, testes, and large intestine (Palmer *et al.*, 2001). Also interestingly, the presence of *Smpx* expression was detected in various developing organs at different embryonic stages.

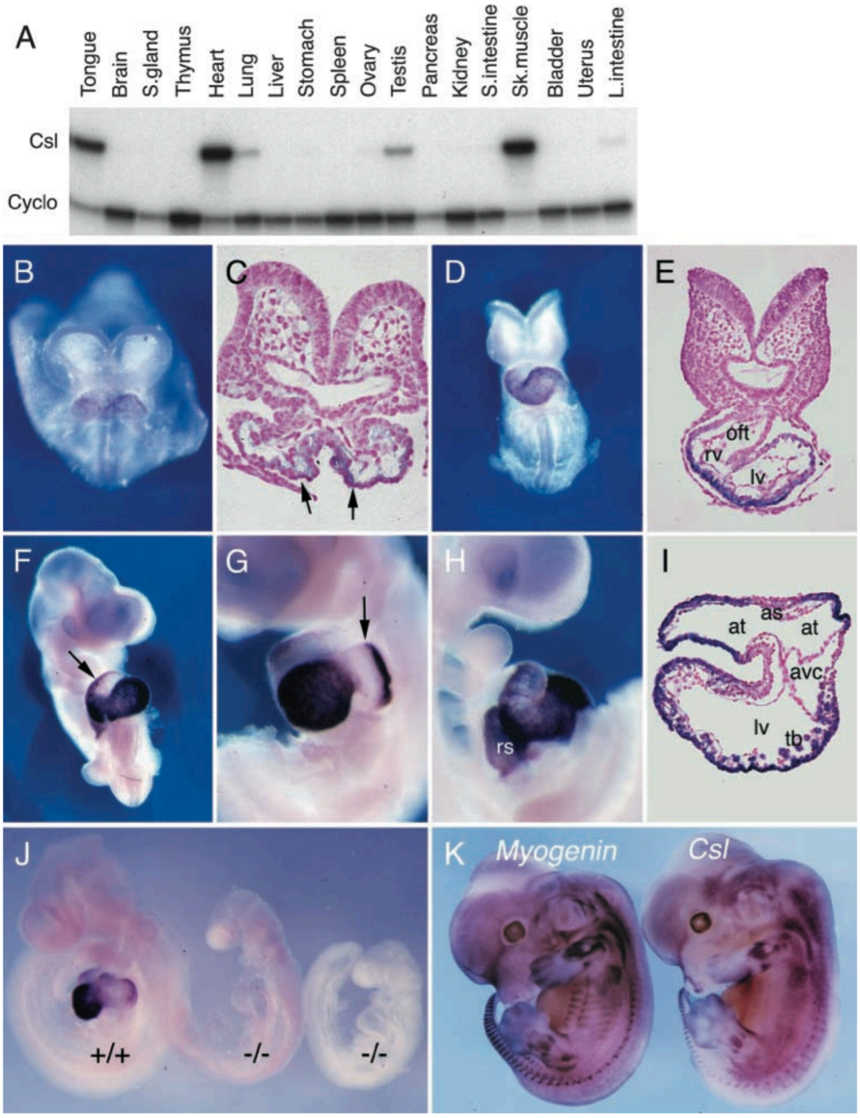

Figure 5. *Smpx (Chisel Csl)* mRNA expression. (A) RNase protection analysis of *Smpx* and control *cyclophilin* (Cyclo) mRNAs in adult mouse tissues. (B–K) Whole-mount in situ hybridization using *Smpx* probe on mouse embryos. (B) Ventral view of E8.25 embryo. (C) Section of the embryo shown in B. Arrows indicate expression on the ventral surface of the fusing heart tube. (D) Ventral view of E8.5 em- bryo. (E) Section of embryo depicted in D showing *Smpx* expression at the outer curvature of the ventricles. (F–H) E10.5 embryo viewed from the ventral and left and right sides, respectively. Arrow in F indicates rib of expression in outflow tract. Arrow in G indicates expression in presumptive left atrial appendage. (I) Section of E10.5 heart. (J) E9.5 *Nkx2-5*-/- embryos (-/-) compared with wild-type sibling (+/+). (K) E13.5 embryos comparing expression of *Smpx* and *myogenin*. as, atrial septum; at, atrium; avc, atrioventricular canal; lv, left ventricle; oft, outflow tract; rs, right sinus horn; rv, right ventricle; tb, trabeculae (Yoon *et al.*, 2011).

In-situ hybridization assays, performed on mouse embryos, showed that *Smpx* starts to be expressed from E8.25 in those myocytes, located at the ventral surface of the heart progenitor region, undergoing active fusion (Fig. 5B,C). The transcript was present during the early stages of heart looping (E8-E8.5), restricted to the myocardial layer at the outer curvature of the presumptive left and right ventricles (Fig. 5D,E). By E9.5–10.5, the expression was also evident in the developing sinoatrial region in a left-right asymmetric pattern. On the right side, the developing right atrium and right horn of the sinus venosus were strongly positive, whereas on the left a disc-shaped pattern was evident in the dorsolateral region of the common atrium, suggestive of the future position of the left atrial appendage. However, the left sinus horn was negative for *Smpx* expression. Transcripts were undetectable in most of the atrioventricular canal, the inner curvature, and in myocardium associated with the forming atrial septum (Fig. 5,G,I). The outflow tract was also negative, except for a unique rib of expression along its outer curvature (Fig. 5F). During fetal development, *Smpx* expression continued in the outer curvature of the ventricles and in the atrial appendages (Palmer *et al.*, 2001). Moreover, also in developing skeletal muscles starting from E11.5 (specifically at E13.5), it is evident the expression of *Smpx* in the myotomal compartment of somites and in developing limb, head, and neck muscles in a pattern resembling that of the myogenic regulatory factor gene *myogenin* (Fig. 5K) (Palmer *et al.*, 2001).

An interesting study identified *Smpx* between novel genes associated with hair cell differentiation or hearing loss during the inner ear development (Fig. 6); an archived gene expression dataset generated using mouse inner ear tissues at several embryonic stages has been analyzed (Yoon *et al.*, 2011). By hybridization assays, *Smpx* activity was compared with the cochlear expression patterns of *Atho1* (*Atonal* homolog, also known as *Math1*) and *Myo15 (myosin15)*, two well known markers for hair cells, both of which are essential for their differentiation and maturation. Data showed that *Smpx* is expressed in the hair cells of the vestibular organs including utricule, saccule and all the *cristae* at E15.5, at least up to postnatal stages P5 (Yoon *et al.*, 2011). In detail, *Smpx* expression was initially barely detectable at the cochlea level, probably because differentiation of the cochlear hair cells occurs later than the vestibular hair cells. At P1 stage, *Smpx* transcript was clearly visible in the base and mid-base of the cochlear duct and faintly in the mid apex. By P5 *Smpx* was strongly expressed in the hair cells of all cochlear turns region (Yoon *et al.*, 2011). So, since the onset of *Smpx* expression in the developing hair cells appeared to be slightly delayed in comparison to *Myo15*, the authors suggested a possible role of *Smpx* in maturation or maintenance, rather than early specification of hair cells.

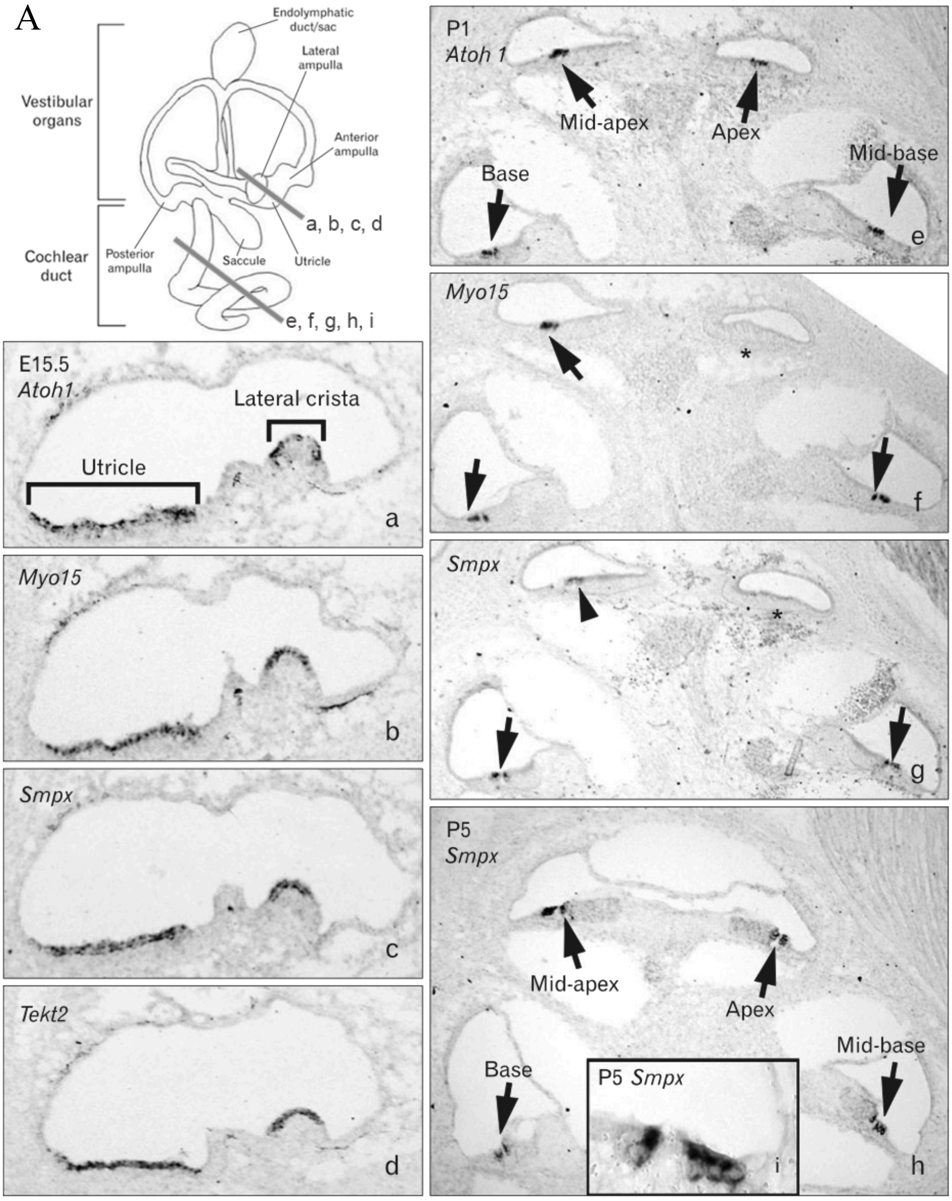

Figure 6. Diagrammatic representation of the substructures of the mouse inner ear and expression patterns of *Smpx* in the developing inner ear. (A) mouse inner ear schematic representation. (a-h) Expression patterns of *Smpx* in the developing inner ear analyzed with *in situ* hybridization at E15.5 (a- d), P1 (e-g), and P5 (h, i). Lines in the inner ear diagram show the levels of sections. *Atoh1* (a, e) and *Myo15* (b, f), well known markers for hair cells, were used to locate the hair cells in the inner ear tissues. At E15.5, expression of *Smpx* was found in the developing hair cells of the vestibular organs (c). At P1, *Atoh1* expression was found in the hair cells of all cochlear turns (e, arrows) and *Myo15* expression was found in the base, mid-base, and mid-apex of the cochlea (f, arrows), but not yet in the apex (f, asterisk). *Smpx* expression was found in hair cells of basal and mid-basal turns (g, arrows) and weakly in the mid-apical turn (g, arrowhead). At P5, *Smpx* expression was detected in hair cells of all cochlear turns (h, i, arrows) (Modified from Yoon *et al.*, 2011).

Immunolocalization studies conducted on the adult mouse cochlea revealed the presence of the protein in different cell types, both in the sensory epithelium (inner and outer hair cells) and non-sensory supporting cells (Deiter cells, Bötcher cell, and inner and outer pillar cells), as well as in Root cells, involved in building up a cellular network in the lateral wall of the cochlea (Huebner *et al.*, 2011). Given the association of SMPX with the cytoskeleton, its responsiveness to mechanical force, and the detection of Smpx in hair cells in the mouse, Huebner and colleagues speculated that SMPX might play a role in the maintenance of stereocilia, which are permanently exposed to physical stress (Huebner *et al.*, 2011).

A second link between Smpx and cochlea development and function is provided by IGF-1 (insulin-like growth factor 1). When Smpx is *in-vitro* stimulated by IGF-1, it modifies cell shape and promotes myocyte fusion in C2C12 mouse myogenic cells. IGF-1 mutations in humans are associated with syndromic sensorineural deafness and Igf-1-deficient mice have multiple cochlear abnormalities, including anomalous differentiation, reduced survival of spiral ganglia neurons, and abnormal tectorial membrane. Moreover, MEF2 (myocyte enhancer binding factor 2) has been indicated to be a target gene of IGF-1 in the mouse cochlea in both the sensory cells and the spiral ganglia neurons. Interestingly, the IGF-1-mediated increase of MEF2 activity in myoblasts is augmented by Smpx; additionally, a consensus sequence for MEF2 binding is present twice in the highly evolutionarily conserved 5’ upstream region of SMPX, suggestive of a more complex network involving these three players.

Another remarkable *in-vitro* data associated with inner ear dysfunction are defects in the Rac1/p38 pathway, which is a target of Smpx (Schindeler *et al.*, 2005). The small GTPase Rac1 is activated by biomechanical stress, upon which it is recruited to sites of actin reorganization and integrin-mediated cell adhesion. Intriguingly, conditional ablation of Rac1 in the otic epithelium of mice resulted in defective morphogenesis of the auditory sensory epithelium and stereociliary bundle (Wei *et al.*, 2005). p38 kinase has also been shown to be of relevance for inner ear function, acting downstream of Smpx and Rac1 in regulating actin dynamics; interestingly, inhibition of p38 MAP kinase phosphorylation suspended gentamicin-induced ototoxicity, a side effect of aminoglycoside therapy leading to permanent hair cell loss and hearing impairment (Schindeler *et al.*, 2005).

Zebrafish as a model for inner ear development, function, and deafness

Firmly established as a model organism for embryonic developmental studies, zebrafish is now emerging as an effective system to elucidate the fundamental aspects of several human diseases (Graham and Currie, 2007). Despite the significant evolutionary distance, gene functions and pathways are often highly conserved between zebrafish and humans. Specifically, zebrafish represent an excellent model for studying inner ear development and function. Indeed, zebrafish ear development is quite similar to what observed in other vertebrates (Whitfield *et al.*, 1996), and the signaling pathways required for its development and functions are strikingly conserved (Whitfield, 2002).

The development of the ear proceeds quite rapidly in zebrafish. Within 16 hours post fertilization (hpf), a thickening of the ectoderm, the otic placode, becomes visible. Soon after cavitation (18 hpf), the first hair cells appear at the opposite poles of the ventral portion of the lumen. These two sensory patches will give rise to the anterior and posterior maculae, respectively. Around 20 hpf, when the first hair cells appear, otoliths (calcium carbonate stone situated above the macula) attach to the kinocilia. During this period neuroblasts delaminate from the otic vesicle to form the first-order neurons of the auditory/vestibular (VIIIth) nerve. Forces impinging upon the otoliths cause them to move, which in turn deflect the underlying hair bundles. Macular organs in zebrafish are important for both hearing and for sensing linear acceleration and gravity. At approximately 45 hpf, epithelial columns sprout from the otocyst wall and grow into the lumen, where they meet and fuse in the following 10-hour stretch. Eventually, they will form the central hubs around which the semicircular canals develop. The sensory patches, or cristae (sensory epithelium of hair cells and supporting cells inside the semicircular canals) will form about a day later than the anterior and posterior maculae. By 96 hpf, the larvae are free swimming and have fully functional ears (Fig. 7A).

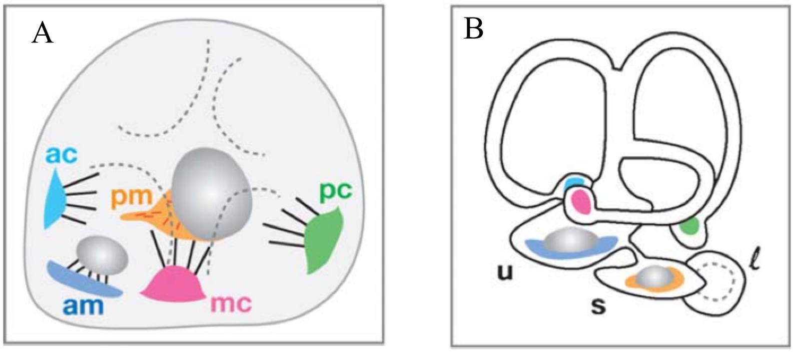

Fig. 7. Zebrafish larval and adult ear. (A) Diagrammatic representation of the zebrafish larval ear. All five sensory patches are indicated in color. Dotted lines indicate the epithelial structures around which the semicircular canals form. (B) Diagram of the adult zebrafish ear. A third macular organ, the lagena (dotted area), forms later during the juvenile stage. Colors correspond to those in panel A.

Abbreviations: ac, anterior crista; am, anterior macula; l, lagena; mc, medial crista; o, otolith; pc, posterior crista; pm, posterior macula; s, saccule; u, utricle. (Modified from Nicolson 2005).

Although the zebrafish ear does not contain a specialized hearing organ - there is no equivalent of the mammalian cochlea - zebrafish are classified as 'hearing specialists', being characterized by morphological adaptations (Weberian ossicles, see below in this text) that aid in the detection of sound pressure (Nicolson, 2005). After the larval stage (30 days post fertilization, dpf), zebrafish develop additional organs including the macular organ called lagena, and the macula neglecta, with auditory function (Fig. 7B). As mentioned above, zebrafish develop a series of bones known as Weberian ossicles, connecting the swim bladder to the saccule. Sound can set the air-filled swim-bladder into motion, and such motion is transmitted to the sensory epithelium via the ossicles, thus amplifying the sound (Nicolson, 2005).

As in other vertebrates, the inner ear is also used to maintain balance (Whitfield, 2002). In addition, fish like frogs possess another organ that employs sensory hair cells, the lateral line organ, taking its name from the clusters of hair cells, known as neuromasts, located in a series extending along the trunk. The lateral line organ allows the detection of low-frequency stimuli, such as water movements, and it is important in schooling, prey detection, and other behaviors (Nicolson, 2005).The anatomy of the zebrafish ear differs significantly from that of the human inner ear, and thus the zebrafish model cannot hope to recapitulate all aspects of human hearing loss (Whitfield, 2002). Nevertheless, as previously mentioned, it is clear that many of the same genetic pathways are utilized for the development and function of the inner ear in all vertebrate groups. Hair cells, for example, require MyosinVIIa to function correctly, whether in a human cochlea or a zebrafish neuromast. Likewise, FGF signaling appears to play an important role in otic induction in chick, mouse, and zebrafish, although different FGFs may be utilized for the same process in different species. As yet, there are zebrafish models of many human deafness syndromes including, for example, Usher syndrome, an autosomal recessive disorder characterized both by deafness and blindness, Waardenburg-Shah syndrome, a rare genetic disorder characterized by auditory-pigmentary abnormalities, and Hirschsprung disease (Whitfield, 2002). Furthermore, zebrafish is amenable to genetic and molecular manipulations that are infeasible in any other vertebrate model, and will therefore be of importance in increasing our understanding of both the biology of inner ear development and, possibly, the etiology of human hearing loss.

Zebrafish *smpx*

Zebrafish *smpx* is located on chromosome 24 and consists of five exons and four introns spanning together about 27 kb. The gene encodes an 83-amino acid protein sharing 85%

of identity with the human protein.

Main results

<u>*smpx* expression analysis</u>

The spatial and temporal *smpx* expression patterns during the early stages of zebrafish development have been analyzed by means of RT-PCR and whole mount *in-situ* hybridization (WISH) assays. RT-PCR has been performed on developmental stages from 1-cell stage to 72 hpf (hours post fertilization) (Fig. 8). *smpx* starts to be expressed from the 4-somite stage, with the smpx-specific primers detecting two amplicons of 188 and 275 bp, respectively, corresponding to alternative splicing isoforms (Fig. 8B,C), as confirmed by DNA sequencing. The two mRNAs encode a short (54 amino acid residues) and a long (83 amino acid residues) form of protein (Fig. 8C). Interestingly, even though no Smpx short form is reported in any protein database, a more in depth bioinformatic inquiry revealed that such splicing event does occur also in higher vertebrates; indeed, the BLAST/tblastn analysis of the ncbi Expressed Sequence Tags (ESTs) database returned - besides some positive hits concerning Smpx short form in other fish species (i.*e*. *Oncorhynchus mykiss* and *Salmo salar*) - also positive hits regarding the presence of the mRNA encoding such form of the protein in the two mammals *Heterocephalus glaber* and *Sus scrofa* (data not shown). Later on during zebrafish development, only the 275 bp *smpx* amplicon is detectable in the stages analyzed (24 – 72 hpf).

smpx expression at 4-somite stage has been also revealed by WISH; at this stage, smpx mRNA marks specifically the Kupffer's vesicle (KV) (Fig. 9A,B). From 10 somites to 24 hpf, *smpx* is expressed at the level of the somites (Fig. 9C,10). At 24 hpf the signal is still present in the somites and starts to be visible in the heart (Fig. 10A). By 36 hpf, *smpx* is also detectable at the ear level (Fig. 10B,C). The images at 48 hpf show *smpx* persistent expression in the heart (Fig. 10D,E) and display the specific signal in the ear, precisely in the hair cells of the anterior (Fig. 10F) and the posterior macula (Fig. 10G). At 72 hpf, *smpx* transcripts are visible in the heart (Fig. 10H), in the ear (Fig. 10J,K) and in the branchial arches (Fig. 10H). Additionally, *smpx* expression is now detectable in the developing eye muscles and in the developing pectoral fins (Fig. 10I).

<u>*smpx* functional analysis</u>

smpx functional analysis in zebrafish embryos has been performed by means of gain- and loss-of-function assays, microinjecting *smpx* synthetic mRNA and smpx-specific Morpholino (MO) antisense oligonucleotide, respectively. GFP *in-vitro* synthesized mRNA has been used as control for the gain-of-function assay, while a standard control MO (SC-

MO) injection has been employed to monitor the loss-of-function analysis (from now on all the MO-injected embryos will be defined as *morphants*).

While the gain-of-function assay did not determine any phenotypic alteration in the embryos at all the tested stages (data not shown), *smpx* functional ablation produces obvious embryonic defects, including abnormal body curvature, randomized heart looping, cardiac edema, and cysts formation (Fig. 11). Zebrafish body curvature alterations, as well as pronephric cysts formation and altered left-right patterning, are linked to defects in genes important for cilia development (Serluca *et al.*, 2009). As mentioned above, the earliest visible sign of embryonic *smpx* expression occurs in the KV, where ciliated cells produce a directional flow required for the establishment of the left-right asymmetry in the placement of the internal organs. Therefore, in order to determine whether the loss of function of *smpx* produced any effects on KV cells, 10-somite morphant embryos were stained with acetylated tubulin antibody for cilia labelling and analyzed under a confocal microscope (Fig. 12). *smpx* morphants displayed a fully formed KV, although they showed a lower number of cilia (less of 50%; n morphants = 8, n controls = 9) when compared to control embryos (Fig. 12A,B). These findings lead us to evaluate, like consequence of deficiencies in the KV, a possible loss of the left-right organ asymmetry. Consequently, to assess organ laterality in *smpx* morphants, we analyzed the position of the heart, liver, pancreas, and medial habenular subnuclei by means of WISH, employing specific markers for these organs (Fig. 13). In a wild-type zebrafish embryo, the ventricle of the heart loops toward the right and the atrium loops towards the left, the liver is positioned to the left of the midline, the pancreas lies to the right of the midline and the number of medial habenular subnuclei is greater in the right side of the dienchephalon (Fig. 13). WISH using *prox1* probe (Pistocchi *et al.*, 2008), labeling liver, pancreas, and medial habenular subnuclei, showed the wild-type pattern (see SC-MO embryos in Fig. 13E,H) in 30% of *smpx* morphants, while an undefined asymmetry (Fig. 13G) or a complete reversal in the placement of the organs is present in the remaining 70% of the embryos (Fig. 13F,I; n morphants and n controls = 100). The same results were obtained using the cardiac-specific *cmlc2* probe (Yelon et al., 1999): 37% of *smpx*-morphants evidenced the correct orientation (see SC-MO embryos in Fig. 13A), while in the remaining 63% a non-looped (Fig. 13C,D) or an inverted heart (Fig. 13B) was visible (n morphants = 120, n controls = 85). Taken together, this wealth of data strongly suggests that such anomalies in the left-right asymmetry may represent a direct consequence of the abnormal number of cilia in the KV determined by *smpx* down-regulation.

In order to investigate ear development in *smpx* deficient embryos, the expression pattern of two different ear markers at two different stages of development has been analyzed by WISH (Fig. 14A-D), together with FITC-phalloidin staining to highlight the cells cytoskeleton (Fig. 14E,F). Specifically, the macular markers *fgf8* (Reifers *et al.*, 1998) and *pax5* (Kwak *et al.*, 2006) has been employed to paint the ear of 30 and 48 hpf morphants, respectively (n morphants = 64 + 71, n controls = 51 + 60). The assay demonstrated that *smpx* knock-down did not exert any effects on the formation of the gross ear structures in all analyzed stages (Fig. 14). Indeed, the anterior macula is correctly formed also in *smpx* morphants (Fig. 14A-D), and the whole ear structure is indistinguishable between *smpx* and standard control embryos, as proved by the FITC-phalloidin staining (Fig.14E,F). Finally, in order to assess potential effects of *smpx* down-regulation on ear cilia structure, immunohistochemistry assays using anti-acetylated tubulin antibody have been performed. The fluorescence confocal microscope observation of the morphant ear revealed the noteworthy 40% reduction of the number of cilia in the macular regions (Fig. 15B; n morphants = 10, n controls = 11). Therefore, it is conceivable to presume a crucial role of *smpx* in the proper differentiation and/or maintenance of the cilia structure also in the ear, providing a possible explanation to the documented cases of *SMPX*-linked human deafness (Huebner *et al.*, 2011; Schraders *et al.*, 2011; Abdelfatah *et al.*, 2013).

A

NCBI Ref. Seq.	Primers
NM_001002185.1	*smpx*_F0: 5’ TTGACATTTGTGTCTGACACCA *smpx*_F1: 5’ ACTGCACACAATGTCAAAACA *smpx*_R1: 5’ CACCTGAGCCAATTTAGTCTT

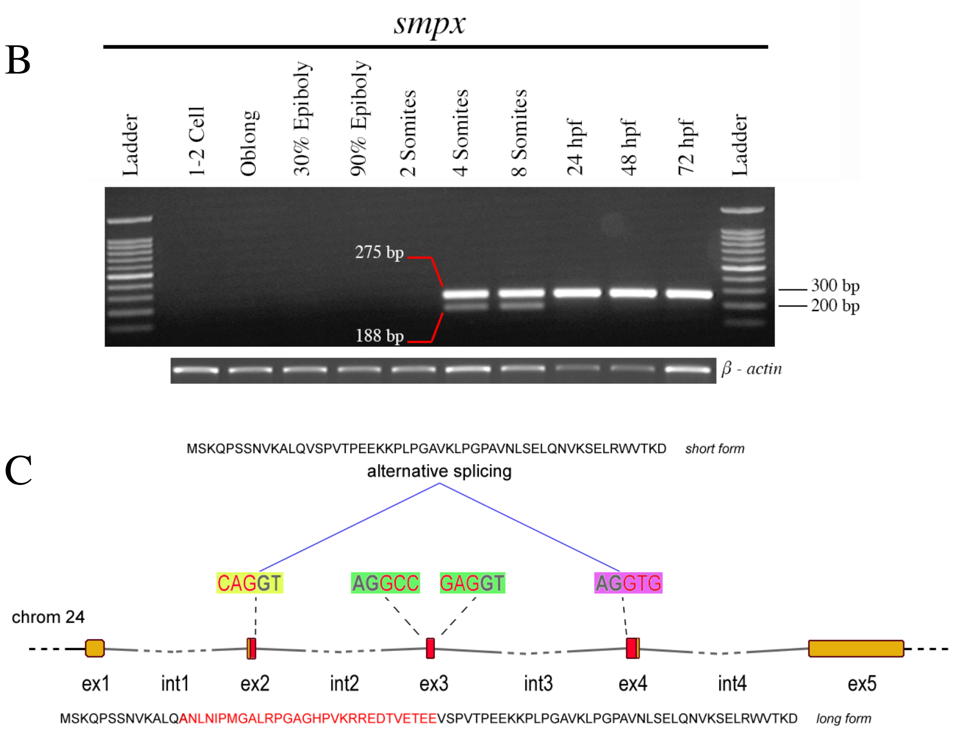

MSKQPSSNVKALQVSPVTPEEKKPLPGAVKLPGPAVNLSELQNVKSELRWVTKD *short form*

MSKQPSSNVKALQANLNIPMGALRPGAGHPVKRREDTVETEEVSPVTPEEKKPLPGAVKLPGPAVNLSELQNVKSELRWVTKD *long form*

Fig. 8. *smpx* expression profile during zebrafish development.

(A) Zebrafish *smpx* accession number and sequences of the primers designed to conduct the expression analysis.

(B) Ethidium bromide-stained gel of the semi-nested RT-PCR performed with the *smpx*_F1 and *smpx*_R1 primers using the *smpx*_F0/*smpx*_R1 reaction as template. 188 and 275 bp bands represent the two products of alternative splicing of the *smpx* RNA (see below for details). The gene is expressed starting from the 4-somite stage up to 72 hpf (upper panel). RT-PCR employing β-actin specific primers has been performed as control for RNA integrity.

(C) *smpx* genomic organization and alternative splicing forms of the mRNA. Zebrafish *smpx*, as well as the human *SMPX*, spans five exons (ex1 - ex5) on chromosome 24, three of which (red boxes) encoding a polypeptide of 83 amino acid residues (long form). When intron 2 donor site (GT, boxed in yellow) and intron 3 acceptor site (AG, boxed in purple) interact, exon 3 is spliced out, resulting in a smaller transcript encoding a 54 amino acid residues protein (short form); in red the portion of the long form encoded by exon 3. The intron 2/exon 3 and exon 3/intron 3 splice junctions are boxed in green.

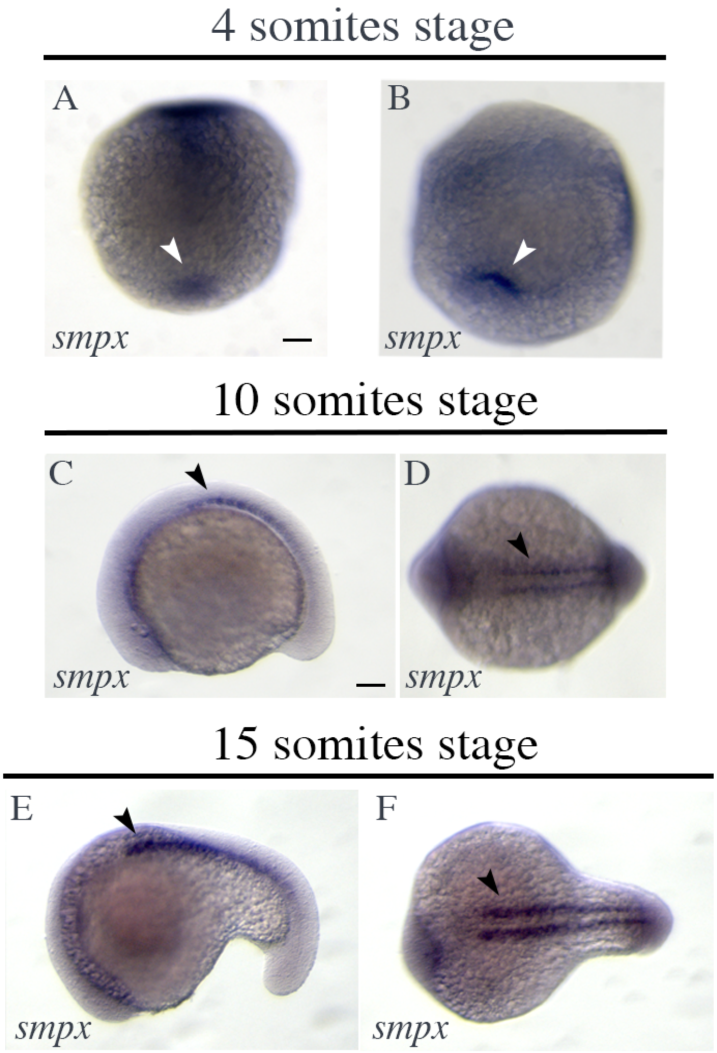

Fig. 9. Developmental expression of *smpx* in zebrafish.
(A, B) *smpx* WISH at 4-somite stage: the transcripts are detected in the KV (white arrowheads).
(C - F) *smpx* WISH at 10- and 15-somite stage: the transcripts are detected in the somites (black arrowheads).
(A, D, F) dorsal view. (B, C, E) lateral view. (B - F) anterior to the left.
Scale bars indicate 150 μm.

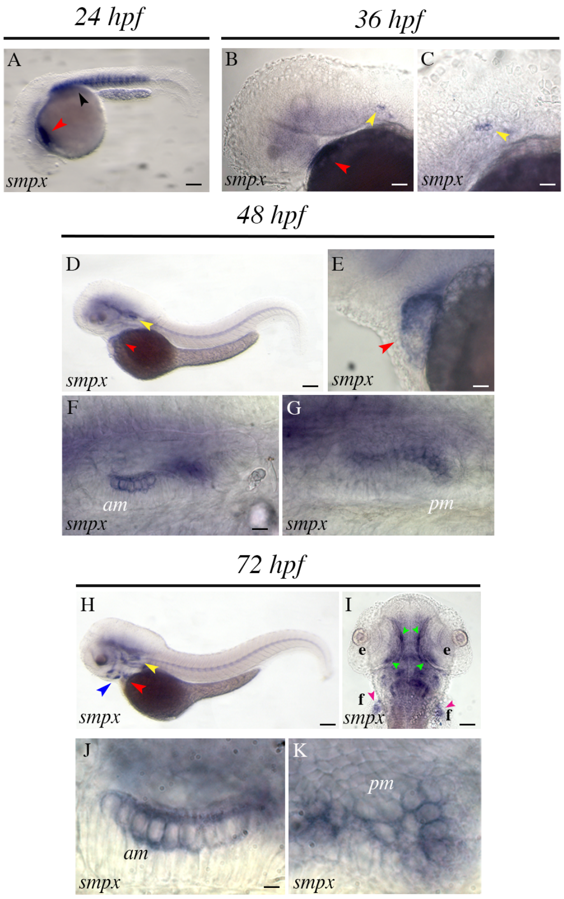

Fig. 10. Developmental expression of *smpx* in zebrafish.
(A) *smpx* WISH at 24 hpf: the transcripts are detected in the somites (black arrowhead) and are now also visible in the heart (red arrowhead).
(B, C) *smpx* WISH at 36 hpf: the transcripts are still present in the heart (red arrowhead) and now label the ear (yellow arrowhead).
(D-G) *smpx* WISH at 48 hpf: (D) the transcripts are present in the heart (red arrowhead) and (D, E) in the ear (yellow arrowhead). (E) Magnification of the heart at 48 hpf. (F, G) Magnification of the ear: (F) anterior macula, (G) posterior macula *(pm)*.
(H-K) *smpx* WISH at 72 hpf: (H, I) *smpx* transcripts are visible in the heart (red arrowhead), the ear (yellow arrowhead), the branchial arches (blue arrowhead), the developing eye muscles (green arrowheads), and the pectoral fins (pink arrowheads). (J, K) Magnification of the ear: (J) anterior macula, (K) posterior macula.
(I) shows dorsal view; all the other panels show lateral views. In all panels anterior is to the left, dorsal to the top.
Abbreviations: *am*, anterior macula; *pm*, posterior macula.
Scale bars indicate 200 μm (A, D, H), 100 μm (B), 60 μm (C, E), 30 μm (F, G), 20 μm (J, K).

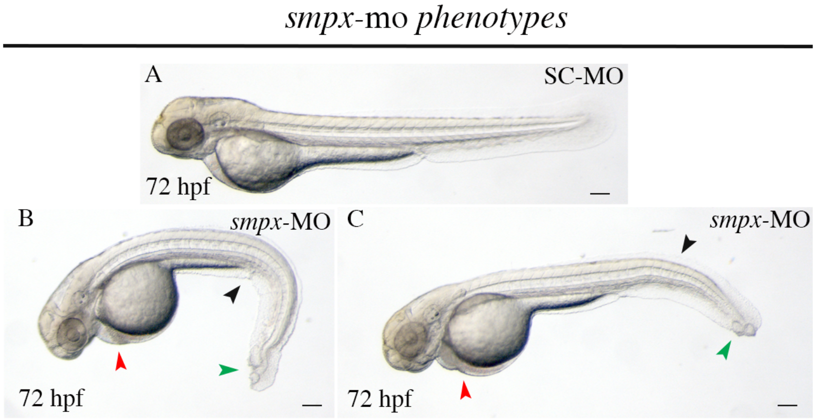

Fig. 11. *smpx* morphants phenotype. (A) Standard-ctrl morpholino (SC-MO) embryo at 72 hpf. (B, C) *smpx* morphant embryo exhibiting ventral axis curvature (black arrowheads), cardiac edema (red arrowheads), and cysts (green arrowheads).
All panels show lateral views, anterior to the left, dorsal to the top.
Scale bars indicate 200 µm.

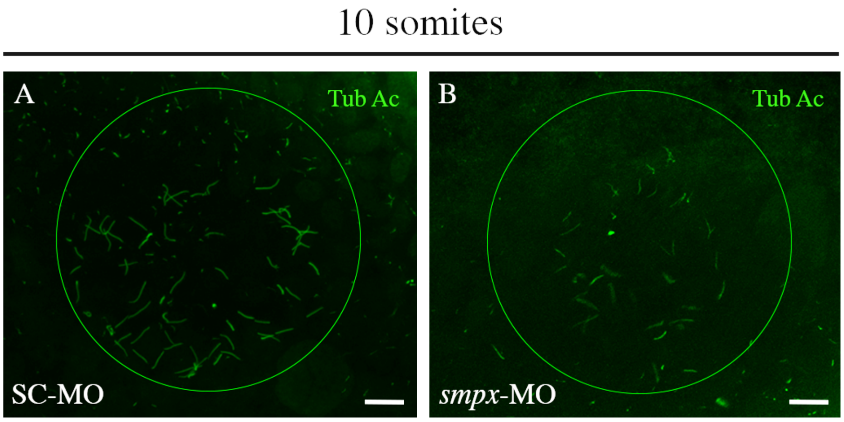

Fig. 12. Defective number of cilia in the Kupffer's vesicle (KV) following *smpx* down-regulation. Immunofluorescence performed with antibody against acetylated tubulin in 10-somite stage embryos KV (green circles): (A) normal control embryos (SC-MO) display a higher number of KV cilia in comparison to (B) *smpx* morphants.
Scale bars indicate 10 µm.

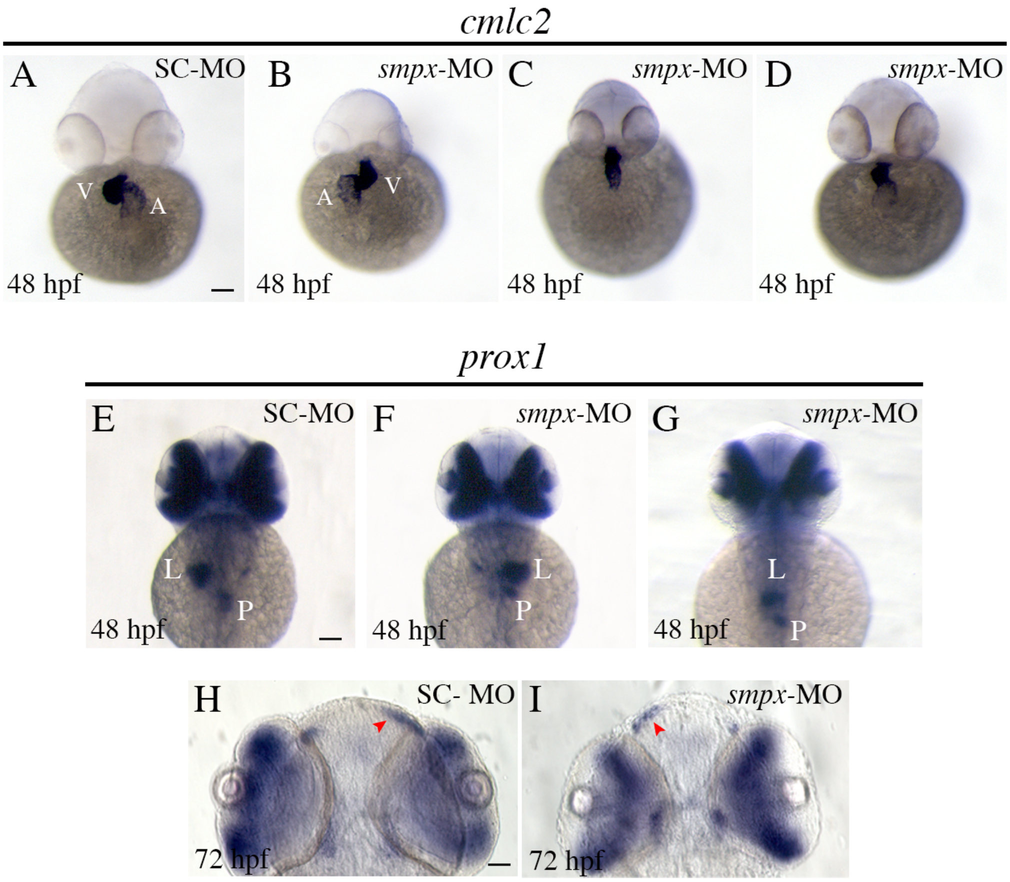

Fig. 13. Organ laterality in *smpx* morphants.

(A-D) Alteration of the wild-type expression pattern of the cardiac-specific marker *cmlc2* following *smpx* down-regulation. In comparison to the (A) standard control morphants (SC-MO), *smpx*-morphants (*smpx*-MO) evidence (B) a full cardiac inversion or (C, D) a non-looped heart.

(E, H) Loss of left-right organ asymmetry documented using a *prox1*-specific probe. (E) In comparison to the standard control embryos (SC-MO), *smpx* morphants show (F) a complete reversal or (G) an undefined asymmetry in the placement of liver and pancreas. (H, I) The asymmetric distribution of the medial habenular subnuclei in the diencephalon (red arrowhead) is perturbed following *smpx* knock-down, as clear comparing (H) control embryos (SC-MO) with (I) *smpx* morphants (smpx-MO).

Abbreviations: V, ventricle; A, atrium; L, liver; P, pancreas.

Panels (A-D) show frontal views; all the other panels (E-I) show dorsal views.

Scale bars indicate 200 µm (A-G), 60 µm (H, I).

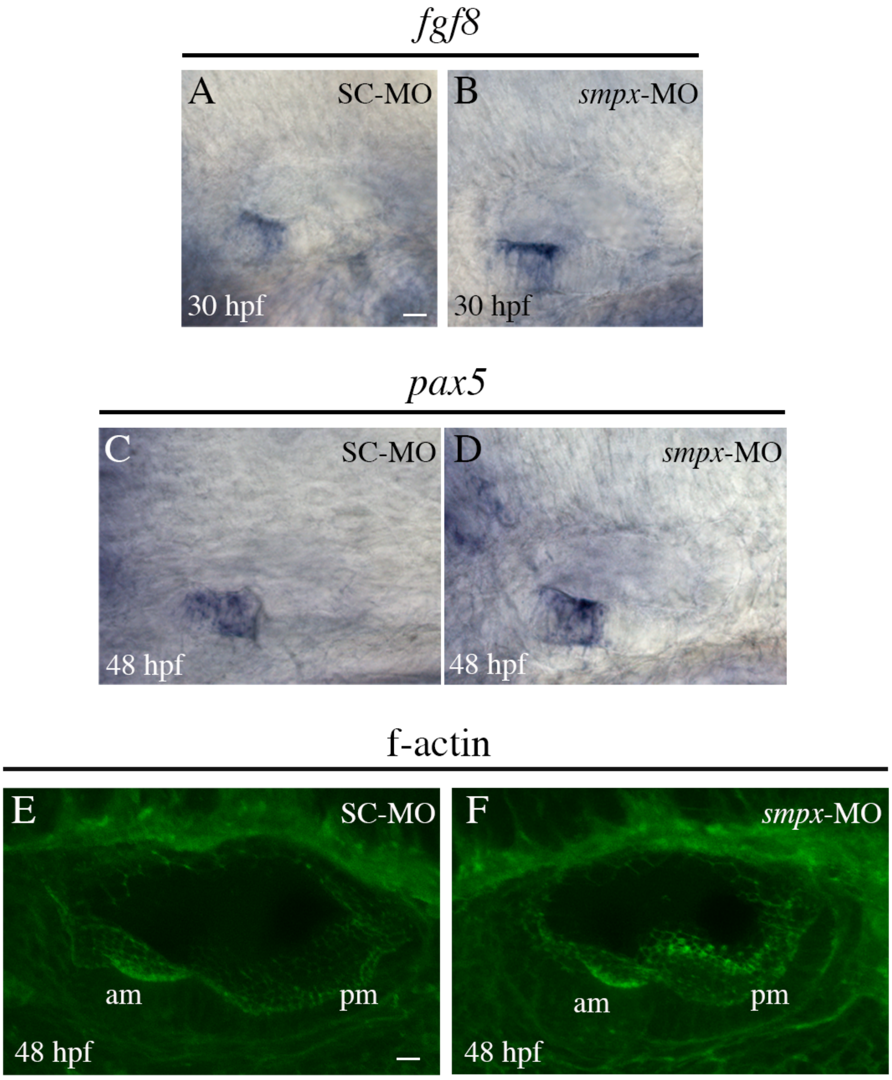

Fig. 14. *smpx* down-regulation does not affect the gross anatomy of the ear. (A, B) *fgf8* and (C, D) *pax5* expression at 30 and 48 hpf, respectively. (E, F) Confocal projection of 48 hpf morphant ear stained with FITC-phalloidin (green). *fgf8* and *pax5* WISH show no difference in the structure of the anterior macula in the (A, C) standard-controls when compared to (B, D) *smpx* morphants. The gross structure of the whole ear is maintained after *smpx* down-regulation. Abbreviations: am, anterior macula; pm, posterior macula.
Scale bar indicates 30 µm (A-D), 10 µm (E, F).

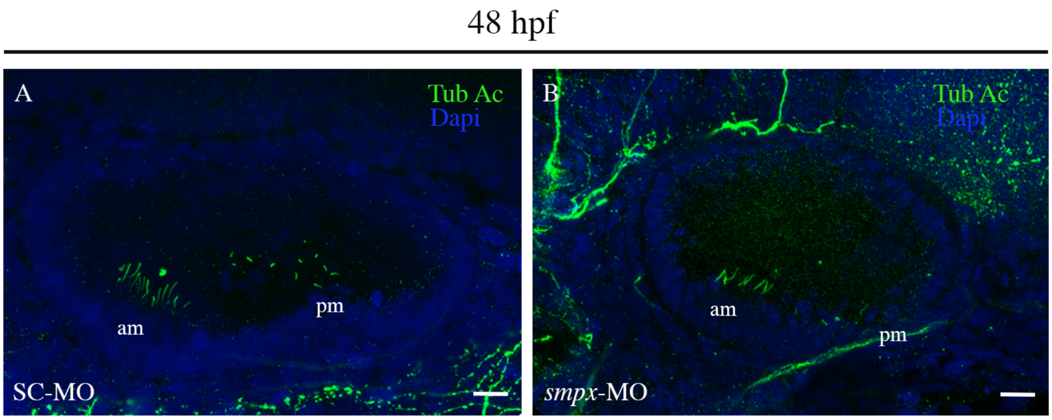

Fig. 15. Reduction in cilia number in *smpx* morphant embryos. Confocal projection of immunofluorescence performed with antibody against acetylated tubulin in 48 hpf (A) control- and (B) *smpx*-morphant embryos. *smpx* morphants display a lower number of cilia in the macular regions compared to control embryos.
Abbreviations: am, anterior macula; pm, posterior macula.
Scale bars indicate 10 µm.

Discussion

In this study we disclosed the role of the zebrafish *small muscle protein X-linked* gene, *smpx*, in crucial steps of embryonic development, and identified the potential cause leading to *SMPX*-linked NSHL in human. Furthermore, we pointed out the key role of *smpx* in zebrafish ciliogenesis, suggestive of a potential involvement of *SMPX* also in human ciliopathies.

Previous works associated *SMPX* mutations with hearing loss (Huebner *et al.*, 2011; Schraders *et al.*, 2011; Abdelfatah *et al.*, 2013). For such reason we embarked upon the project of trying modelling hearing loss phenotypes in zebrafish in order to gain insights into the events underlying this phenomenon. With this aim, we first investigated for *smpx* activity during zebrafish embryonic development from 0 to 72 hours post fertilization (hpf). The RT-PCR assay showed *smpx* expression starting from the 4-somite stage; interestingly, the mRNA at the earliest developmental stages (4 to 8 somites) was alternatively spliced, encoding two forms of the protein, a long form of 83 amino acid residues, and a short form, lacking of exon 3, of 54 amino acid residues. Indeed, later on and up to 72 hpf, only the long mRNA form is detectable. Although this alternative splicing has not been yet reported in any other organism before, we revealed the presence of several ESTs encoding the short form in other fish species and, intriguingly, also in the mammals *Heterocephalus glaber* and *Sus scrofa,* suggestive of a more widespread event concerning vertebrates. To elucidate the potentially different roles of the two protein forms during development, further experiments will be required.

By means of WISH assays we disclosed *smpx* expression at the 4-somite stage specifically in the Kupffer's vesicle (KV), a ciliated organ of asymmetry that establish the left-right body axis of zebrafish by creating a directional fluid flow through cilia beating (Essner *et al.*, 2005). From 10 somites to 24 hpf, *smpx* was expressed at the level of the somites and, at 24 hpf, started to be visible in the heart. At 72 hpf, *smpx* transcripts were detectable in the heart, in the branchial arches, and in the developing muscles of eye and pectoral fins. Starting from 36 hpf, *smpx* specific signal was visible in the ear, specifically in hair cells of the anterior and the posterior macula. Being human *SMPX* abundantly and specifically expressed in fetal skeletal muscle, heart and in fetal inner ears (Patzak *et al.*, 1999; Schraders *et al.*, 2011), similarly to murine *Smpx* (Palmer *et al.*, 2001), it is possible to conclude that the expression pattern of the gene is well conserved between zebrafish and the mammalian ortholog.

Of particular interest for our project was the expression of the gene in the zebrafish embryonic ear, which allowed us to set up a series of experiments of *smpx* functional ablation in order to assess the effect of the down-regulation on ear development. Although the knock-down of the gene did not alter the gross morphology of the inner ear, as showed by the conserved normal pattern of *fgf8* and *pax5* ear-specific markers, as well as by the normal aspect of the elaborate cytoskeleton of the hair cells (as shown by the phalloidin-mediated F-actin staining), we observed a noteworthy 40% reduction in the number of cilia in both the anterior and the posterior macular regions. This data strongly support the previously formulated hypothesis (Abdelfatah *et al.*, 2013), suggesting that SMPX protein deficiency in human could lead to a progressive hearing loss due to damages to the inner hair cells. Furthermore, being the gross morphology of the ear essentially normal, it is likely the involvement of Smpx in the maintenance of the hair cells rather then their proper development/differentiation, as also suggested by Yoon and colleagues (Yoon *et al.*, 2011). In order to analyze this hypothesis we plan to follow the development of the cilia in the hair cells at selected time points starting from the very beginning of their establishment. Macular organs in zebrafish are important for both hearing and for sensing linear acceleration and gravity (Nicolson, 2005). To understand if the decrease in the number of cilia in the macular regions may have consequences on the vestibular and auditory system in *smpx* morphants, the next step would be to assess embryos hearing capacities by a behavioral screening method that relies on the observation of the acoustically-triggered startle response (Bang *et al.*, 2002).

As mentioned above, the first site of *smpx* expression we identified was the ciliated KV, the equivalent of the mouse embryonic node, responsible for the body left-right patterning. Interestingly, besides ear cilia defects, another striking outcome of our functional assay was an abnormal body curvature, a feature usually associated with alterations in the ciliogenesis process in zebrafish (Serluca *et al.*, 2009). The potential involvement of *smpx* in cilia defects has been confirmed by the analysis of the position of the asymmetric organs in the morphant embryos, which indeed displayed the altered left-right patterning of the diencephalic habenular nuclei, the liver, and the pancreas, as well as the randomized looping of the heart. On these premises we analysed in more details the KV in morphant embryos. Although *smpx*-deficient embryos displayed a fully formed KV, the structure was characterized by a marked decrease in the number of cilia (less of 50%) when compared to the KV of control embryos, indicative of a KV-lack of functionality determined by the drastic drop in the amount of cilia, in agreement with previous studies supporting the hypothesis that a defective flow within the KV, due to the reduced number of cilia, resulted in heterotaxy, the randomization of left-right visceral organ situs (Sampaio *et al.*, 2014). As for the ear hair cells, in order to discriminate in between cilia development versus maintenance, we plan to follow the development of the KV since the beginning of its formation.

The wealth of data reported in this study strongly supports the notion of the important role of *smpx* in the process of developing and/or maintaining zebrafish cilia. Such evidences shed some light on the cause of hearing loss in SMPX-defective patients, allowing us to propose zebrafish as a suitable system to elucidate the mechanisms lying behind the disability. Additionally, this work identified a novel, unexpected effect of Smpx-deficiency on zebrafish embryos, meaning impairment of the left-right patterning of visceral organs. On this basis, considering the high degree of gene function conservation between zebrafish and human, it is possible to hypothesize potential links concerning SMPX and heterotaxy. Indeed, despite the heavy genetic contribution to human heterotaxy, the vast majority of cases remain unexplained; in this scenario, the employment of animal models such as zebrafish may speed up the identification of novel genetic causes leading to this heritable disorder. At this juncture, we are planning the screening of a cohort of patients affected by X-linked heterotaxy already tested for the known loss of function mutations in *ZIC3*, the only gene associated with *situs inversus* and positioned on the X chromosome (Ware *et al.*, 2004).

In conclusion, this study contributes to the comprehension of the link between *SMPX* and human hearing loss, delivers a novel heterotaxy-candidate gene, and finally provides a robust animal tool for the future elucidation of the mechanisms behind both deafness/hearing loss and heterotaxy.

Experimental Procedures

Zebrafish Strains

We used AB zebrafish strains for all experiments. Breeding wild type fish of the AB strain were maintained at 28°C on a 14 h light/10 h dark cycle. Wild-type zebrafish embryos were obtained through natural matings, raised at 28°C in the presence of 0.002% Methylene Blue and 0.003% PTU (1-phenyl-2-thiourea) to block pigmentation, and staged as described (Kimmel *et al.*, 1995).

RT-PCR

Total RNA from 10 samples (an average of 30 embryos per sample) corresponding to 10 different developmental stage embryos (1–2 cells, Oblong, 30% epiboly, 90% epiboly, tailbud, 2 somites, 4 somites, 8 somites, 24 hpf, 48 hpf and 72 hpf) was extracted with the SV Total RNA Isolation System (Promega) and reverse transcribed with the ImProm-II™ Reverse Transcriptase kit (Promega), according to manufacturers' instructions. The following primers were used for the subsequent PCRs:

*smpx*_F0*:* 5'-TTGACATTTGTGTCTGACACCA (forward)
*smpx*_F1*:* 5'-ACTGCACACAATGTCAAAACA (forward)
*smpx*_R1*:* 5'-CACCTGAGCCAATTTAGTCTT (reverse)
*β-actin*_F*:* 5'-TGTTTTCCCCTCCATTGTTGG (forward)
*β-actin*_R*:* 5'-TTCTCCTTGATGTCACGGAC (reverse)

PCR products were loaded and resolved onto 2% agarose gels.

The *smpx*_F1/*smpx*_R1 amplicon has been gel extracted and cloned in the pSC-A-amp/kan and pCMV-SC vectors (Strataclone) in order to *in-vitro* transcribe the smpx-specific sense/antisense RNA probes and the synthetic mRNA, respectively.

Morpholino and mRNA microinjection

Embryos were injected at the one- to four-cell stage with ~4 nl using freshly pulled micropipettes attached to the FemtoJet precision pressurized injector (Eppendorf); the dye tracer rhodamine dextran (Invitrogen) was also coinjected. To repress *smpx* mRNA translation, the following ATG-targeting morpholino (Gene Tools, LLC) has been synthesized: 5'-AGCAGCAGGAACGTGGACACAACTG-3'. *smpx* morpholino (*smpx*-MO) was used at the concentration of 0.35 pmole per embryo in Ringer's solution (pH 7,3) according to the Gene Tool's protocol. As control a standard control morpholino oligonucleotide (SC-MO) has been injected. For Smpx over-expression, synthetic capped *smpx* mRNA was synthesized with the mMessage mMachine® SP6 kit (Ambion) and injected at the concentration of 300 pg per embryo. 300 pg/embryo of synthetic capped GFP mRNA was synthesized with the same Ambion kit and injected as control.

In-situ hybridization

Whole mount *in-situ* hybridization (WISH), was carried out as previously described (Thisse *et al.*, 1995) on embryos fixed overnight in 4% paraformaldehyde/PBS, then rinsed with PBS-Tween, dehydrated in 100% methanol and stored at -20°C until processed for WISH (Jowett and Lettice, 1994). Antisense riboprobes were previously *in-vitro* labelled with modified nucleotides (digoxigenin or fluorescein, Roche). Embryos were imaged by Digital Camera DCF480 (Leica) and software LAS (Leica Application Suite, Leica) on a MZFLIII microscope (Leica).

Phalloidin staining and immunostaining

Immunostaining was performed according to routine protocol. Briefly, fresh embryos were fixed overnight in 4% paraformaldehyde/PBS, then incubated with mouse anti-acetylated α-tubulin IgG (Sigma) and goat anti-mouse Alexa^{488} (Invitrogen). Embryos were counterstained with 4’,6-diamidino-2-phenylindole (DAPI) to visualize cell nuclei.
For visualization of actin using phalloidin staining, embryos were fixed as above, followed by overnight incubation in 1:20 FITC-phalloidin (Sigma). Embryos were confocally imaged with the TCS SP5 microscope (Leica). The number of cilia and their location was determined from inspections of *z*-stacks of up to 200 0.2-1.0 μm optical sections. *z*-stacks were converted into projections that merged optical sections into one image.

References

Abdelfatah N, Merner N, Houston J, Benteau T, Griffin A, Doucette L, Stockley T, Lauzon JL, Young T (2013). A novel deletion in *SMPX* causes a rare form of X-linked progressive hearing loss in two families due to a founder effect. *Hum. Mutat*. 34, 66-69.

Bang PI, Yelick PC, Malicki JJ, Sewell WF (2002). High-throughput behavioral screening method for detecting auditory response defects in zebrafish. *J. Neurosci. Methods* 118:177-187

Essner JJ, Amack JD, Nyholm MK, Harris EB, Yost HJ (2005). Kupffer's vesicle is a ciliated organ of asymmetry in the zebrafish embryo that initiates left-right development of the brain, heart and gut. *Development* 132:1247–1260.

Fliegauf M, Benzing T and Omran H (2007). When cilia go bad: cilia defects and ciliopathies. *Nat. Rev. Mol. Cell. Biol.* 8:880-893.

Graham JL and Currie PD (2007). Animal models of human disease: zebrafish swim into view. *Nat. Rev. Gen.* 8: 353-367.

Huebner AK, Gandia M, Frommolt P, Maak A, Wicklein EM, Thiele H, Altmuller J, Wagner F, Vinuela A, Aguirre LA, Moreno F, Maier H, *et al.* (2011). Nonsense mutations in SMPX, encoding a protein responsive to physical force, result in X-chromosomal hearing loss. *Am. J. Hum. Genet.* 88, 621–627.

Jowett T, Lettice L (1994). Whole-mount in situ hybridizations on zebrafish embryos using a mixture of digoxigenin and fluorescein-labelled probes. *Trends Genet.* 10:73-74.

Kemp TJ, Sadusky TJ, Simon M, Brown R, Eastwood M, Sassoon DA, Coulton GR (2001). Identification of a novel stretch-responsive skeletal muscle gene (SMPX). *Genomics* 72:260–271.

Kimmel CB, Ballard WW, Kimmel SR, Ullmann B, Schilling TF (1995). Stages of embryonic development of the zebrafish. *Dev. Dyn.* 203:253-310.

Kwak S, Vemaraju S, Moorman SJ, Zeddies D, Popper AN, Riley BB (2006). Zebrafish *pax5* regulates development of the utricular macula and vestibular function. *Dev. Dyn.* 235:3026-3038.

Nicolson T (2005). The genetics of hearing and balance in zebrafish. *Annu. Rev. Genet.* 39:9–22.

Palmer S, Groves N, Schindeler A, Yeoh T, Biben C, Wang CC, Sparrow DB, Barnett L, Jenkins NA, Copeland NG, Koentgen F, Mohun T, et al. (2001). The small muscle-specific protein Csl modifies cell shape and promotes myocyte fusion in an insulin-like growth factor 1-dependent manner. *J. Cell. Biol.* 153:985–998.

Patzak D, Zhuchenko O, Lee CC, Wehnert M. (1999). Identification, mapping, and genomic structure of a novel X-chromosomal human gene (SMPX) encoding a small muscular protein. *Hum. Genet.* 105:506–512.

Phillips JB, Blanco-Sanchez B, Lentz JJ, Tallafuss A, Khanobdee K, Sampath S, Jacobs ZG, Han PF, Mishra M, Titus TA, *et al.* (2011). Harmonin (Ush1c) is required in zebrafish Müller glial cells for photoreceptor synaptic development and function. *Dis. Model Mech.* 4:786–800.

Pistocchi A, Gaudenzi G, Carra S, Bresciani E, Del Giacco L, Cotelli F (2008). Crucial role of zebrafish prox1 in hypothalamic catecholaminergic neurons development. *BMC Dev. Biol.* 8:27.

Reifers F, Böhli H, Walsh EC, Crossley PH, Stainier DY, Brand M (1998). Fgf8 is mutated in zebrafish acerebellar (ace) mutants and is required for maintenance of midbrain-hindbrain boundary development and somitogenesis. *Development* 125:2381-2385.

Schindeler A, Lavulo L, and Harvey RP (2005). Muscle costameric protein, Chisel/Smpx, associates with focal adhesion complexes and modulates cell spreading in vitro via a Rac1/ p38 pathway. *Exp. Cell Res.* 307, 367–380.

Schraders M, Haas SA, Weegerink NJD, Oostrik J, Hu H, Hoefsloot LH, Kannan S, Huygen

PLM, Pennings RJE, Admiraal RJC, *et al*. (2011). Next-Generation sequencing identifies mutations of SMPX which encodes the small muscle protein, X-linked, as a cause of progressive hearing impairment. *Am. J. Hum. Genet*. 88, 628–634.

Serluca FC, Xu B, Okabe N, Baker K, Lin SY, Sullivan-Brown J, Konieczkowski DJ, Jaffe KM, Bradner JM, Fishman MC *et al*. (2009). Mutations in zebrafish leucine-rich repeat-containing six-like affect cilia motility and result in pronephric cysts, but have variable effects on left-right patterning. *Development* 136:1621–1631.

Sampaio P, Ferreira RR, Guerrero A, Pintado P, Tavares B, Amaro J, Smith AA, Montenegro-Johnson T, Smith DJ, Lopes SS. (2014). Left-Right organizer flow dynamics: how much cilia activity reliably yields laterality? *Dev. Cell*. 29:716-728

Sutherland MJ, Ware SM (2009) Disorders of left-right asymmetry: heterotaxy and situs inversus. *Am. J. Med. Genet. C. Semin. Med. Genet*, 151C:307-317.

Thisse C, Thisse B, Schilling TF, Postlethwait JH (1993). Structure of the zebrafish snail1 gene and its expression in wild-type, spadetail and no tail mutant embryos. *Development* 119:1203-1215.

Ware SM, Peng J, Zhu L, Fernbach S, Colicos S, Casey B, Towbin J, Belmont JW (2004). Identification and functional analysis of ZIC3 mutations in heterotaxy and related congenital heart defects. *Am. J. Hum. Genet*. 74:93-105

Wei X, Zhao L, Liu J, Dodel RC, Farlow MR, Du Y (2005). Minocycline prevents gentamicin-induced ototoxicity by inhibiting p38 MAP kinase phosphorylation and caspase 3 activation. *Neuroscience* 131, 513–521.

Whitfield TT (2002). Zebrafish as a model for hearing and deafness. *J. Neurobiol*. 53:157-71.

Whitfield TT, Granato M, van Eeden FJM, Schach U, Brand M, Furutani-Seiki M, Haffter P, Hammerschmidt M, Heisenberg C-P, Jiang Y-J, Kane DA, Kelsh RN, Mullins MC, Odenthal J, Nüsslein-Volhard C. (1996). Mutations affecting development of the zebrafish inner ear and lateral line. *Development* 123:241–254.

Yelon D, Horne SA and Stainier DY (1999). Restricted expression of cardiac myosin genes reveals regulated aspects of heart tube assembly in zebrafish. *Dev. Biol.* 214, 23-37.

Yoon H, Lee DJ, Kim MH, Bok J (2011). Identification of genes concordantly expressed with *Atoh1* during inner ear development. *Anat. Cell. Biol.* 44:69-78.

Acknowledgement

I am deeply grateful to Telethon Foundation that fully supported this work and gave me the opportunity to realize my PhD student project funding my fellowship. I also want to thank the Cariplo Foundation that financed part of this experimental laboratory research.

Part II

List of published papers

1. La Porta C.A.M., **Ghilardi A.**, Pasini M., Laurson L., Alava M.J., Zapperi S., Amar M.B. (In Press) Osmotic stress affects functional properties of human melanoma cell lines. *Journal of the Royal Society Interface.*

2. Beghini A., Corlazzoli F., Del Giacco L., Re M., Lazzaroni F., Brioschi M., Valentini G., Ferrazzi F., **Ghilardi A.**, Righi M., Turrini M., Mignardi M., Cesana C., Bronte V., Nilsson M., Morra E., Cairoli R. (2012) Regeneration-associated Wnt signaling is activated in long-term reconstituting AC133^{bright} acute myeloid leukemia cells. *Neoplasia,* **14(12)**:1236-1248.

3. Guella I., Pistocchi A., Asselta R., Rimoldi V., **Ghilardi A.**, Sironi F., Trotta L., Primignani P., Zini M., Zecchinelli A., Coviello D., Pezzoli G., Del Giacco L., Duga S., Goldwurm S. (2011) Mutational screening and zebrafish functional analysis of *GIGYF2* as a Parkinson-disease gene. *Neurobiology of Aging*, **32(11)**:1994-2005.

4. Del Giacco L., Pistocchi A., **Ghilardi A.** (2010) *prox1b* Activity is essential in zebrafish lymphangiogenesis. *PLoS One*, **5(10)**:e13170.

Osmotic stress affects functional properties of human melanoma cell lines

Caterina A. M. La Porta[1] Anna Ghilardi[1], Maria Pasini[1], Lasse Laurson [2], Mikko J. Alava [2], Stefano Zapperi[3,4] and Martine Ben Amar[5,6]*

[1] Department of Biosciences, University of Milano, via Celoria 26, 20133 Milano, Italy
[2] COMP Centre of Excellence, Department of Applied Physics, Aalto University, P.O. Box 14100, FIN-00076 Aalto, Espoo, Finland
[3] CNR-IENI, Via R. Cozzi 53, 20125 Milano, Italy
[4] ISI Foundation, Via Alassio 11C, 10126 Torino, Italy
[5] Laboratoire de Physique Statistique, Ecole Normale Supérieure, UPMC Univ Paris 06, Université Paris Diderot, CNRS, 24 rue Lhomond, 75005 Paris, France
[6] Institut Universitaire de Cancérologie, Faculté de médecine, Université Pierre et Marie Curie-Paris 6, 91 boulevard de l'hôpital, 75013 Paris, France

Abstract

Understanding the role of microenvironment in cancer growth and metastasis is a key issue for cancer research. Here, we study the effect of osmotic pressure on the functional properties of primary and metastatic melanoma cell lines. In particular, we experimentally quantify individual cell motility and transmigration capability. We then perform a circular scratch assay to study how a cancer cell front invades an empty space. Our results show that primary melanoma cells are sensitive to a low osmotic pressure, while metastatic cells are less. To better understand the experimental results, we introduce and study a continuous model for the dynamics of a cell layer and a stochastic discrete model for cell proliferation and diffusion. The two models capture essential features of the experimental results and allow to make predictions for a wide range of experimentally measurable parameters.

1 Introduction

The microenvironment is a key factor in tumour development and progression. Its influence on the behaviour of cancer cells is to a great extent mediated by the composition, structure, and dimensionality of the extracellular matrix, the polymeric scaffold that surrounds cells within tissues. Research shows that the mechanical properties of tumour microenvironment can facilitate or oppose tumour growth and dynamics, although this effect is poorly understood. Mechanical stresses such as those experienced by cancer cells during the expansion of the tumour against the stromal tissue have been shown to release and activate growth factors involved in the progression of cancer [14]. Moreover, the stiffness of the matrix surrounding a tumour determines how cancer cells polarize, adhere, contract, and migrate, thus regulating their invasiveness [14]. Another possibility is that mechanical stresses directly regulate the growth and death rates of cancer cells. Recently, Montel et al. have explored this possibility, investigating the effect of a constant stress applied on cellular spheroids over long time scales by inducing osmotic pressure by a solution of dextran, a biocompatible polymer which is neutral and can not metabolised by mammalian cells [11, 12]. Using a similar method, some of us recently reported that a constant low osmotic pressure (1KPa) affects more strongly the proliferative capability of primary human melanoma cells (IgR39) in comparison to the corresponding metastatic ones (IgR37) [20]. Furthermore, a computer simulation analysis of the growth of melanocytic nevi inside epidermal or dermal tissues shows that the shape of the nevi is correlated with the elastic properties of the surrounding tissue[20].

Several studies in the literature reported important changes in cellular functioning due to osmotic pressure [15, 13], but the stresses involved (in the MPa range) were orders of magnitude larger than those (in the kPa range) studied in Refs. [11, 12, 20]. It is interesting to notice that compressive stresses of slightly less than 1 kPa applied through a piston were recently found to induce a metastatic phenotype in cancer cells [21]. In a recent paper, Simonsen et al. showed that interstitial fluid pressure (IFP) was associated with high geometric resistance to blood flow caused by tumour-line specific vascular abnormalities in xenografted tumours from two human melanoma lines with different angiogenic profiles [18]. In another recent paper, Wu *et al* investigated how nonlinear interactions among the vascular and lymphatic networks and proliferating tumour cells might influence IFP transport of oxygen, and tumour progression [22]. They also investigated the possible consequences of tumour-associated pathologies such as elevated vascular hydraulic conductivities and decreased osmotic pressure differences. All these parameters might affect microenvironmental transport barriers, and the tumour invasive and metastatic potential, opening interesting new therapeutic perspectives. In general, understanding the influence of mechanical stress on cancer growth could shed new light on tumour development and progression. Studies present in the literature also use hypertonic conditions, but the effects are always observed at high osmotic pressure [7, 10].

In this paper, we show that low osmotic pressure (1KPa) beside proliferation, which was the focus of previous works [11, 12, 20], also modulates key functional biological aspects of cancer cells such as their motility and transmigration, possibly contributing to the acquisition of a more aggressive phenotype. Melanoma is an aggressive, radio- and chemo-resistant tumour which becomes impossible to cure when metastasised. Therefore, a pressing clinical problem in the treatment of melanoma is to understand how to stop or prevent the capability of the tumour to give rise metastasis. Using an interdisciplinary approaches combining cellular biology and theoretical physics, here we show that a low osmotic pressure (1KPa) leads significant changes in cell F-actin organization compromising the capability of the cells to move and transmigrate. Interestingly, osmotic pressure shows a more efficacy on the primary human melanoma cell line with respect to the metastatic once belonging to the same patient. We perform quantitative analysis on the experimental data and extract parameters for cell motilities that we can then use in a continuum theory and a discrete model for cancer cell front dynamics. Overall, our results show that osmotic pressure can contribute to the selection of subpopulation in the primary human melanoma cells contributing to the acquisition of a more aggressive phenotype.

2 Experimental results

2.1 Effect of osmotic pressure on F-actin organization

The organization of F-actin in the two human melanoma cell lines is shown in Figure 1 under normal growth condition or 1KPa osmotic pressure without or with collagen as physiological substrate. In both cell lines, 1KPa induces a rearrangement in F-actin organization (Fig. 1). In particular in IgR39, 1KPa osmotic pressure induces the appearance of filopodia and stress fibers (Fig. 1a-b) Similar changes have been shown plating the cells on a collagen pre-coated Petri dish (Fig. 1c-d). The metastatic cell line IgR37 shows, however, a little effect of osmotic pressure displaying a more elongated shape (Fig.1e-f).

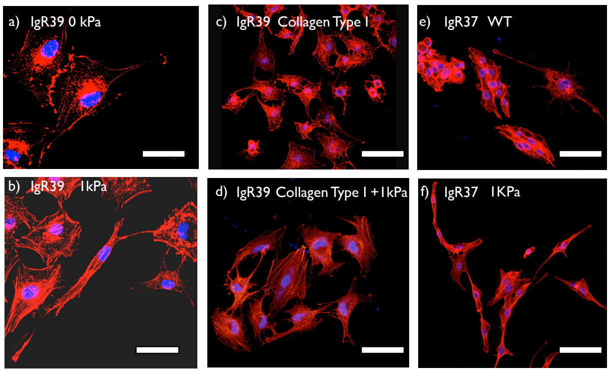

Fig. 1 Effect of osmotic pressure on F-actin. Subconfluent cells were plated on 33cm^2 Petri dish untreated or pre-coated with type I collagen. After 6 days the cells were fixed with 3.7% paraformaldeide and incubated with Red-Falloidin for 30min at room temperature. The nuclei were counterstained with DAPI and the slides were mounted with Pro-long anti fade reagent (Invitrogen). The images were acquired using a Leika TCS NT confocal microscope. Panel a-d represent IgR39 cells and panel e-f IgR37 cells. Scale bar is 50μm

2.2 Effect of osmotic pressure on transmigration capability of IgR39 and IgR37 human melanoma cells

An important function needed by cancer cells in order to metastasise is the ability to bypass an obstacle such as an endothelial wall. To simulate this process in vitro, we use a transwell assay counting the number of cells that are able to pass through 8μm wide pore after 6 hours in presence of a chemoattractant (10%FBS). Without chemoattractant the cells barely overcome the obstacles, although metastatic cells are intrinsically more capable to do this (Table 1). Figure 2 shows a significantly decrease of transmigration capability when cells are treated for six days with a 1kPa osmotic pressure. The decrease is by a factor 4 for IgR39 and by a factor 2 for IgR37 with respect to the untreated ones (Table 1).

2.3 Effect of osmotic pressure on circular scratch assay of IgR39 human melanoma cells.

We study the biological effect of 1kPa osmotic pressure on the capability of the cells to cover a free space using a circular scratch assay. As shown in Fig. 3, the circular shape of the ring is maintained during up to 96 hours, suggesting that the cells move isotropically into the free space. Moreover, in Table 2 is shown that osmotic pressure induces a little effect on the migration capability to cover the free area (around 4%). By

	IgR39 0kPa	IgR37 0kPa	IgR39 1kPa	IgR37 0kPa
without FBS	103 ± 1.4	602 ± 74	68 ± 11	387 ± 57
+FBS	1704 ± 388	1925 ± 173	269 ± 21	825 ± 125

Table 1 Result of the transwell assay for primary and metastatic human melanoma cells with and without osmotic pressure. The results are the mean number of cells crossing pores averaged over three independent experiments. Error bars correspond to the standard error.

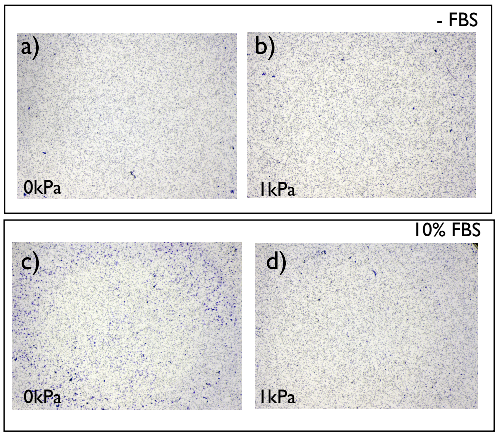

Fig. 2 Transwell Assay. 70000 cells are plated to each transwell insert (8μm pores) into the upper chamber. In the lower chamber 600μl medium without FBS (-FBS) or when 10% FBS is added. After 6 hours the cells are fixed and stained in a 20% methanol/0.1% crystal violet solution for three minutes at room temperature, followed by washing in deionized water to remove redundant staining. Non-migrated cells remaining at the upper side of the membranes, are carefully removed with cotton swabs and inserts are dried in darkness overnight. Pictures of the entire Petri dish are made with a Leika MZFL11 microscope mounted with a camera Leika DFC 32. The blue cells are counted using the magnified images (25X) and then calculated for the whole surface (32cm^2).

observing the cells at higher magnification, we notice that the structure of the front is affected by osmotic pressure becoming more scattered 3b-c. The effect might be due to changes in either their proliferative capability or in their motility due to cytoskeleton changes observed in Fig. 1. Colony formation assays reported in Ref. [20] for the same cells, show that the rate of division decreased from $k_{\text{div}} = 0.60$ to $k_{\text{div}} = 0.51$ under the effect of 1kPa of osmotic pressure.

We also investigate if the proliferative capacity of the cells are different at the border of the ring or at the edge of the Petri dish. As shown in Fig. 4, no significant differences of proliferation have been shown using Ki67, a known proliferative marker, between the centre of the dish and the edge (Fig. 4 shows the expression at 72 hours, similar results was obtained at 24 and 48 hours). Regarding to IgR37 we did not carry out this kind of experiment since these cells do not grow as a monolayer and it is impossible to get a homogeneous confluent layer.

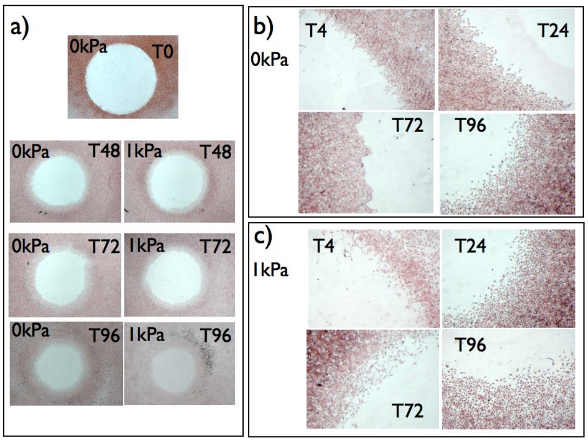

Fig. 3 Circular scratch assay. Cells were plated on 33cm^2 Petri dish with at the center a ring (32mm^2) at confluence. The day after the ring was removed and the cells were fixed with 3.7% paraformaldeide and stained with hematoxillin/eosin solution at different times. The same experiment was carried out on cells treated with 1KPa osmotic pressure. Panel a shows a typical experiment at magnification 8X; Panel b-c show details from the same images at magnification 40X. The images were acquired with LEICA MZFLIII mounted with a camera LEICA DFC320.

2.4 Osmotic pressure affects cell motility

To investigate the effect of osmotic pressure on cell motility, we reconstruct cell trajectories from confocal images (see 5a). We use IgR39 cells since these cells are the ones that are most affected by osmotic pressure [20]. To quantify cell motility we compute the typical width of the trajectories $W = \langle (R(t) - \langle R \rangle)^2 \rangle$, where the average is taken over all time frames and 4 different cells for each experimental condition. Fig. 5b shows that osmotic pressure reduces the average excursions of the cells. Next, we compute the time dependence of the mean square displacement $\langle (R(t+t') - R(t'))^2 \rangle$ which

Time [hours]	Pressure [KPa]	Ring area [mm^2]	% of area covered
0	0	32	0
48	0	16	50
48	1	16.5	48
72	0	15.5	52
72	1	16	50
96	0	11.2	68
96	1	11.8	65

Table 2 The table shows a typical example of the free circle area and the percentage of covered area obtained from Fig. 3.

increases roughly linearly in time (Fig. 5c) as would be expected for a Brownian motion. The slope of the linear slope can be used to estimate the diffusion coefficient resulting in $D = 0.016(\mu\mathrm{m})^2/\mathrm{s}$ at 0kPa and $D = 0.004(\mu\mathrm{m})^2/\mathrm{s}$ at 1kPa. To confirm the Brownian nature of the process, we compute the power spectrum $S(\omega)$ of the trajectories, showing that it decays approximately as $1/\omega^2$ as expected for a random walk.

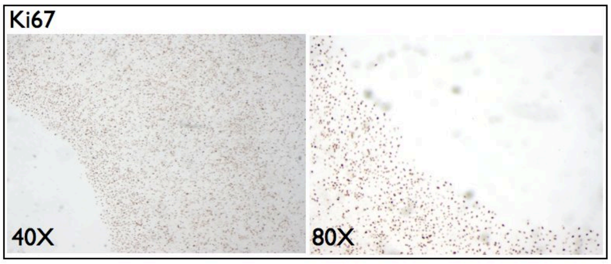

Fig. 4 Ki67 Immunohystochemistry IgR39 cells were plated on 33cm^2 Petri dish with at the center a ring (32mm^2) at confluence. 72 hours after the ring was removed and the cells were fixed with 3.7% paraformaldeide and stained overnight with anti-mouse Ki67 (1:100, DAKO). After a brief incubation for 30min with biotinylated anti-mouse secondary antibody(Dako, 1:100), the cells were incubated with streptavidin (Dako, 1:350) conjugated to peroxidase for 30min. Color was routinely developed using DAB peroxidase substrate kit (Vector) up to 10 min and coverslipped with a permanent mounting medium.

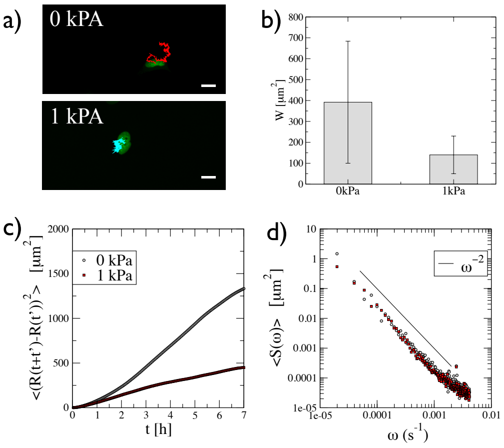

Fig. 5 Cell motility. Subconfluent cells plated in a 35cm^2 Petri dish untreated or treated for 6 days with 1kPa of osmotic pressure are transfected with H2B-GFP plasmide. Pictures are made on a confocal microscope (Leica TCS SP5 AOBS with resonant scanner, equipped with a 20X, 0.5 NA, dry objective) every 4 minutes for 14 hours. a) Typical trajectories for IgR39 cells untreated and under osmotic pressure. b) The width of the trajectories is reduced under osmotic pressure. c) The average displacement grows roughly linearly with a typical slope that depends on the osmotic pressure. d) The Brownian nature of the motion is confirmed by the power spectrum of the trajectories that decays as ω^{-2}.

3 A continuous model for advancing cell front

Since the main objective of our work is to study the effect of mechanical stress on an layer made of cancerous cells, we propose a physical model to explain and quantify the observations. As shown in Table 2 , we get a strong decrease of the surface hole, about 50%, the first 2 days, then a period without proliferation followed by a new decrease which is less abrupt. The effect is a little less acute if an over-pressure is added via addition of dextran. For an advancing layer under chemotaxis, a continuous model has already been proposed by [2, 3], but these works are not concerned by a proliferative layer submitted eventually to an overpressure due to an osmotic solution. In addition, proliferation is not considered in the advance of a layer experimentally but here our experiment clearly shows that it cannot be discarded.

Let us consider a layer of constant thickness in a domain Ω with a border $\delta\Omega$. The cell displacement in Ω is mostly driven by the cell proliferation, but at the border the cells may be more proliferative eventually and even detach and move freely. Due to proliferation, the mass conservation equation is then transformed into:

$$\frac{\partial \rho_0}{\partial t} + \vec{\nabla}(\rho_0 \vec{V}) = -k_v(\tilde{P} - P_h), \quad (1)$$

where P_h is the homeostatic pressure for which cell proliferation just compensates apoptosis, ρ_0 is the constant mass density, $\vec{V}$ is the velocity at an arbitrary point of Ω. This simple idea about regulation in living systems is due to Claude Bernard, a french physiologist, in 1865 [4]. Mathematically, such a continuous model is valid at a scale larger than the cell size and the velocity is an averaged quantity on a sample of intermediate scale between the single cell and the full layer. Adding dextran to the solution increases the pressure $\tilde{P}$, slightly inhibiting the proliferation rate. For a layer crawling on a substrate in strong adhesion, the second Newton's law of dynamic simplifies into a Darcy law ([8, 2])

$$\vec{V} = -\frac{1}{M}\nabla \tilde{P}, \quad (2)$$

where the mobility coefficient M is related to the friction coefficient. Combining both equations gives:

$$\Delta P - \alpha^2 P = 0 \text{ with } P = \tilde{P} - P_h \quad (3)$$

and $\alpha^2 = k_v M/\rho_0$. At the free interface, boundary conditions include the mechanical equilibrium and the front velocity. The pressure at the layer border $\tilde{P}_i$ is equal to the pressure of the solution (if capillary effect is neglected). It is smaller at the interface $\delta\Omega$ than in the layer bulk Ω for a proliferative layer. The interface velocity $\vec{\delta\Omega}_t$ is given by the velocity of the cells at the interface which may be different from the cells in the bulk Ω. Indeed, these peripheral cells have more room both for displacement and proliferation. Then the normal front velocity $\vec{\delta\Omega}_t$ is given by

$$\vec{N} \cdot \vec{\delta\Omega}_t = -\frac{1}{M}\vec{N} \cdot \vec{\nabla} P + \vec{N} \cdot \vec{v}_s \quad (4)$$

where $\vec{v}_s$ may represent a specific proliferation rate of the border cells. It may exist other boundary conditions due to the geometry of the experiment, it is why we consider now 3 different growth geometries.

3.1 Growing circular disc

We imagine a disc of a cell monolayer and assume that the growth process preserves the circular geometry. Eq.(3) for the pressure $P = \tilde{P} - P_h$ is then transformed into an ordinary differential equation of second order:

$$\frac{1}{R}\frac{d}{dR}\left(R\frac{dP}{dR}\right) = \alpha^2 P \quad (5)$$

The regular solution at the origin is the modified Bessel function of zero order I_0 so

$$P(R) = P_i \frac{I_0(\alpha R)}{I_0(\alpha R_i(t))} \quad (6)$$

and $P_i = \tilde{P}_i - P_h$ is negative, being fixed by the nutrient medium, whatever the hole radius $R_i(t)$. From Darcy's law (Eq.(2)), we derive the growing velocity at the interface:

$$\vec{N} \cdot \delta\Omega_t = \dot{R}_i(t) = -P_i \frac{\alpha}{M} \frac{I_1(\alpha R_i(t))}{I_0(\alpha R_i(t))} \quad (7)$$

which is an implicit equation for the time variation of the radius which can be solved numerically. However one can make an asymptotic analysis of Eq.(7) and gets a constant growth rate at long times :

$$\dot{R}_i(t)|_{t\to\infty} \to -P_i \frac{\alpha}{M}$$

and a radius growing linearly in time. However, it is to be noticed that a constant proliferation rate into Eq.(1) will lead to an exponential time behaviour for the radius so to follow the growth expansion of the layer at long times may be a good test for the validation of the model.

3.2 A hole in an infinite layer

In this case, we can accept the irregular Bessel function at the center K_0 as the solution of Eq.(5), but not I_0, which grows exponentially. The solution reads

$$P(R) = P_i \frac{K_0(\alpha R)}{K_0(\alpha R_i(t))}. \quad (8)$$

The pressure P vanishes at infinity where there is no cell proliferation. The velocity given by Darcy's law is then:

$$\dot{R} = \frac{\alpha}{M} P_i \frac{K_1(\alpha R)}{K_0(\alpha R_i(t))} \quad (9)$$

being negative as P_i and vanishing as $R \to \infty$ as expected. Here again the radius of the hole is given numerically if we take Eq.(4) on the interface. In addition, the radius velocity diverges when the total cover of the hole is reached, and the continuous model stops to be valid for $R_i(t) \to 0$.

3.3 The circular scratch assay

Here we focus on the geometry of the circular scratch assay which is made of a planar annulus of cells limited by a plastic circular wall at $R = R_e$. The outer interface is rather diffuse but an average circular border can be defined. In addition a thin circular ring (of thickness δ) with smaller cell density can be observed appearing less contrasted than the inner core.

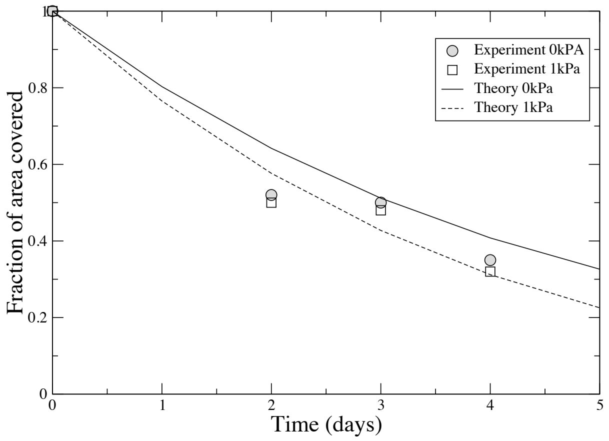

Fig. 6 Relative area of the hole as a function of time for theory and experiments (see Table 2). Parameters for the theory are $P_i = -1$ for 0kPa and $P_i = -0.98$ for 1kPa, $\alpha = 0.71, \delta = 0.3$ (with initial radius 1), $\tau = 1$.

We will adapt the previous model to this inhomogeneous ring which has a density ρ_i for R between $R_i(t)$ and $R_i(t) + \delta$ while the density in the bulk ($R_i(t) + \delta < R < R_e$) is called ρ_e . We take constant both ρ values. Moreover, in vitro, it has been shown that in confluent layers, live cell extrusion is induced to recover the homeostatic state in case of over-crowding and it is clear that the border allows more easily such extrusion [9]. So we presume that $\rho_i < \rho_e$.

Because the layer geometry excludes $R = 0$ and $R \to \infty$, possible solutions for Eq.(5) are superposition of I_0 and K_0 and we get

$$P^i(R) = \frac{P_i}{1+b}\Big(\frac{I_0(\alpha_i R)}{I_0(\alpha_i R_i(t))} + b\frac{K_0(\alpha_i R)}{K_0(\alpha_i R_i(t))}\Big) \tag{10}$$

with $\alpha_i^2 = k_v M/\rho_i$. The velocity of the cells at the outer border being :

$$\dot{R}^i = -\frac{\alpha_i}{M}\frac{P_i}{1+b}\Big(\frac{I_1(\alpha_i R)}{I_0(\alpha_i R_i(t))} - b\frac{K_1(\alpha_i R)}{K_0(\alpha_i R_i(t))}\Big) \tag{11}$$

P_i keeps the same definition as before : the pressure in the solution minus the homeostatic pressure. For $R_i(t) + \delta < R < R_e$ we have:

$$P^e(R) = P_e\Big(\frac{I_0(\alpha_e R)}{I_1(\alpha_e R_e)} + \frac{K_0(\alpha_e R)}{K_1(\alpha_e R_e)}\Big)) - \tau \tag{12}$$

τ being an evaporation rate of cells as mentioned by [9] and

$$\dot{R}^e = -\frac{\alpha_e}{M}P_e\Big(\frac{I_1(\alpha_e R)}{I_1(\alpha_e R_e)} - \frac{K_1(\alpha_e R)}{K_1(\alpha_e R_e)}\Big) \tag{13}$$

with $\alpha_e^2 = k_v M/\rho_e$. In Eqs.(12,13), we have applied the cancellation of cell velocity at the exterior border R_e. We have 2 unknowns: the coefficient b and P_e which are fixed by the mechanical equilibrium $P^i(R_i(t) + \delta) = P^e(R_i(t) + \delta)$ and the continuity of the flux: $\rho_i dP^i/dR = \rho_e dP^e/dR$ for $R = R_i(t) + \delta$. The principle of such analysis is simple but requires also a numerical solution that we present in Fig(6) in comparison with experimental data. However, varying parameters, the comparison with the experiment is mostly controlled by the quantity $\alpha P_i/(MR_i) = \sqrt{k_v/(\rho_0 M)}R_i^{-1}$ which is the inverse of a typical time. In the experiment the time scale is the day. it turns out that αR_i of order one is a good fitting value for the experiment so $\alpha \sim 0.7 \cdot 10^3$. Then taking the fact that experimentally 1 kPa is enough to vary the proliferation rate of 1 cell by 0.09 gives k_v/ρ of order 10^{-9} giving finally $M \sim 0.5 \cdot 10^{15}$ in SI units . A naive estimation consisting of a pico-Newton force acting on a cell of micro-size with the velocity of the layer that we estimate from Table 2 as $2 \cdot 10^{-6}$ mm/s gives the same estimation of 10^{15} in SI units. Having all the data we can estimate from Eq.(11), the departure from homeostatic pressure of 25 kPa.

4 Computational model of cell duplication and movement

To understand how the morphology of the front in the circular scratch assay depends on the interplay between cell division and mobility, we simulate a simple lattice model including mechanisms for cell division and motility, with the relative rates of the two as the tunable parameter. The model is defined on a square lattice of linear size $L = 700$, in which all the sites are occupied by cells except those inside a circle of radius $r = 320$. This choice corresponds to the ratio of cell size and the radius of the initial empty circle used in the experiments. The dynamics of the model is defined as follows: First, a random choice is made of whether a cell division (probability

P_{div} or diffusion (probability $P_{\text{diff}} = 1 - P_{\text{div}}$) attempt is made. Then, an occupied site with coordinates (x,y) is selected randomly, followed by a random selection of one of its four nearest neighbours. If that nearest neighbour site is unoccupied, a new cell is created there (cell division) or the cell at (x,y) is moved there (diffusion). If the chosen nearest neighbour site of (x,y) is occupied, nothing happens - the cell cannot move on top of another cell, nor can a new cell be created there. In any case, time is incremented with an amount proportional to $1/N$, where N is the total instantaneous number of cells present in the system. Then, a new Monte Carlo step is started by repeating the steps above. The simulation is continued until a cell reaches a small region around the center of the system. We simulate the model by varying the probability for cell division P_{div} (and thus the probability of diffusion $P_{\text{diff}} = 1 - P_{\text{div}}$) between 0 and 1. These probabilities correspond to ratios of the rates for the two processes, $k_{\text{div}}/k_{\text{diff}} = P_{\text{div}}/(1 - P_{\text{div}})$. The above protocol then corresponds to using a unit of time proportional to $1/(k_{\text{div}} + k_{\text{diff}})$, and consequently, velocities are measured in units of $k_{\text{div}} + k_{\text{diff}}$. Results are averaged over 10 realizations for each case.

In Fig. 7, we report typical configurations of the ring assay obtained by numerical simulations for different values of $k_{\text{diff}}/k_{\text{div}}$. When this ratio is large the interface is very diffuse, with several cells moving ahead of the front. As the ratio decreases, the front is more sharp, but still remains rough due to the randomness in the division process. When we compare these results with experiments, we see that fronts are more diffuse under osmotic pressure. This is consistent with the fact that $k_{\text{diff}}/k_{\text{div}}$ increases with osmotic pressure. We can estimate $k_{\text{diff}} \simeq D/a^2$, where a is the typical cell diameter. From Fig. 1, we obtain that $a \simeq 20\mu$m at 0kPa and $a \simeq 50\mu$m at 1kPa. Using our measurements for D and k_{div} [20], we obtain $k_{\text{diff}}/k_{\text{div}} \simeq 0.9$ at 0kPa and $k_{\text{diff}}/k_{\text{div}} \simeq 1.7$.

In the model, we have also quantified the front velocity and the roughness that are reported in Fig. 8. The velocity is found to decrease when diffusion predominates over cell division, suggesting that the process of ring closure is dominated by cell division (Fig. 8a). Fig. 8b shows instead that the front roughness increases when diffusion becomes more important.

5 Discussion

Melanoma is one of the most aggressive tumours and practically impossible to cure once it becomes metastatic. Hence, one of the main goals of research is to understand the processes involved in metastasis. The classical approach is to consider the biological properties of the cell trying to identify biological markers. Here, we investigated this problem from a different point of view, focusing on the possible role of mechanical stress in the selection of a more aggressive cell subpopulation. Recent research has shown the involvement of mechanical stresses, such as the osmotic pressure, in the modulation of critical biological properties [14, 11, 12, 20, 21]. Therefore, we have investigated the effect of low osmotic pressure on two cell lines belonging to the same patient, IgR39 and IgR37 a primary and metastatic cell line, respectively. Our results show that a low osmotic pressure which gives little effect on cell proliferation on the primary human melanoma cell line [20], induces significant changes on the F-actin organization,with the appearance of filopodia and stress fibres. These changes are more evident in primary human melanoma cell lines than in metastatic ones. Earlier studies on endothelial cells have shown that an osmotic pressure around 1.6KPa induces an elongation of the cells due to a rearrangement of the cytoskeleton [1, 17], in agreement with our results. In human breast cancer, mechanical compression has an effect on the contractility of the cells suggesting the presence of a mechanoregulation which is able to integrate external physics stimulation into cytoskeletal changes and therefore cell phenotypes [21].

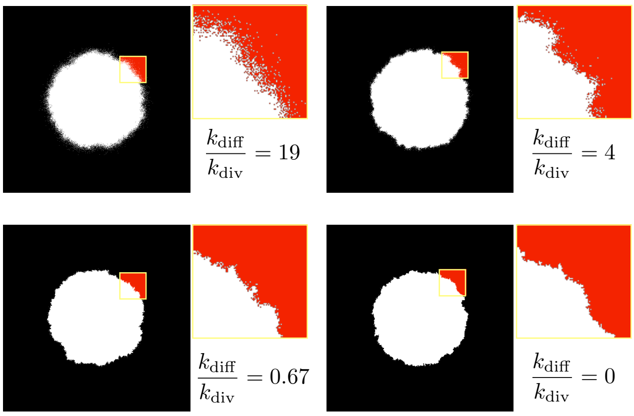

Fig. 7 Simulated ring assay. Illustrative examples of the rings obtained for different ratios of the rates of diffusion and division.

A critical question is whether F-actin rearrangement has a functional effect on biological properties of cancer cells such as their capability to move or to invade. Metastasis is indeed an integrated process composed by several steps. At least two key aspects play a critical role in this process: first the capability of the cell to move and then the capability of the cell to squeeze through the endothelium. To reproduce in vitro these two processes we have carried out the circular scratch assay which gives the possibility to study the movement of the cell into an open space and the transwell assay which investigates the capability of the cell to squeeze through a pore of a fixed size. Primary human melanoma cell are less able to move through fixed size pores using transwell assay in comparison

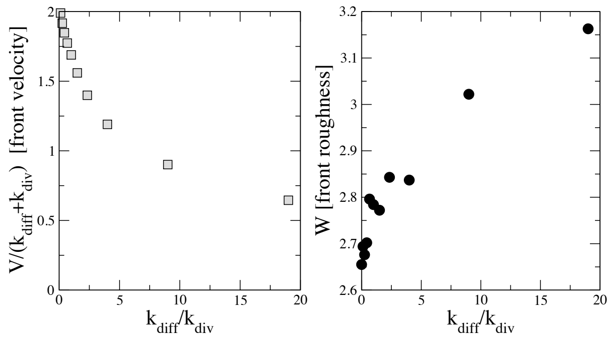

Fig. 8 Front velocity and roughness from numerical simulations. a) The front velocity as a function of the ratio of the rates of diffusion and division. b) The front roughness as a function of the ratio of the rates of diffusion and division.

to metastatic cells. Moreover, interestingly, low osmotic pressure leads to a reduced capability to transmigrate in both cell lines, however, the primary human melanoma cell line is more affected. The circular scratch assay confirms an inhibitory effect of osmotic pressure on the capability to move of the cells. This is also confirmed by quantitative measurements of cell motility from series of confocal images.

In other to better understand the biophysical aspects of the circular scratch experiments, we have approached the problem theoretically and numerically. We have derived a continuum theory for the growth of a single layer of cells with different boundary conditions such those used in the circular scratch assay. This allows to obtain quantitative predictions for the dynamics of the cell front. In particular, we calculate the dependence of the front velocity on a few experimentally measurable parameters such as the cell division rate and motility. The theoretical results are in good agreement with the experiments. The main limitation of the theoretical model is that it does not include noise and fluctuations which are obviously present in our experiments. To deal with this issue in a simple way, we introduce a discrete lattice model of cell proliferation and diffusion which we simulate in similar conditions. The discrete model allows to reproduce the experimentally observed roughening of the cell front.

This combination of theoretical and numerical models allows to understand better the role of motility and cell division under osmotic pressure and provide a useful tool to explore the effect of experimentally relevant parameter. Experimentally, fronts appear to be more diffusive under osmotic pressure and this is explained by our model when we input into it parameters measured from other independent experiments. Both cell proliferation and motility rates are reduced by osmotic pressure, which also changes the shape of cells making them thinner and more elongated. The combination of this factor leads to an increase of $k_{\text{diff}}/k_{\text{div}}$ under osmotic pressure.

All together our results show how low osmotic pressure changes functional properties of the tumour cells leading to the selection of subpopulation that appear more aggressive. These results appear in agreement with previous papers showing a role of osmotic pressure in the selection of more resistant subpopulation [6, 14, 16].

6 Material and Methods

6.1 Dextran solution

A master solution of dextran at 10% (w/v) was formed (Dextran from Leuconostoc spp, Fluka) and diluted to the desired concentration with complete medium. Transformation from dextran concentration to osmotic pressure was performed according to the calibration curve measured in Ref. [5].

6.2 Cell lines

Human IGR39 and IGR37 cells were obtained from Deutsche Sammlung von Mikroorganismen und Zellkulturen GmbH and cultured as previously described [19]. IGR39 was derived from a primary amelanotic cutaneous tumour and IGR37 from an inguinal lymph node metastasis in the same patient. The cells were plated on pre-coated collagen type I plates according to the manufacturer's instructions for further experiments when specified in the results section.

6.3 Cell transfection

Cells were transfected with 1μg H2B-GFP plasmide (plasmide 116980, Addgene) according to the manufactories instruction of SuperFect Transfection reagent by Qiagen. The cells were analyzed by time lapse using Leica TCS SP5 AOBS with resonant scanner, equipped with a 20X, 0.5 NA, dry objective (Leica Microsystems GmbH, Wetzlar Germany) with fluorescence under 5% CO2 and 37C temperature.

6.4 Immunofluorescence-Phalloidin

Subconfluent cells grown on glass coverslip were fixed with 3.7% parafolmaldeide in PBS for 10min, permealized with 0.5% Triton X-100 in PBS for 5min at room temperature and. stained with 200μl of 100nM Acti-stain™ 555 Phalloidin (TebuBio, Cat. # PHDH1) for 30min. DNA was counterstained for 30s with 200μl of 100nM DAPI and the slides were mounted with Pro-long anti fade reagent (Invitrogen). The images were acquired using a Leika TCS NT confocal microscope.The same experiments were carried out using pretreated collagen type I coverslips (Sigma).

6.5 Immunohystochemistry-Ki67

Cells plated for ring assay were fixed with 3.7%paraformaldeide for 10min at room temperature, incubated for 1hr in 1%BSA, 10NGS, 0.3M glycin, 0.1%Tween in PBS and overnight with anti-Ki67 (clone MIB-1, Dako, 1:100 cod.) at 4C. All the sections were incubated for 30min with biotinylated anti-mouse secondary antibody in PBS (Dako, 1:100). This was followed by incubation with streptavidin (Dako, 1:350) coniugated to peroxidase in PBS for 30min, and by a brief rinse in PBS. Color was routinely developed using DAB peroxidase substrate kit (Vector) up to 10 min, rinsed in distilled water, and coverslipped with a permanent mounting medium. The images were acquired using a microscope Leica MZ FLIII mounted with a camera Leica DFC320.

6.6 Circular scratch assay

Cells were plated on 33cm^2 Petri dish with a ring at the center each (Sigma cod. z370789, diameter: 6.4mm, area 32mm^2) to reach 70-80% confluence as a monolayer. When they were at confluence, the ring was removed and the cells were fixed with 3.7% paraformaldeide at different times (from 4 to 96hrs) and stained with hematoxillin-eosin. The images were acquired using a Leica MZFL11 microscope mounted with a Camera Leica DFC 32 at different magnification (8, 16 and 25X). To quantify the free area and the correspondent percentage of covered area calculated we used Gimp (GNU Image Manipulation Program).

6.7 Transwell migration assay

Migration experiments were conducted using a conventional 24-well Transwell system (6.5 mm TranswellH (# 3422), CorningH, NY, USA) with each well separated by a microporous polycarbonate membrane (10 mm thickness, 8 mm pores) into an upper (insert) and a lower chamber (well) according to [16]. After 24 hours of serum deprivation, cells were detached, counted and resuspended in growth media without FBS to obtain equal cell densities (296000 cells/cm^2). A volume of 250 μl containing 70000 cells was plated to each insert and 600 μl medium was added to the wells. As chemotactic factors, a medium containing 10% FBS was used. After 6 hours the cells were fixed and stained in a 20% methanol/0.1% crystal violet solution for three minutes at room temperature, followed by washing in deionized water to remove redundant staining [16]. Non-migrated cells remaining at the upper side of the membranes were carefully removed with cotton swabs and inserts were dried in darkness overnight. The following day at stained membranes were made pictures using a transmitted-light microscope (Leica MZFL11 microscope mounted with a camera Leica DFC 32) at different magnification (8, 16 and 25X). The blue cells were counted using the magnified images (25X) and then calculated for the whole surface (32cm^2).

6.8 Cell tracking

Cell tracking has been done in ImageJ by first projecting the confocal stacks (maximum intensity) and then finding the maxima for different frames.

6.9 Statistical analysis

Statistical significance was evaluated using the Kolomogorov-Smirnov non parametric test (see http://www.physics.csbsju.edu/stats/KS-test.html).

7 Acknowledgments

This work is supported in part by AAP Physique and Cancer 2012, project DERMA (MBA). SZ acknowledges the visiting professor programme of UPMC and the European Research Council Advanced grant SIZEFFECTS. CAMLP and SZ acknowledge the visiting professor programme of Aalto University. CAMLP is supported by PRIN 2010. LL and MJA are supported by the Academy of Finland through an Academy Research Fellowship (LL., Project No. 268302) and through the Centres of Excellence Program (MJA and L. L., Project No. 251748).

References

1 Acevedo, A. D., Bowser, S. S., Gerritsen, M. E. & Bizios, R. 1993 Morphological and proliferative responses of endothelial cells to hydrostatic pressure: role of fibroblast

growth factor. *J Cell Physiol*, **157**(3), 603–14. (doi:10.1002/jcp.1041570321)

2 Ben Amar, M. 2013 Chemotaxis migration and morphogenesis of living colonies. *Eur Phys J E Soft Matter*, **36**(6), 64. (doi:10.1140/epje/i2013-13064-5)

3 Ben Amar, M. & Wu, M. 2014 Re-epithelialization: advancing epithelium frontier during wound healing. *J R Soc Interface*, **11**(93), 20131 038. (doi:10.1098/rsif.2013.1038)

4 Bernard, C. 1865 *Introduction à l' étude de la médecine expérimentale*. Paris.

5 Bonnet-Gonnet, C., Belloni, L. & Cabane, B. 1994 Osmotic pressure of latex dispersions. *Langmuir*, **10**(11), 4012–4021. (doi:10.1021/la00023a019)

6 Boucher, Y., Kirkwood, J. M., Opacic, D., Desantis, M. & Jain, R. K. 1991 Interstitial hypertension in superficial metastatic melanomas in humans. *Cancer Res*, **51**(24), 6691–4.

7 Bounedjah, O., Hamon, L., Savarin, P., Desforges, B., Curmi, P. A. & Pastré, D. 2012 Macromolecular crowding regulates assembly of mrna stress granules after osmotic stress: new role for compatible osmolytes. *J Biol Chem*, **287**(4), 2446–58. (doi:10.1074/jbc.M111.292748)

8 Callan-Jones, A. C., Joanny, J.-F. & Prost, J. 2008 Viscous-fingering-like instability of cell fragments. *Phys Rev Lett*, **100**(25), 258 106.

9 Eisenhoffer, G. T., Loftus, P. D., Yoshigi, M., Otsuna, H., Chien, C.-B., Morcos, P. A. & Rosenblatt, J. 2012 Crowding induces live cell extrusion to maintain homeostatic cell numbers in epithelia. *Nature*, **484**(7395), 546–9. (doi:10.1038/nature10999)

10 Ignatova, Z. & Gierasch, L. M. 2006 Inhibition of protein aggregation in vitro and in vivo by a natural osmoprotectant. *Proc Natl Acad Sci U S A*, **103**(36), 13 357–61. (doi:10.1073/pnas.0603772103)

11 Montel, F., Delarue, M., Elgeti, J., Malaquin, L., Basan, M., Risler, T., Cabane, B., Vignjevic, D., Prost, J. *et al.* 2011 Stress clamp experiments on multicellular tumor spheroids. *Phys. Rev. Lett.*, **107**, 188 102. (doi:10.1103/PhysRevLett.107.188102)

12 Montel, F., Delarue, M., Elgeti, J., Vignjevic, D., Cappello, G. & Prost, J. 2012 Isotropic stress reduces cell proliferation in tumor spheroids. *New Journal of Physics*, **14**(5), 055 008.

13 Nielsen, M.-B., Christensen, S. T. & Hoffmann, E. K. 2008 Effects of osmotic stress on the activity of mapks and pdgfr-beta-mediated signal transduction in nih-3t3 fibroblasts. *Am J Physiol Cell Physiol*, **294**(4), C1046–55. (doi:10.1152/ajpcell.00134.2007)

14 Paszek, M. J., Zahir, N., Johnson, K. R., Lakins, J. N., Rozenberg, G. I., Gefen, A., Reinhart-King, C. A., Margulies, S. S., Dembo, M. *et al.* 2005 Tensional homeostasis and the malignant phenotype. *Cancer Cell*, **8**(3), 241–54. (doi:10.1016/j.ccr.2005.08.010)

15 Racz, B., Reglodi, D., Fodor, B., Gasz, B., Lubics, A., Gallyas, Jr, F., Roth, E. & Borsiczky, B. 2007 Hyperosmotic stress-induced apoptotic signaling pathways in chondrocytes. *Bone*, **40**(6), 1536–43. (doi:10.1016/j.bone.2007.02.011)

16 Rofstad, E. K., Tunheim, S. H., Mathiesen, B., Graff, B. A., Halsør, E. F., Nilsen, K. & Galappathi, K. 2002 Pulmonary and lymph node metastasis is associated with primary tumor interstitial fluid pressure in human melanoma xenografts. *Cancer Res*, **62**(3), 661–4.

17 Salwen, S. A., Szarowski, D. H., Turner, J. N. & Bizios, R. 1998 Three-dimensional changes of the cytoskeleton of vascular endothelial cells exposed to sustained hydrostatic pressure. *Med Biol Eng Comput*, **36**(4), 520–7.

18 Simonsen, T. G., Gaustad, J.-V., Leinaas, M. N. & Rofstad, E. K. 2012 High interstitial fluid pressure is associated with tumor-line specific vascular abnormalities in human melanoma xenografts. *PLoS One*, **7**(6), e40 006. (doi:10.1371/journal.pone.0040006)

19 Taghizadeh, R., Noh, M., Huh, Y. H., Ciusani, E., Sigalotti, L., Maio, M., Arosio, B., Nicotra, M. R., Natali, P. *et al.* 2010 CXCR6, a newly defined biomarker of tissue-specific stem cell asymmetric self-renewal, identifies more aggressive human melanoma cancer stem cells. *PLoS One*, **5**(12), e15 183. (doi:10.1371/journal.pone.0015183)

20 Taloni, A., Alemi, A. A., Ciusani, E., Sethna, J. P., Zapperi, S. & La Porta, C. A. M. 2014 Mechanical properties of growing melanocytic nevi and the progression to melanoma. *PLoS One*, **9**(4), e94 229. (doi:10.1371/journal.pone.0094229)

21 Tse, J. M., Cheng, G., Tyrrell, J. A., Wilcox-Adelman, S. A., Boucher, Y., Jain, R. K. & Munn, L. L. 2012 Mechanical compression drives cancer cells toward invasive phenotype. *Proc Natl Acad Sci U S A*, **109**(3), 911–6. (doi:10.1073/pnas.1118910109)

22 Wu, M., Frieboes, H. B., McDougall, S. R., Chaplain, M. A. J., Cristini, V. & Lowengrub, J. 2013 The effect of interstitial pressure on tumor growth: coupling with the blood and lymphatic vascular systems. *J Theor Biol*, **320**, 131–51. (doi:10.1016/j.jtbi.2012.11.031)

NEOPLASIA
www.neoplasia.com

Volume 14 Number 12 December 2012 pp. 1236–1248 1236

Regeneration-associated WNT Signaling Is Activated in Long-term Reconstituting AC133$^{\text{bright}}$ Acute Myeloid Leukemia Cells[1,2]

Alessandro Beghini[*], Francesca Corlazzoli[*,3], Luca Del Giacco[†,3], Matteo Re[‡], Francesca Lazzaroni[*], Matteo Brioschi[§], Giorgio Valentini[‡], Fulvia Ferrazzi[¶,#], Anna Ghilardi[†], Marco Righi[*,], Mauro Turrini[††], Marco Mignardi[‡‡,§§], Clara Cesana[††], Vincenzo Bronte[¶¶], Mats Nilsson[‡‡,§§], Enrica Morra[††] and Roberto Cairoli[††,##]**

*Department of Medical Biotechnology and Translational Medicine, Università degli Studi di Milano, Milano, Italy; †Department of Biosciences, Università degli Studi di Milano, Milano, Italy; ‡Department of Computer Science, Università degli Studi di Milano, Milano, Italy; §Dipartimento di Scienze Oncologiche e Chirurgiche, Università degli Studi di Padova, Padova, Italy; ¶Dipartimento di Informatica e Sistemistica, Università degli Studi di Pavia, Pavia, Italy; #Gene Center, Ludwig-Maximilians-Universität München, Munich, Germany; **Consiglio Nazionale delle Ricerche, Institute of Neuroscience, Milano, Italy; ††Department of Oncology, Niguarda Hospital, Milano, Italy; ‡‡Department of Immunology, Genetics and Pathology, Rudbeck Laboratory, Uppsala Universitet, Uppsala, Sweden; §§Science for Life Laboratory, Department of Biochemistry and Biophysics, Stockholm University, Solna, Sweden; ¶¶Istituto Oncologico Veneto, Padova, Italy; ##Divisione di Medicina Interna, Sezione di Ematologia Clinica, Ospedale Valduce, Como, Italy

Abstract

Acute myeloid leukemia (AML) is a genetically heterogeneous clonal disorder characterized by two molecularly distinct self-renewing leukemic stem cell (LSC) populations most closely related to normal progenitors and organized as a hierarchy. A requirement for WNT/β-catenin signaling in the pathogenesis of AML has recently been suggested by a mouse model. However, its relationship to a specific molecular function promoting retention of self-renewing leukemia-initiating cells (LICs) in human remains elusive. To identify transcriptional programs involved in the maintenance of a self-renewing state in LICs, we performed the expression profiling in normal ($n = 10$) and leukemic ($n = 33$) human long-term reconstituting AC133^{+} cells, which represent an expanded cell population in most AML patients. This study reveals the ligand-dependent WNT pathway activation in AC133$^{\text{bright}}$ AML cells and shows a diffuse

Abbreviations: AML, acute myeloid leukemia; LSC, leukemic stem cell; LT-HSCs, long-term hematopoietic stem cells; CFU, colony forming units; CFU-GM, granulocyte/macrophage; BM MNCs, bone marrow mononuclear cells; LIC, leukemia-initiating cell

Address all correspondence to: Alessandro Beghini, PhD, Department of Medical Biotechnology and Translational Medicine, Università degli Studi di Milano, via Viotti 3/5, 20133 Milano, Italy. E-mail: alessandro.beghini@unimi.it

[1] This work was supported in part by PUR 2008 (to A.B.), Progetto Integrato Oncologia 2006 (RO 4/2007), Associazione Malattie del Sangue Onlus (AMS), and Piano Regionale Sangue-Regione Lombardia 2006 (DDG 7917). The authors declare that they have no competing financial interests.

[2] This article refers to supplementary materials, which are designated by Table W1 and W2 and Figure W1 and are available online at www.neoplasia.com.

[3] F. Corlazzoli and L. Del Giacco contributed equally to this work.

Received 7 September 2012; Revised 15 October 2012; Accepted 18 October 2012

DOI 10.1593/neo.121480

expression and release of WNT10B, a hematopoietic stem cell regenerative-associated molecule. The establishment of a primary AC133$^+$ AML cell culture (A46) demonstrated that leukemia cells synthesize and secrete WNT ligands, increasing the levels of dephosphorylated β-catenin *in vivo*. We tested the LSC functional activity in AC133$^+$ cells and found significant levels of engraftment upon transplantation of A46 cells into irradiated Rag2$^{-/-}$γc$^{-/-}$ mice. Owing to the link between hematopoietic regeneration and developmental signaling, we transplanted A46 cells into developing zebrafish. This system revealed the formation of ectopic structures by activating dorsal organizer markers that act downstream of the WNT pathway. In conclusion, our findings suggest that AC133$^{\text{bright}}$ LSCs are promoted by misappropriating homeostatic WNT programs that control hematopoietic regeneration.

Neoplasia (2012) 14, 1236–1248

Introduction

Different genetic causes result in variable clinical courses of acute myeloid leukemia (AML) and different responses to standard chemotherapy including stem cell transplant. Despite the genetic differences among individual patients, most AML clones display certain common features. Ample evidence exists in mouse models that AML develops through the stepwise acquisition of collaborating genetic and epigenetic changes in self-renewing LICs, which exhibit a committed myeloid immunophenotype and give rise to nonleukemogenic progeny in a myeloid-restricted hierarchy [1–3]. An important issue to understand the early events in the origin of AML is the observation that long-term hematopoietic stem cell (LT-HSC) expansion precedes the generation of committed myeloid LICs [4].

Although well-orchestrated cell intrinsic programs and environmental cues represent the main contributory factors for normal LT-HSC expansion, it is still unclear if transcriptional programs responsible for the expansion of premalignant LT-HSC populations and leukemia initiation share common embryonic or post-embryonic functions, such as stem cell renewal, tissue repair, and regeneration [5,6]. Even though recent studies have addressed the role of Hedgehog signaling for maintenance of cancer stem cells in myeloid leukemia [7], its requirement in AML remains controversial [8].

Recently, the notion that LICs are restricted only to the CD34$^+$CD38$^-$ population has been challenged [9,10] and it has been suggested that more cell surface markers could be appropriately used to enrich the leukemia-initiating cell (LIC)–containing fraction. One of such markers is the AC133 antigen (a glycosylation-dependent epitope of CD133) that defines a desirable population of stem and progenitor cells containing in turn all the CD34$^{\text{bright}}$CD38$^-$ progenitors, as well as the CD34$^{\text{bright}}$CD38$^+$ cells committed to the granulocytic/monocytic lineage [11]. In addition, AC133 represents a well-documented marker of tumor-initiating cells in a number of human cancers [12]. In this study, fluorescence-activated cell sorter (FACS) analysis demonstrates that AC133$^+$ cell population is dramatically expanded in 25 AML cases analyzed. We carried out genome-wide transcriptional analysis of AC133$^+$ cells isolated from newly diagnosed non-promyelocytic AML patients ($n = 33$) and healthy donors ($n = 10$). Results obtained from a multistep analysis of the generated data defined the involvement of the ligand-dependent WNT receptor signaling pathway as the self-renewal associated signature in the AC133-enriched fraction in human AML. Furthermore, the results presented here suggested that *WNT10B* and other WNT genes expressed during the regenerative process of the hematopoietic system [13,14] are aberrantly upregulated in AC133$^{\text{bright}}$ AML cells. To obtain a localized detection of each single transcript, we first applied an *in situ* detection of individual mRNA molecules [15] on bone marrow (BM) sections from AML patients. By the establishment of a primary culture of AC133$^+$ AML cells (termed A46 hereafter), we confirmed that secreted WNTs activated a β-catenin/human T-cell factor (TCF) transcription–based reporter construct. Moreover, we intend to clarify the relationship between the abnormal WNT activation in AC133$^+$ population and the leukemic stem cell (LSC) activity. Using Rag2$^{-/-}$γc$^{-/-}$ as immunodeficient xenotransplant model [16], AC133$^+$ A46 cells were injected intravenously into sublethally irradiated mice.

To achieve a complete view of how AC133$^+$ A46 cells modulated the microenvironment and given that hematopoietic regeneration converge to developmental signaling, we used zebrafish embryonic model as an *in vivo* biosensor.

Our results confirmed previously reported data [17] and raise new important implications for the involvement of the ligand-dependent canonical WNT pathway in AML. These suggestive findings are supported by the pivotal function of WNT in promoting self-renewal [18,19], its emerging role in myeloid leukemogenesis [20,21], and the effects of its constitutive activation through a stabilized form of β-catenin, by inducing quiescent stem cells to enter the cell cycle and arresting their differentiation [22,23].

Materials and Methods

Collection of Patient Samples and Normal Hematopoietic Cells

BM MNCs were collected from 33 newly diagnosed, unselected non-promyelocytic AML patients, according to Niguarda Hospital's Ethical Board–approved protocols (116_04/2010). According to the revised Medical Research Council risk group stratification, based on cytogenetic and molecular markers/mutations [24], samples included 14 adverse, 13 intermediate, and 6 favorable risk patients. Human adult BM cells obtained from 10 consenting healthy donors were processed as previously described [25].

Cell Sorting and Flow Cytometry

We carried out AC133$^+$ cell separation based on MACS MicroBeads and cytofluorometric determinations, as previously described [25].

Microarray Expression Analysis

Total RNA for expression profiling was extracted using RNAqueous-4PCR kit (Ambion, Austin, TX) from AC133-selected cells. Expression profiling was performed on Affymetrix HGU133plus2.0 GeneChip arrays according to the manufacturer's procedures. The bioinformatics analysis performed in this study was realized using the R language for statistical computing (http://www.r-project.org/) and the annotation libraries provided by the Bioconductor project (http://www.bioconductor.org/). Microarray data have been deposited in ArrayExpress (http://www.ebi.ac.uk/arrayexpress/), with accession number E-MTAB-220. We performed a genome-wide analysis to select genes differentially expressed between AML AC133$^+$ patients and AC133$^+$ healthy donors (Welch t test, 0.05 significance level). The resulting set of differentially expressed genes has been analyzed for functional enrichment with respect to the terms of the Biological Process (BP) branch of the Gene Ontology (GO) and the pathways of the KEGG database. We relied on three different methods for functional enrichment analysis: GOStats (version 2.12.0 of the Bioconductor package, http://www.bioconductor.org/packages/release/bioc/html/GOstats.html) [26], Database for Annotation, Visualization and Integrated Discovery (DAVID; http://david.abcc.ncifcrf.gov/home.jsp) [27], and the iterative procedure of dysregulated pathway analysis proposed by Majeti et al. [17]. The first two tests are based on the hypergeometric distribution, whereas the last one is based on a non-parametric test and on an iterative procedure. Overrepresented GO terms and KEGG pathways have been selected at 0.05 significance level.

WNT/β-catenin Responsive Luciferase Assay

HEK293T cells grown in 24-well plates at a density of 1.7×10^5 cells per well were transfected with M50 Super 8x TOPFlash (plasmid 12456; Addgene, Cambridge, MA) and pRL-TK (Renilla luciferase; Promega, Madison, WI) using jetPEI (Polyplus, New York, NY). Cells were treated for 12 hours with A46 conditioned medium (CM) or HEK293T cells transfected with BA-*WNT10B* (plasmid 1831; Addgene) CM as positive control. *WNT10B* expression in HEK293T transfected with BA-WNT10B was evaluated by SYBR Green–based real-time reverse transcription–polymerase chain reaction (RT-PCR) using *WNT10B* FW-5′-GCTGTAACCATGACATGGAC-3′ and RW-5′-CTGCCTGATGTGCCATGAC-3′ specific primers. Luciferase activity measurement was performed with the Dual-Luciferase Reporter Assay System (Promega).

Immunoblot

Protein expression was assessed by immunoblot analysis using standard procedures, applying anti–active β-catenin (ABC) monoclonal mouse (anti-ABC clone 8E7; Millipore, Billerica, MA), anti–β-catenin monoclonal rabbit (E247; Abcam, Cambridge, United Kingdom), anti–WNT10B polyclonal rabbit (H-70; Santa Cruz Biotechnology, Inc, Santa Cruz, CA), anti–WNT10B monoclonal mouse (5A7; Abcam), anti–glyceraldehyde-3-phosphate dehydrogenase (GAPDH) polyclonal rabbit (ab97626; Abcam), and anti–Pygopus 2 polyclonal rabbit (H-216; Santa Cruz Biotechnology, Inc) antibodies. Secondary antibodies used were anti–mouse HRP, anti–goat HRP, and anti–rabbit HRP (Thermo Fisher Scientific, Waltham, MA).

In Situ *mRNA Detection*

In situ detection of individual mRNA molecules was performed as described [15]. One micromolar of locked nucleic acid–modified cDNA primer (*WNT10B*, 5′-C+A+G+G+C+CGGACAGCGTCAAGCACACG-3′; *β-actin*, 5′-C+TG+AC+CC+AT+GCCCACCATCACGCCC-3′; Exiqon, Vedbaek, Denmark) was added to the reverse transcriptase reaction. Ligation was then carried out with 0.1 μM of the *WNT10B* padlock probe or *β-actin* padlock probe (*WNT10B*, 5′-[Phos]ACCGTGCCTGTCGGACCCTCCTCTATGATTACTGACCTAAGTCGGAAGTACTACTCTCTTCTTCTTTTAGTGAAGCCCAGGCAACCCA-3′; *β-actin*, 5′-[Phos]GCCGGCTTCGCGGGCGACGATTCCTCTATGATTACTGACCTATGCGTCTATTTAGTGGAGCCTCTTCTTTACGGCGCCGGCATGTGCAAG-3′; Sigma-Aldrich, St Louis, MO). Rolling circle products (RCPs) were visualized using 100 nM of detection probe (*WNT10B*, 5′-Cy5-AGTCGGAAGTACTACTCTCT-3′ and *β-actin*, 5′-Cy3-TGCGTCTATTTAGTGGAGCC-3′; Sigma-Aldrich). Nuclei were counterstained with 100 ng/ml Hoechst 33258 (Sigma-Aldrich). Images of BM tissue slides were acquired using an Axioplan II epifluorescence microscope (Zeiss, Munchen, Germany) equipped with a charge-coupled device (CCD) camera (HRM, Zeiss) and a computer-controlled filter wheel with excitation and emission filters for visualization of 4′-6-diamidino-2-phenylindole (DAPI), Cy3, and Cy5. A ×20 objective (Plan-Apocromat, Zeiss) was used for capturing the images. Images were collected using the Axiovision software (release 4.3, Zeiss). Images were collected as *z*-stacks to ensure that all RCPs were imaged, with a maximum intensity project created in Axiovision. For quantification, the numbers of RCPs and cell nuclei in images were counted digitally using CellProfiler software (www.cellprofiler.org) on three ×20 microscope images. The total number of RCPs was divided by the number of nuclei for each image. The average for each sample was then calculated from the result of the three images and is reported as RCPs per cell.

Immunostaining

Direct and indirect immunostaining were performed following standard procedures. BM biopsies of AML patients, previously embedded in paraffin blocks, were cut in 5-μm-thick sections and mounted on slides. Slides were incubated with primary antibody mouse anti-CD133.1 (AC133) (1:100; Miltenyi Biotec GmBH, Bergisch Gladbach, Germany), directly labeled with 488-nm dye (Sigma), and with primary antibodies such as mouse anti-ABC (1:100; Millipore), rabbit anti-WNT10B (H70) (1:100; Santa Cruz Biotechnology, Inc), rabbit anti–Pygopus 2 (H-216) (1:100; Santa Cruz Biotechnology, Inc), goat anti-SMYD3 (F-19) (1:100; Santa Cruz Biotechnology, Inc). Samples were incubated with the secondary antibodies donkey anti-mouse Alexa Fluor 488 (1:500; Life Technologies, Carlsband, CA), donkey anti-rabbit Alexa Fluor 568 (1:500; Life Technologies), and donkey anti-goat Alexa Fluor 568 (1:500; Life technologies). Nuclei were counterstained with 100 ng/ml DAPI (Sigma-Aldrich). Cells were analyzed using the upright microscope (Leica, DM 4000B).

Immunofluorescence Image Analysis

Image analysis was performed by means of a custom automatic routine and the ImageJ program (1.43s; National Institutes of Health, Bethesda, MD). Maps of ABC$^+$/WNT10B$^+$ cells were obtained using an automatic threshold based on moments algorithm newly implemented in the ImageJ program and mathematical morphology plugin developed by D. Prodanov (http://rsbweb.nih.gov/ij/plugins/gray-morphology.html). DAPI staining was used to identify nuclei. Finally, images of nuclei for positive cells were obtained by Boolean AND operations between DAPI staining and cell maps. The resulting images were used to determine the percentage of ABC$^+$/WNT10B$^+$ cells both manually or through the Analyze Particles function of ImageJ.

Cell Culture

Selected AC133$^+$ cells from BM at AML diagnosis were cultured for 16 weeks. The culture was performed using synthetic medium

StemSpam H3000 (StemCell Technologies, Vancouver, Canada) in the absence of serum and cytokines. StemSpan H3000 and HPGM media, conditioned by the cell culture, were collected after 12 weeks, refined with 0.2-μm filter and stored at −20°C. HEK293T cells were grown in Dulbecco's modified Eagle's medium (high glucose with sodium pyruvate and L-glutamine; Euroclone), supplemented with 10% FBS (Euroclone) and penicillin-streptomycin solution (100×) (Euroclone, Milano, Italy).

Mice and Xenogeneic Transplantation

Rag2$^{-/-}\gamma c^{-/-}$ BALB/c mice were bred and maintained under specific pathogen-free conditions in the mouse facility of Istituto Oncologico Veneto, and experiments were performed according to state guidelines and approved by the local ethics committee. Rag2$^{-/-}\gamma c^{-/-}$ mice at 6 weeks were sublethally irradiated with 5 Gy and transplanted via the tail vein with 1 × 10^6 of human AC133$^+$ AML cells (A46).

Evaluation of Hematopoietic Chimerism by Flow Cytometry

Three weeks after transplantation, recipient mice were sacrificed and BM cells were harvested by flushing femurs and tibias. BM engraftment was evaluated using human antibodies CD34, CD38, AC133, and CD45 [BD Biosciences (Bedford, MA) and Miltenyi Biotec GmBH]. Multicolor flow cytometric analyses were performed using FACSCalibur flow cytometer (BD Biosciences) and analyzed by FlowJo software (Tree Star, Ashland, OR). Cell engraftment was determined by expression of the human panleukocyte marker CD45.

Zebrafish Models and Transplantation Procedures

Embryos were handled according to relevant guidelines. Fish of the AB strain were maintained at 28°C on a 14-hour light/10-hour dark cycle and collected by natural spawning. Transplantation of human A46 cells into zebrafish embryos was performed as previously reported [28]. Briefly, fluorescently labeled A46 cells were resuspended in 1× phosphate-buffered saline and injected into zebrafish blastulae (between 100 and 200 cells per injection) at 3 hours post-fertilization (hpf). Injected live embryos were observed under a fluorescent microscope at 30% of epiboly to ensure the presence of labeled A46 cells. Embryos were collected at the desired developmental stages, immediately fixed, and processed for whole-mount *in situ* hybridization according to Thisse et al. [29], using *gsc*, *ntl*, and *pax2a* DIG-labeled riboprobes.

Results

AC133$^+$ Cells Are Highly Expanded in AML

AC133 antigen is restricted to a rare cell population with long-term reconstituting activity, ranging from 20% to 60% of all CD34$^+$ cells, and resulting barely detectable in CD34$^-$Lin$^-$ cells [11–30]. We have previously shown that AC133$^+$ LT-HSCs are also highly enriched in colony forming units and have a stronger granulocyte/macrophage differentiation potential relative to unselected BM MNCs. However, their burst-forming units–erythroid forming potential is lower [25]. To determine the range of expansion of AC133$^+$ cell fraction in AML, flow cytometric quantification of CD133.1 (AC133) expression either in single staining or in combination with the pan-hematopoietic marker CD45 was performed in BM on 25 primary non-promyelocytic AML samples and 10 age-matched healthy volunteer adult donors. The resulting CD133.1$^+$ cell fraction results expanded among AML patients by a median of 31.5% [interquartile range (IQR), 16.5%–53.4%] with respect to normal donors (median, 0.54%; IQR, 0.17%–1.14%; $P < .0001$; Figure 1, *A–C*). To directly compare the gene expression profiles of purified populations highly enriched in LSCs or HSCs, positive selection of CD133.1$^+$ cells was performed on all the 33 non-promyelocytic AML patients (25 *de novo*, 7 secondary to myelodysplasia, and 1 secondary therapy-related; Table W1) as well as on the 10 healthy donors recruited to this study, respectively. MNC selection in samples from AML patients led to an average of 236-fold enrichment of AC133-positive cells (IQR, 142.72–419.44, data not shown).

Identification of Dysregulated Pathways in AC133$^+$ AML Cell Fraction

To identify the dysregulated pathways in AC133$^+$ AML cell fraction *versus* normal long-term reconstituting AC133$^+$ HSC cells, we performed a genome-wide functional enrichment analysis on gene expression microarray data of 33 AML patients and 10 healthy donors. The identification of overrepresented pathways in AC133$^+$ AML cells was realized through three computational tools: GOStats [26], DAVID [27], and dysregulated pathway analysis according to Majeti et al. [17]. Employing the functional terms from GO BPs and the pathway information from KEGG databases, we found 212 functionally enriched GO BP terms with GOStats ($P < .01$), 284 GO BP terms with DAVID ($P < .05$), and 616 GO BP terms with the non-parametric test of Majeti et al. ($P < .05$). Moreover, GOStats selected 16 KEGG pathways

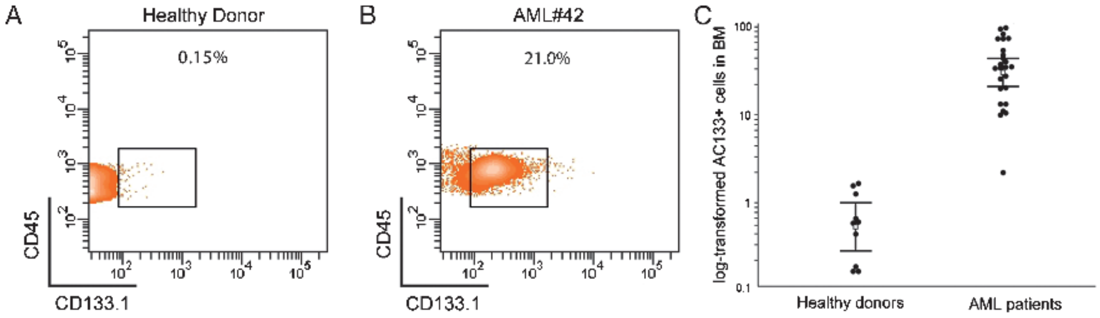

Figure 1. Human AC133$^+$ cells are strongly expanded in AML. Representative dot plots of the immunophenotype analysis from the BM of (A) a healthy donor and (B) a patient with AML (AML No. 42 in Table W1). The CD45/CD133.1 co-staining was gated on BM MNCs; percentages on total cellularity are shown for gated normal and AML populations. (C) Flow cytometry analysis of the CD133.1 antigen in BM MNCs of healthy donors ($n = 10$) and AML patients ($n = 25$). The IQR for each sample group is indicated in the dot. Mann-Whitney U test was used to calculate the P value ($\alpha = 0.001$).

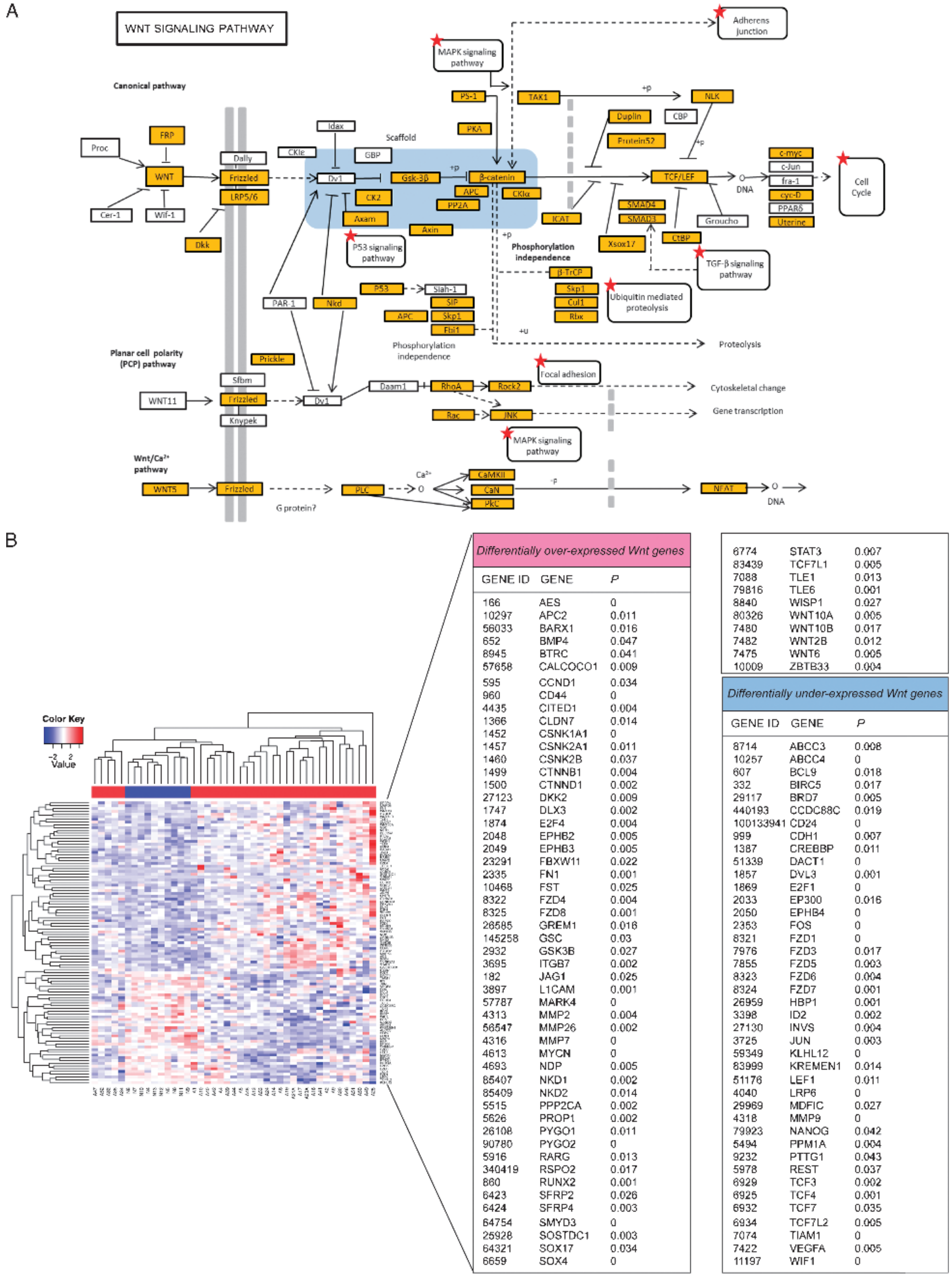

Differentially over-expressed Wnt genes		
GENE ID	GENE	*P*
166	AES	0
10297	APC2	0.011
56033	BARX1	0.016
652	BMP4	0.047
8945	BTRC	0.041
57658	CALCOCO1	0.009
595	CCND1	0.034
960	CD44	0
4435	CITED1	0.004
1366	CLDN7	0.014
1452	CSNK1A1	0
1457	CSNK2A1	0.011
1460	CSNK2B	0.037
1499	CTNNB1	0.004
1500	CTNND1	0.002
27123	DKK2	0.009
1747	DLX3	0.002
1874	E2F4	0.004
2048	EPHB2	0.005
2049	EPHB3	0.005
23291	FBXW11	0.022
2335	FN1	0.001
10468	FST	0.025
8322	FZD4	0.004
8325	FZD8	0.001
26585	GREM1	0.016
145258	GSC	0.03
2932	GSK3B	0.027
3695	ITGB7	0.002
182	JAG1	0.025
3897	L1CAM	0.001
57787	MARK4	0
4313	MMP2	0.004
56547	MMP26	0.002
4316	MMP7	0
4613	MYCN	0
4693	NDP	0.005
85407	NKD1	0.002
85409	NKD2	0.014
5515	PPP2CA	0.002
5626	PROP1	0.002
26108	PYGO1	0.011
90780	PYGO2	0
5916	RARG	0.013
340419	RSPO2	0.017
860	RUNX2	0.001
6423	SFRP2	0.026
6424	SFRP4	0.003
64754	SMYD3	0
25928	SOSTDC1	0.003
64321	SOX17	0.034
6659	SOX4	0
6774	STAT3	0.007
83439	TCF7L1	0.005
7088	TLE1	0.013
79816	TLE6	0.001
8840	WISP1	0.027
80326	WNT10A	0.005
7480	WNT10B	0.017
7482	WNT2B	0.012
7475	WNT6	0.005
10009	ZBTB33	0.004

Differentially under-expressed Wnt genes		
GENE ID	GENE	*P*
8714	ABCC3	0.008
10257	ABCC4	0
607	BCL9	0.018
332	BIRC5	0.017
29117	BRD7	0.005
440193	CCDC88C	0.019
100133941	CD24	0
999	CDH1	0.007
1387	CREBBP	0.011
51339	DACT1	0
1857	DVL3	0.001
1869	E2F1	0
2033	EP300	0.016
2050	EPHB4	0
2353	FOS	0
8321	FZD1	0
7976	FZD3	0.017
7855	FZD5	0.003
8323	FZD6	0.004
8324	FZD7	0.001
26959	HBP1	0.001
3398	ID2	0.002
27130	INVS	0.004
3725	JUN	0.003
59349	KLHL12	0
83999	KREMEN1	0.014
51176	LEF1	0.011
4040	LRP6	0
29969	MDFIC	0.027
4318	MMP9	0
79923	NANOG	0.042
5494	PPM1A	0.004
9232	PTTG1	0.043
5978	REST	0.037
6929	TCF3	0.002
6925	TCF4	0.001
6932	TCF7	0.035
6934	TCF7L2	0.005
7074	TIAM1	0
7422	VEGFA	0.005
11197	WIF1	0

Figure 2. Schematic visualization of dysregulated networks in KEGG database and representation of WNT gene expression profiles. (A) Visualization of WNT signaling pathway in the KEGG database. Highlighted genes are differentially expressed and red-starred pathways are overrepresented in AC133$^+$ AML cells. (B) Heat map of the differentially expressed WNT-associated genes. The color bar under the patient sample dendrogram identifies AML samples (red) and healthy controls (blue). The names, accession numbers, as well as *P* values for the differentially overexpressed and underexpressed genes are shown in the right panels.

($P < .05$), DAVID selected 24 KEGG pathways ($P < .05$), and the dysregulated pathway analysis selected 3 KEGG pathways ($P < .05$). As shown in Table W2, DAVID ranks the WNT signaling pathway ($P = .022$) among the first 10 dysregulated pathways in AC133$^+$ AML cells. The visualization of the WNT molecular interaction in KEGG database is presented in Figure 2*A*.

It is worth noting that different statistical methods agree in identifying the WNT pathway as a significant dysregulated pathway in AC133$^+$ AML cells. Moreover, the WNT signaling pathway in KEGG is selected as overrepresented in AC133$^+$ AML stem cells by both GOStats and DAVID. Taken together, the functional enrichment methods select the term "WNT receptor signaling pathway" (GO:0016055) as the most specific self-renewal associated dysregulated pathway.

WNT Gene Expression Profiles of Normal and Leukemia Long-term Reconstituting AC133$^+$ Cells

To obtain insights into the WNT pathway in AC133$^+$ leukemia cells, we focused our analysis on the probe sets annotated to "WNT receptor signaling pathway" GO class or to any of its children GO terms. The resulting probe set list was complemented with the probes mapping to genes in a manually curated list of WNT target genes and with probes mapping to other well-known WNT genes, not included in the previous two lists. The total list of analyzed WNT genes includes 480 probe sets, mapping to 193 different genes (Table_A in http://homes.dsi.unimi.it/~re/TRdataset/). To assess differential expression of WNT genes, we employed Welch *t* tests (two-tailed) on the 480 probe sets, thus identifying 103 differentially expressed genes ($P < .05$; Figure 2*B*). Genes shown to be highly AML-specific include the WNT ligands *WNT2B*, *WNT6*, *WNT10A*, and *WNT10B* [14], the WNT/β-catenin signaling agonists including *SMYD3* [31], *DKK2* [32], *SOX4* [33], *PROP-1* [34], and *PYGO2* [35,36], antagonists including *WIF-1* [37], *KLHL12* [38], *LRP6* [39], *KREMEN1* [40], *E2F1* [41], *DACT1* [42], and *HBP1* [43], and the deregulated WNT targets including *STAT3*, *MYCN*, *ABCC4*, *DLX3*, *MARK4*, *RUNX2*, *CD24*, and *CD44* [44]. Collectively, these data are consistent with ligand-dependent activation of the regeneration-associated WNT pathway [14].

We also investigated whether the expression of the WNT genes varied between the risk groups in AML (favorable, intermediate, and adverse) revised by Smith et al. [24]. Clustering results of AML cases restricted to WNT genes show that the risk groups are not clearly distinguishable in separate clusters (Figure 2*B*). Analysis of variance between groups confirms these results: only 3 (*ABCC4*, *HBP1*, and *NDP*) of 193 WNT-related genes are differentially expressed across the three categories ($P < .05$). Thus, our data do not support a significant distinction between risk groups in AML patients. This statement should be considered with caution, because the cardinality of the subgroups is relatively low (6 favorable, 13 intermediate, and 14 adverse samples).

Hyperactive WNT Signaling Resulted Activated in Diffuse AC133^{bright} AML Cells Expressing the Hematopoietic Regenerative Molecule WNT10B

Most of what is known about hematopoietic regeneration point to WNT signaling pathway and specifically to *WNT10B* [13,45]; therefore,

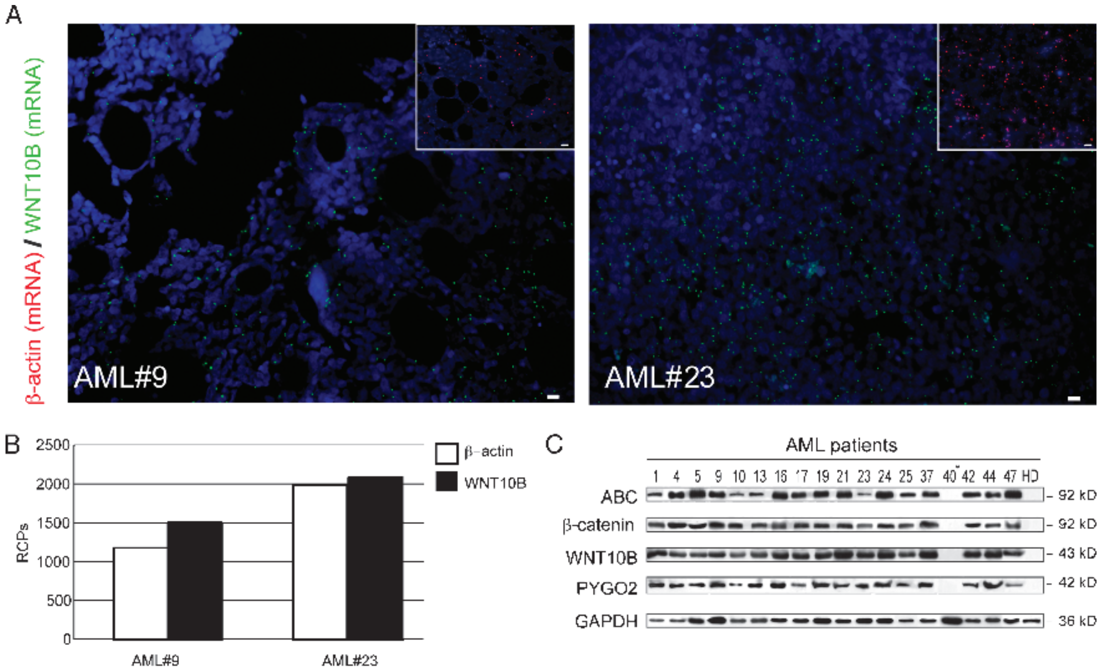

Figure 3. Altered WNT signaling in AC133$^+$ AML cells. (A) Detection with padlock probe and target-primed rolling circle amplification of individual *WNT10B* transcripts on BM slides from AML patients. Green RCPs represent *WNT10B* transcripts, and red RCPs represent β-actin transcripts in consecutive sections. Cell nuclei are shown in blue. Images were acquired with ×20 magnification. Scale bar, 10 μm. (B) The quantification of RCPs was done on three ×20 images of BM biopsies of AML patients. For quantification, the numbers of RCPs of each image were counted digitally using CellProfiler software. The average of RCPs for each sample was calculated and it is reported as a ratio between β-actin and WNT RCPs. (C) Immunoblot analysis of ABC, β-catenin (as detected with the N-terminal pan–β-catenin antibody), WNT10B, and Pygopus 2 protein expression in AC133$^+$ cell fractions from 18 patient samples and 1 healthy donor introduced as control. GAPDH, loading control. HD, healthy donor; *therapy-related secondary AML.

we investigated how expression of *WNT10B* is related to AML phenotype. To fully understand mRNA distribution of WNT10B within BM sections, we focused on the application of single molecule detection methods. *In situ* mRNA detection by target-primed rolling circle amplification analysis offers high sensitivity and localized detection within single cells and tissues [15]. Following this approach, we detected *WNT10B*-related transcript in BM sections obtained at diagnosis from two randomly selected patients. *β-Actin* was included as a reference transcript in consecutive sections. Visualization by using high-performance fluorescence microscopy showed a diffuse localization pattern in the tissues (Figure 3*A*). Signal distribution and RCP quantification showed a *β-actin*/*WNT10B* ratio close to 1, suggesting a constitutive activation of *WNT10B* transcription in the BM (Figure 3*B*). In addition, we analyzed transcriptional activation of canonical WNTs focusing on genes that have been shown to be potent regulators of stem cell functions. N-terminally dephosphorylated β-catenin (ABC) was increasingly accumulated as determined by immunoblot analysis (Figure 3*C*). Remarkably, we confirmed a dramatic increase in WNT10B expression in all patient samples, except for one, reanalyzed by immunoblot (Figure 3*C*). Interestingly, the only AML patient negative for the WNT10B expression (AML No. 40 in Table W1) was affected by therapy-related AML. According to the biologic relevance of PYGO2 in promoting the responsiveness of WNT signaling [35,36], diffuse overexpression was detected by immunoblot (Figure 3*C*). To better elucidate the impact of the broad WNT10B overexpression on the leukemic microenvironment, we examined its expression in histologic preparations of BM from five randomly selected AML patients at diagnosis. Double immunostaining for WNT10B and ABC, followed by ImageJ analysis, confirmed that WNT10B was expressed by a high proportion of leukemic cells. We next examined by immunostaining a number of BM biopsy sections from five randomly selected cases. In all the analyzed samples, the AC133 immunostaining revealed islands of highly positive cells (AC133$^{\text{bright}}$) in an estimated proportion of 8% of cells, amid AC133$^{\text{dim}}$ or negative tumor blasts (Figure 4*A*). AC133$^{\text{bright}}$ cells correlated with accumulation of ABC (Figure 4, *B* and *C*). WNT10B antibody staining was also detectable in interstitial spaces, suggesting its secretion and release in the BM microenvironment (Figure 4*D*, top). The slides revealed that WNT10B is diffusely expressed (Figure 4, *A* and *D*) but that only the AC133$^{\text{bright}}$ small cells (8–10 μm diameter of the nuclei), with a clonal appearance and increased N/C ratio, shared the WNT signaling activation signature represented by accumulation of ABC [46], likely induced through an autocrine/paracrine mechanism (Figure 4, *B* and *D*, top).

AC133$^+$ Leukemic Cells Express and Secrete WNT10B in a Primary Cell Culture

The notion that primary cell cultures closely mimic the *in vivo* state and generate more physiologically relevant data led us to establish a primary AC133$^+$ cell culture (A46). A46 cells, with diploid karyotype, were selected from a 66-year-old male at diagnosis of AML-M2 (AML No. 46 in Table W1). Immunophenotype of MNCs before selection revealed a dominant CD133.1$^+$CD34$^+$CD38$^-$CD45$^+$CD117$^+$ blast population (59%; Figure 5*A*), representing an optimal source to establish an LIC-enriched primary culture. Recently published data implicate the existence of an immunophenotypic hierarchy in AML, with a minority of CD38$^-$CD45$^+$ cells giving rise to CD38$^+$CD45$^+$ "GMP-like" cells at the apex of an LIC hierarchy [10]. The latter finding seems to suggest that CD38$^-$CD45$^+$ cells start to gain CD38 expression after AC133 selection procedures as observed in sorted cells (Figure 5*A*). Comparative analysis of spotted AC133-selected A46 leukemic and normal cells by

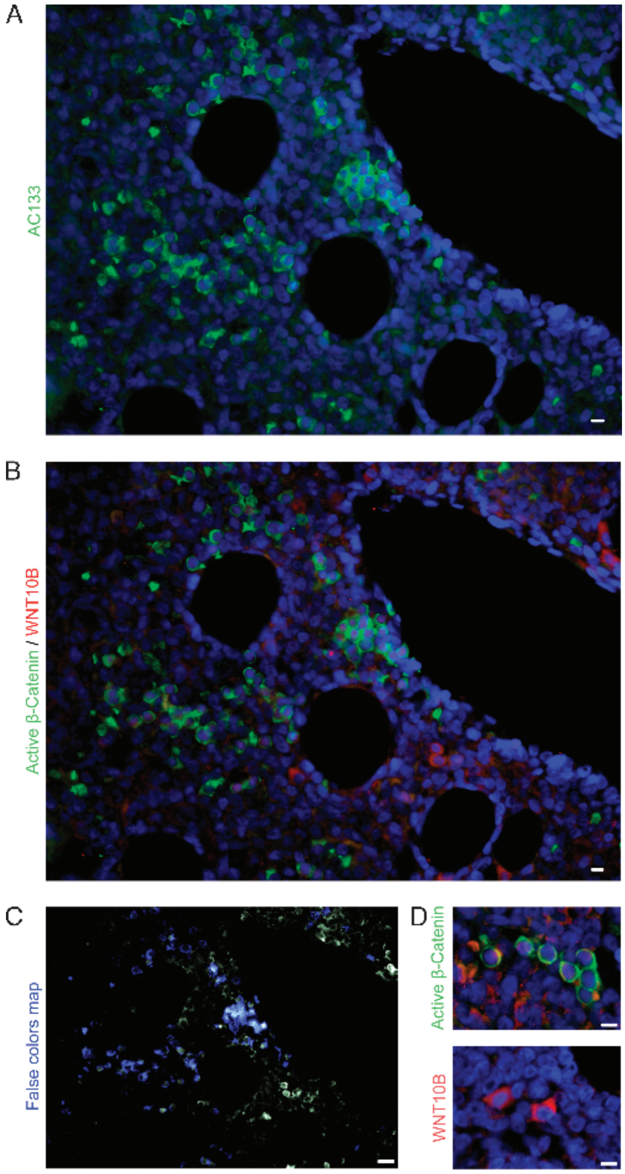

Figure 4. β-Catenin activation in the subpopulation of AC133$^{\text{bright}}$ AML cells expressing WNT10B. (A) Representative immunostaining micrographs show green fluorescence of cells expressing AC133 in a BM section of AML No. 9 (Table W1). Cell nuclei are shown in blue. Scale bar represents 10 μm. (B) Co-staining of BM from AML No. 9 adjacent serial section for expression of ABC (green) and WNT10B (red). Cell nuclei are shown in blue (DAPI). (C) False color maps of ABC/WNT10B double positive cells (blue) were obtained using an automatic threshold based on the moments algorithm implemented in the ImageJ program. DAPI staining was used to identify nuclei. Images obtained crossing ABC masks with WNT10B signals were used to count the percentage of ABC/WNT10B double positive cells over the total number of cells. The macro was validated against a trained experimenter over a sample of 830 total cells from eight different images. Differences in results were restricted to less than 0.01%. (D) Morphologic detail of cells showing intense specific staining for ABC (top panels) and WNT10B (bottom panels). All images were acquired with a ×40 objective. Scale bars represent 10 μm. Representative images of at least three serial slides from five randomly selected patients.

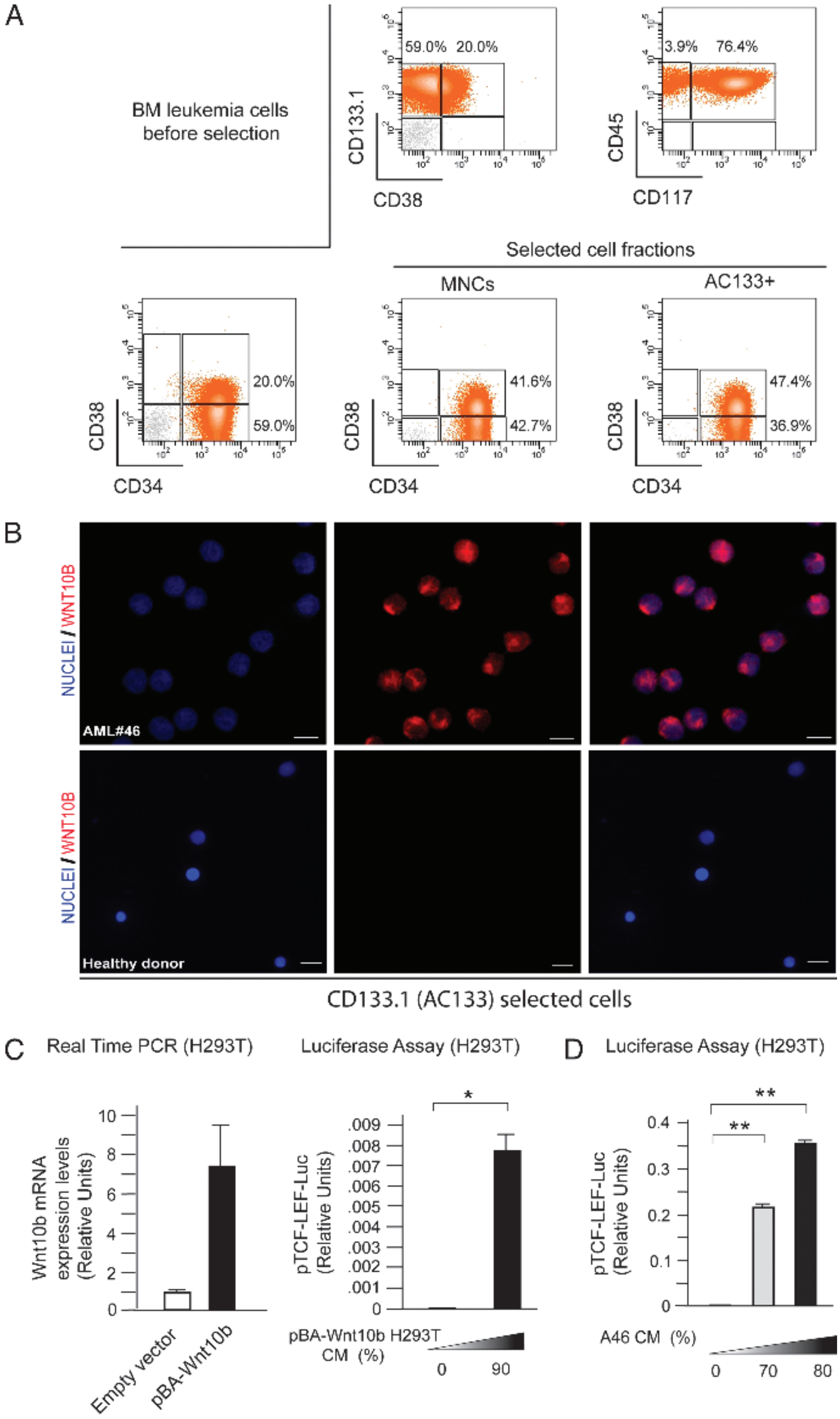

Figure 5. AC133$^+$ A46 cells express and release WNT10B. Dot plots of the immunophenotype analysis from AML No. 46 BM MNCs at diagnosis and after selection. (A) Patterns of CD38/CD133.1 (top left), CD117/CD45 (top right), and CD34/CD38 (bottom left) co-staining were gated on BM AML cells before selection. Representative CD34 and CD38 expression on Ficoll-selected MNCs (bottom center) and AC133-sorted cells before culture (bottom right) is shown. Percentages on total cellularity are shown for gated AML populations. (B) Immunostaining assessment for WNT10B in AC133$^+$ populations from A46 (top panels) or healthy donor (bottom panels). Representative images of at least five serial slides. Blue, nuclei; red, WNT10B; merge, WNT10B/DAPI. All images were acquired with a ×40 objective. Scale bars represent 10 μm. (C and D) TOPFlash reporter assay showing luciferase expression driven by eight TCF/lymphoid-enhancing factor (LEF) binding sites. (C) Positive control was obtained by CM of pBA-*WNT10B*–transfected H293T cells. Expression of *WNT10B* was evaluated in pBA-*WNT10B*–transfected H293T by real-time PCR (left). TOPFlash reporter assay shows luciferase expression induced in Super 8x TOPFlash–H293T cells by pBA–*WNT10B* H293T CM (right). (D) TOPFlash reporter assay showing dose-dependent luciferase expression induced in Super 8x TOPFlash–H293T cells by A46 CM. Significance was evaluated by the unpaired Student's *t* test: $*P < .05$; $**P < .001$. Data represent the mean ± SD of triplicate reactions and are representative of three independent experiments.

immunostaining revealed WNT10B expression in all A46 AC133$^+$ cells (Figure 5*B*, top), whereas normal BM-derived AC133$^+$ cells resulted negative (Figure 5*B*, bottom). To further investigate whether the endogenous WNT production had any paracrine effect, we used A46 CM to evaluate β-catenin–mediated transcriptional activation. To this aim, HEK293T cells (H293T), transfected with Super 8x TOPFlash β-catenin/TCF transcription–based reporter construct, were exposed either to pBA–*WNT10B* H293T CM as control (Figure 5*C*) or A46 CM. This construct could be efficiently expressed in a dose-dependent manner when transiently exposed to A46 CM for 12 hours (Figure 5*D*).

AC133 Is Expressed on Functional A46 AML LSC

To complement the *in vitro* observations, we tested whether AC133 was expressed on functional A46 AML LSC. We transplanted A46 cells into sublethally irradiated (5 Gy) 6-week-old Rag2$^{-/-}$γc$^{-/-}$ mice via the tail vein. This highly immunodeficient mouse strain lacks mature B, T, and natural killer (NK) cells, supporting efficient engraftment of human AML [16]. Transplanted mice were killed at 3 to 8 weeks after transplantation and analyzed for engraftment of human leukemia cells in BM (Figure 6*A*). The results of a typical experiment from three transplanted mice (M1–M3) are shown in Figure 6, with AC133$^+$ A46 cells showing engraftment of human CD45 (hCD45) cells. We confirmed that engrafted hCD45$^+$ cells were human myeloid leukemia blasts by measuring CD34/CD38/CD133 expression (Figure 6*B*).

Transplantation of A46 Induces Ectopic Axial Structure Formation in Zebrafish Embryo by WNT Signaling Activation

To bring our functional analyses full circle, we explored the physiological relevance of tumor-derived WNT signals by using the developing zebrafish as a biosensor. We hypothesized that WNT-secreting A46 cells transplanted into developing zebrafish embryos might act as

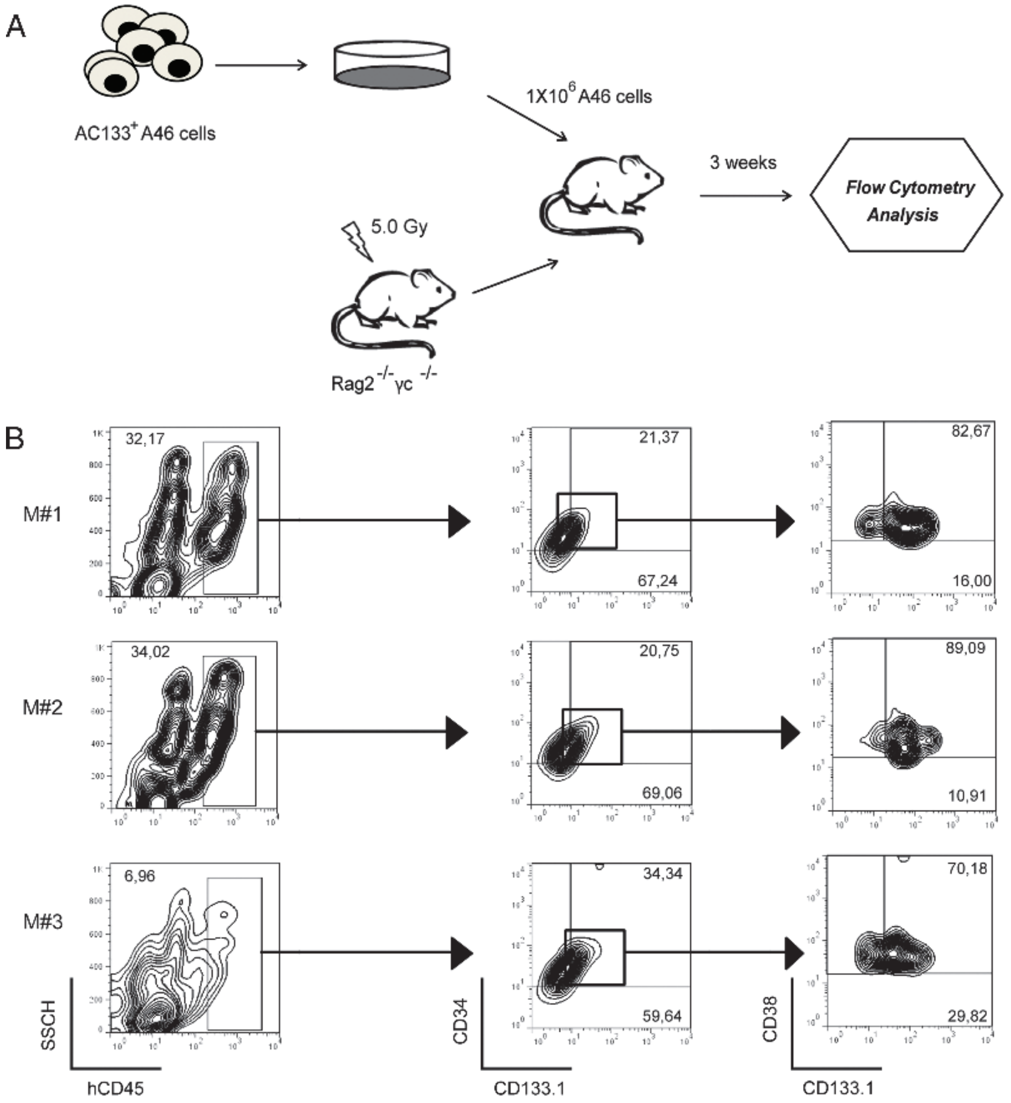

Figure 6. AC133$^+$ A46 cell transplantation in Rag2$^{-/-}$γc$^{-/-}$ mice. (A) Overview of the experimental design: 1 × 10^6 AC133$^+$ A46 cells were injected into sublethally irradiated Rag2$^{-/-}$γc$^{-/-}$ mice through the tail vein. Three weeks after transplantation, BM cells were collected and analyzed by flow cytometry. (B) Expression profiles of three recipient mice (M1–M3) are shown. hCD45$^+$ population was identified in BMs of mice, and within hCD45$^+$, the expression patterns of hCD34 and hCD133.1 (AC133) were analyzed. Cells were separated in subpopulations according to the expression of hCD34 and hCD133.1 and then analyzed for hCD38 and hCD133.1 expressions.

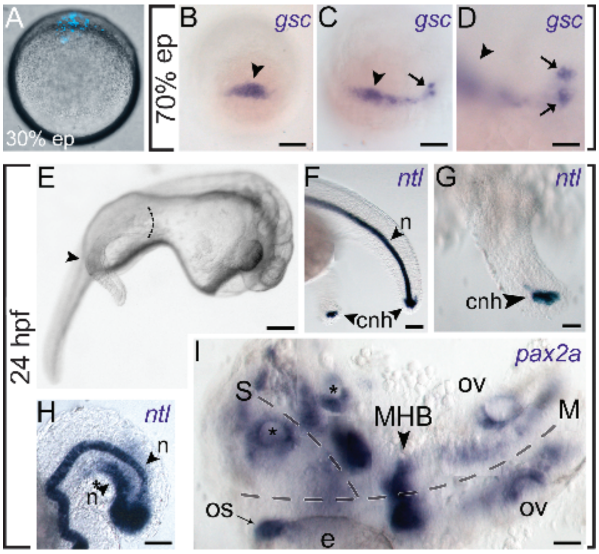

Figure 7. A46 AML cells induce ectopic gene expression and secondary body axis formation upon transplantation in zebrafish embryos. (A) Fluorescence microscopy of a live zebrafish embryo at 30% of epiboly (lateral view) transplanted at 3 hpf at the animal pole region with A46 cells previously blue-stained with Hoechst 33342. (B–D) Dorsal side view of 70% epiboly-stage embryos hybridized with a *gsc*-specific probe. Embryos have been injected with (B) normal AC133$^+$ cells as control or (C and D) A46 AML cells. The arrowheads indicate the *gsc* endogenous signal, while arrows specify the position of zebrafish cells expressing ectopic *gsc*. (E) Bright-field microscopy of a 24-hpf zebrafish embryo injected with A46 AML cells (lateral view). The arrowhead and the dotted line indicate the secondary trunk/tail induced by A46 cells. (F, G) The embryo in E has been hybridized with a probe specific for the notochord and tail bud marker *ntl*. (F) The probe labels the notochord (n) in the endogenous trunk and the chordoneural hinge (cnh) in both tails (G, higher magnification). (H) Tail of a 24-hpf embryo hybridized with *ntl*-specific probe. The endogenous (n) and ectopic (*n) *ntl* signals run parallel along the axis of the embryo, indicating the presence of additional axial structures. (I) Dorsal view of a 24-hpf embryo that developed an ectopic head on the side of the endogenous one, as indicated by the expression of the brain marker gene *pax2a*. The dotted lines indicate the main (M) and secondary (S) axes. The optic stalk (OS) in close vicinity to the eye (e), the midbrain-hindbrain boundary (MHB), and the otic vesicles (OV) of the embryo are stained with the *pax2a* riboprobe, as well as several areas of the ectopic head (the asterisks indicate the two clearly recognizable additional otic vesicles). The image is composed of different pictures corresponding to several focal planes, since the embryo is not flat, and a single focal plane cannot comprise all the labeled structures belonging to the main and secondary axes. Scale bars represent 125 μm (A–D), 150 μm (E), 40 μm (F), 15 μm (G and I), or 25 μm (H).

ectopic sources of maternal WNT ligands. Cell-grafted embryos, injected at or before the mid-blastula transition stage ($\sim$3 hpf) with Hoechst 33342 fluorescently labeled A46 cells (Figure 7*A*), showed the expression of the organizer-specific gene *goosecoid* (*gsc*). Expression of *gsc* is typically initiated by the nuclear translocation of maternal β-catenin triggered by the activation of the WNT signaling. While normal AC133$^+$ cells did not alter the normal expression of the gene (Figure 7*B*), approximately 30% of the embryos grafted with A46 cells ($n = 208$) displayed both the expansion of the *gsc* endogenous domain and the activation of the gene in ectopic positions (Figure 7, *C* and *D*).

Consistent with our hypothesis, the A46 cells retain a dorsal organizer–inducing activity possibly correlated with their strong WNT signaling activation. In addition, grafted embryos developed secondary axial structures, ranging from additional tail tissues (Figure 7, *E–H*) to an almost fully formed ectopic head (Figure 7*I*). Control embryos grafted with normal BM-derived AC133$^+$ cells, devoid of any WNT signaling activity, did not display alterations of the normal phenotype (data not shown). The identity of the additional tail structures was confirmed by *in situ* hybridization staining for the notochord and tail bud marker *ntl* [47], whereas the emergence of ectopic head structures was highlighted by *pax2a* labeling optic stalk, midbrain–hindbrain boundary, and otic vesicles. These results imply that A46 cells might determine the establishment of an additional source of signal, with a Nieuwkoop center–like activity, able to induce an extra dorsal organizer, similarly to the endogenous situation at mid-blastula transition, when maternal WNT/β-catenin signaling initiates the formation of the dorsal organizer [48]. In zebrafish, secondary axis can be also induced by Nodal, a highly evolutionarily conserved morphogen belonging to the transforming growth factor–β superfamily and able to activate *gsc* expression [49]. Therefore, we investigated the possible involvement of the Nodal signaling pathway in the dorsal organizer induction mediated by A46 cells. The complete lack of *Nodal* expression observed after microarray analyses was confirmed by qualitative RT-PCR in A46 and samples from six different AML patients (Figure W1), allowing to exclude any *Nodal* contribution from A46 cells to the formation of the secondary axis and induction of *gsc* expression.

Discussion

The deceivingly homogeneous, undifferentiated morphology of the AML blasts is now known to mask a heterogeneous collection of cells that recapitulate the hierarchy of precursor cells that characterize the normal process of blood-cell differentiation. The concept that LIC properties occur in a self-renewing non-HSC progenitor cell population, preceded by the expansion of a preleukemic LT-HSC, has been recently reinforced [4,10]. However, the molecular functions responsible for the preleukemic LT-HSC expansion and the acquisition of self-renewal ability in AML remained poorly defined.

The WNT/β-catenin pathway has been show to play a critical role in the regulation of cell proliferation, differentiation, and apoptosis of different malignant entities. It is highly regulated in AML [50] and also involved in the self-renewal process of HSCs. WNT/β-catenin pathway requirement for LIC development in AML has emerged in mouse model [21]. Recent studies revealed aberrant WNT signaling in AML cells that is independent from the occurrence of AML-associated fusion proteins or mutations in tyrosine kinase receptors [reviewed in 20].

The results presented here using gene expression microarrays and pathway analysis provide direct evidence that the WNT/β-catenin signaling is diffusely activated in the AC133$^+$ AML population, with a specific transcriptional signature involving overexpression of the WNT pathway agonists and down-modulation of the major antagonists.

Although the long-term reconstituting human HSC marker AC133 has been detected in a majority of CD34$^+$ AML [51], no extensive data concerning the role of AC133 in AML were available.

Analysis of freshly fractionated cells from AML patients showed that active WNT signaling was predominant in the population highly enriched for the AC133 marker. Notably, *WNT2B*, *WNT6*, *WNT10A*, and *WNT10B*, known to promote hematopoietic tissue regeneration [13,14], are the WNT mediators specifically upregulated in the AC133$^+$

AML cells. In addition, there is evidence that in the hematopoietic system *WNT10B* is specifically and significantly upregulated following an injury and that WNT10B acts to enhance the growth of HSCs [13]. It is also worth noting that greater fold expansion of murine HSC progenitors was obtained after WNT10B CM exposure [52]. Consistent with the latter observations, we showed a dramatic increase of WNT10B expression and protein release within the microenvironment in the large majority of samples from AML patients recruited to this study, with the exception of the unique therapy-related AML patient. In accordance with previous reports [52], we have not detected *WNT10B* gene expression in normal AC133$^+$ hematopoietic cells. Moreover, our data also point to the strong expression of the WNT target gene *CD44* and the loss of *CD24*, according to the expression of CD44$^+$CD24$^-$AC133$^+$ phenotype that defines a putative cancer stem cell population also in breast tumors [53]. Interestingly, Dick et al. have shown that CD44 is a key regulator of AML LSC function and that targeting it eradicates LSCs [54]. In light of the higher homeostatic range of WNT/β-catenin signaling occurring upon an acute injury [55], our study demonstrated the involvement of the regeneration-associated WNT signaling in AC133$^{\text{bright}}$ AML cell fraction. The term "regeneration" has been used to define the physiological phenomena of reconstitution from damage due to injury or disease. Hematopoietic regenerative-associated WNT ligand (WNT10B) is expressed at mRNA and protein levels on both leukemic blasts and stromal-like cells, indicating a possible autocrine/paracrine involvement of WNT in the BM microenvironment. Conversely, activation of WNT signaling marked by expression of the dephosphorylated β-catenin was restricted to the smaller population of AC133$^{\text{bright}}$ leukemic cells. The reasons for these differences are unclear, but it is possible that β-catenin activation by WNTs requires the expression of specific Fzd receptors, conferring a "responsive" phenotype, only restricted to a rare population of cells. In the HSC biology, a fundamental question is how self-renewal is controlled; several lines of evidence point to Notch for a WNT-mediated maintenance of undifferentiated HSCs [56]. Recent studies, examining the molecular targets of WNT10B, have highlighted the nuclear factor κB and Notch pathways as downstream targets of WNT10B [57]. It is tempting to speculate that WNT10B and other regeneration-associated WNTs (i.e., WNT2B, WNT6, and WNT10A) integrate with other signals, such as Notch, to drive oncogenic renewal. Because activation of WNT signaling can increase the ability of HSCs to reconstitute the hematopoietic system of lethally irradiated mice, we transplanted the AC133$^+$ A46 cells into irradiated Rag2$^{-/-}\gamma c^{-/-}$ mice. Different papers have been recently published in which comparisons in the engraftment ability of different immunodeficient murine models were made. The variability of the reconstitution seemed to be mainly linked to the degree of immunodepression of the murine host. Rag2$^{-/-}\gamma c^{-/-}$ represents a powerful model to verify the biologic and malignant characteristics of human tumor cells. It is characterized by immunodeficiency of T and B cells caused by Rag2 knockout, coupled with the NK deficit mediated by the absence of the γc interleukin receptor chain [16]. The results of our experiments indicate that AC133 is expressed on AML LSC in the A46 primary cells, suggesting that regeneration-associated WNT expression signature is enriched in primary human AML LSC–containing fraction.

Regeneration requires the rapid expansions of HSCs; this process is often mediated by reactivation of developmental signal transduction pathways, such as BMP and WNT [45,58]. In the early embryo, the WNT factors induce the nuclear translocation of β-catenin, which triggers the formation of the dorsal organizer through the activation of zygotic dorsal-specific genes [59]. Such WNT-induced cascade of events results in the establishment of the embryonic dorsoventral axis [47]. To test the hypothesis that regeneration-associated WNT signaling is involved in AML LSC expansion, we used a zebrafish embryonic model as a tool by examining the ability of A46 primary leukemia cells to modulate embryonic microenvironment. Therefore, we used zebrafish embryos to show that A46 cells prompt secondary axis development, inducing the formation of a dorsal organizer–like structure, possibly through the secretion of different WNT ligands. The mechanisms promoting organizer formation are known to involve cooperation between Nodal and WNT signaling. However, implanted cell lines with different origin induce the dorsal organizer independently from the Nodal signaling [60]. Here, we demonstrated that the A46-dependent alteration of zebrafish development and activation of the organizer-specific gene *gsc* are not reliant on Nodal activity.

In summary, the findings we report here implicate, for the first time, that regeneration-associated ligand-dependent WNT signaling exceeds the homeostatic range in the majority of human AML cases and affects responsive AC133$^{\text{bright}}$ cells whose renewal is promoted by WNT pathway activity *in vivo*. These results not only support that AC133 is expressed on functional leukemia stem cells, but because developmental signal transduction pathways are often reactivated during regeneration, we also show that AC133$^+$ AML cells induce the formation of a dorsal organizer–like structure in zebrafish embryos.

Finally, these studies suggest that the regenerative WNT signaling is a stem cell–associated function altered, as a common feature, in AC133$^{\text{bright}}$ AML leukemia stem cell fraction. Future studies will be required to demonstrate a pathogenic association of AC133$^{\text{bright}}$ LSC regeneration response with AML, in terms of tumorigenicity, clinicopathologic features, and patient outcomes.

Acknowledgments

We thank the patients with AML and their families. We also thank E. Cattaneo, G. Simonutti, R. Bacchetta, and N. Santo for support with microscopy facilities, U. Landegren and O. Soderberg for supporting our activities at Rudbeck Laboratory, B. Scarpati and E. Calzavara for assistance with flow cytometry, R. Brusamolino and L. Pezzetti for assistance with patients' samples, L. Prosperi for support with zebrafish procedures, and S. Pozzi for helpful discussion.

References

[1] Cozzio A, Passegué E, Ayton PM, Karsunky H, Cleary ML, and Weissman IL (2003). Similar MLL-associated leukemias arising from self-renewing stem cells and short-lived myeloid progenitors. *Genes Dev* **17**, 3029–3035.

[2] Somervaille TC, Matheny CJ, Spencer GJ, Iwasaki M, Rinn JL, Witten DM, Chang HY, Shurtleff SA, Downing JR, and Cleary ML (2006). Hierarchical maintenance of MLL myeloid leukemia stem cells employs a transcriptional program shared with embryonic rather than adult stem cells. *Cell Stem Cell* **4**, 129–140.

[3] Kirstetter P, Schuster MB, Bereshchenko O, Moore S, Dvinge H, Kurz E, Theilgaard-Mönch K, Månsson R, Pedersen TA, Pabst T, et al. (2008). Modeling of C/EBPα mutant acute myeloid leukemia reveals a common expression signature of committed myeloid leukemia-initiating cells. *Cancer Cell* **13**, 299–310.

[4] Bereshchenko O, Mancini E, Moore S, Bilbao D, Månsson R, Luc S, Grover A, Jacobsen SE, Bryder D, and Nerlov C (2009). Hematopoietic stem cell expansion precedes the generation of committed myeloid leukemia-initiating cells in C/EBPα mutant AML. *Cancer Cell* **16**, 390–400.

[5] Beachy PA, Karhadkar SS, and Berman DM (2004). Tissue repair and stem cell renewal in carcinogenesis. *Nature* **432**, 324–331.

[6] Goessling W, North TE, Loewer S, Lord AM, Lee S, Stoick-Cooper CL, Weidinger G, Puder M, Daley GQ, Moon RT, et al. (2009). Genetic interaction of PGE2 and Wnt signaling regulates developmental specification of stem cells and regeneration. *Cell* **136**, 1136–1147.

[7] Zhao C, Chen A, Jamieson CH, Fereshteh M, Abrahamsson A, Blum J, Kwon HY, Kim J, Chute JP, Rizzieri D, et al. (2009). Hedgehog signalling is essential for maintenance of cancer stem cells in myeloid leukaemia. *Nature* **458**, 776–779.

[8] Hofmann I, Stover EH, Cullen DE, Mao J, Morgan KJ, Lee BH, Kharas MG, Miller PG, Cornejo MG, Okabe R, et al. (2009). Hedgehog signaling is dispensable for adult murine hematopoietic stem cell function and hematopoiesis. *Cell Stem Cell* **4**, 559–567.

[9] Taussig DC, Miraki-Moud F, Anjos-Afonso F, Pearce DJ, Allen K, Ridler C, Lillington D, Oakervee H, Cavenagh J, Agrawal SG, et al. (2008). Anti-CD38 antibody-mediated clearance of human repopulating cells masks the heterogeneity of leukemia-initiating cells. *Blood* **112**, 568–575.

[10] Goardon N, Marchi E, Atzberger A, Quek L, Schuh A, Soneji S, Woll P, Mead A, Alford KA, Rout R, et al. (2011). Coexistence of LMPP-like and GMP-like leukemia stem cells in acute myeloid leukemia. *Cancer Cell* **19**, 138–152.

[11] Yin AH, Miraglia S, Zanjani ED, Almeida-Porada G, Ogawa M, Leary AG, Olweus J, Kearney J, and Buck DW (1997). AC133, a novel marker for human hematopoietic stem and progenitor cells. *Blood* **90**, 5002–5012.

[12] Mizrak D, Brittan M, and Alison MR (2007). CD133: molecule of the moment. *J Pathol* **214**, 3–9.

[13] Congdon KL, Voermans C, Ferguson EC, DiMascio LN, Uqoezwa M, Zhao C, and Reya T (2008). Activation of Wnt signaling in hematopoietic regeneration. *Stem Cells* **26**, 1202–1210.

[14] Katoh M and Katoh M (2006). Cross-talk of WNT and FGF signaling pathways at GSK3β to regulate β-catenin and SNAIL signaling cascades. *Cancer Biol Ther* **5**, 1059–1064.

[15] Larsson C, Grundberg I, Söderberg O, and Nilsson M (2010). *In situ* detection and genotyping of individual mRNA molecules. *Nat Methods* **7**, 395–397.

[16] Shinkai Y, Rathbun G, Lam KP, Oltz EM, Stewart V, Mendelsohn M, Charron J, Datta M, Young F, Stall AM, et al. (1992). RAG-2-deficient mice lack mature lymphocytes owing to inability to initiate V(D)J rearrangement. *Cell* **68**, 855–867.

[17] Majeti R, Becker MW, Tian Q, Lee TL, Yan X, Liu R, Chiang JH, Hood L, Clarke MF, and Weissman IL (2009). Dysregulated gene expression networks in human acute myelogenous leukemia stem cells. *Proc Natl Acad Sci USA* **106**, 3396–3401.

[18] Reya T, Duncan AW, Ailles L, Domen J, Scherer DC, Willert K, Hintz L, Nusse R, and Weissman IL (2003). A role for Wnt signalling in self-renewal of haematopoietic stem cells. *Nature* **423**, 409–414.

[19] Staal FJT and Luis TC (2010). Wnt signaling in hematopoiesis: crucial factors for self-renewal, proliferation, and cell fate decisions. *J Cell Biochem* **109**, 844–849.

[20] Mikesch JH, Steffen B, Berdel WE, Serve H, and Müller-Tidow C (2007). The emerging role of Wnt signaling in the pathogenesis of acute myeloid leukemia. *Leukemia* **21**, 1638–1647.

[21] Wang Y, Krivtsov AV, Sinha AU, North TE, Goessling W, Feng Z, Zon LI, and Armstrong SA (2010). The Wnt/β-catenin pathway is required for the development of leukemia stem cells in AML. *Science* **327**, 1650–1653.

[22] Scheller M, Huelsken J, Rosenbauer F, Taketo MM, Birchmeier W, Tenen DG, and Leutz A (2006). Hematopoietic stem cell and multilineage defects generated by constitutive β-catenin activation. *Nat Immunol* **7**, 1037–1047.

[23] Kirstetter P, Anderson K, Porse BT, Jacobsen SE, and Nerlov C (2006). Activation of the canonical Wnt pathway leads to loss of hematopoietic stem cell repopulation and multilineage differentiation block. *Nat Immunol* **7**, 1048–1056.

[24] Smith ML, Hills RK, and Grimwade D (2011). Independent prognostic variables in acute myeloid leukaemia. *Blood Rev* **25**, 39–51.

[25] Brioschi M, Fischer J, Cairoli R, Rossetti S, Pezzetti L, Nichelatti M, Turrini M, Corlazzoli F, Scarpati B, Morra E, et al. (2010). Down-regulation of microRNAs 222/221 in acute myelogenous leukemia with deranged core-binding factor subunits. *Neoplasia* **12**, 866–876.

[26] Falcon S and Gentleman R (2007). Using GOstats to test gene lists for GO term association. *Bioinformatics* **23**(2), 257–258.

[27] Huang DW, Sherman BT, and Lempicki RA (2009). Systematic and integrative analysis of large gene lists using DAVID bioinformatics resources. *Nat Protoc* **4** (1), 55–57.

[28] Hatta K and Takahashi Y (1996). Secondary axis induction by heterospecific organizers in zebrafish. *Dev Dyn* **205**, 183–195.

[29] Thisse C, Thisse B, Schilling TF, and Postlethwait JH (1993). Structure of the zebrafish *snail1* gene and its expression in wild-type, *spadetail* and *no tail* mutant embryos. *Development* **119**, 1203–1215.

[30] Hess DA, Wirthlin L, Craft TP, Herrbrich PE, Hohm SA, Lahey R, Eades WC, Creer MH, and Nolta JA (2006). Selection based on CD133 and high aldehyde dehydrogenase activity isolates long-term reconstituting human hematopoietic stem cells. *Blood* **107**, 2162–2169.

[31] Hamamoto R, Silva FP, Tsuge M, Nishidate T, Katagiri T, Nakamura Y, and Furukawa Y (2006). Enhanced SMYD3 expression is essential for the growth of breast cancer cells. *Cancer Sci* **97**, 113–118.

[32] Mao B and Niehrs C (2003). Kremen2 modulates Dickkopf2 activity during Wnt/LRP6 signaling. *Gene* **302**, 179–183.

[33] Sinner D, Kordich JJ, Spence JR, Opoka R, Rankin S, Lin SC, Jonatan D, Zorn AM, and Wells JM (2007). Sox17 and Sox4 differentially regulate β-catenin/T-cell factor activity and proliferation of colon carcinoma cells. *Moll Cell Biol* **27**, 7802–7815.

[34] Olson LE, Tollkuhn J, Scafoglio C, Krones A, Zhang J, Ohgi KA, Wu W, Taketo MM, Kemler R, Grosschedl R, et al. (2006). Homeodomain-mediated β-catenin-dependent switching events dictate cell-lineage determination. *Cell* **125**, 593–605.

[35] Mieszczanek J, de la Roche M, and Bienz M (2008). A role of Pygopus as an anti-repressor in facilitating Wnt-dependent transcription. *Proc Natl Acad Sci USA* **105**, 19324–19329.

[36] Gu B, Sun P, Yuan Y, Moraes RC, Li A, Teng A, Agrawal A, Rhéaume C, Bilanchone V, Veltmaat JM, et al. (2009). Pygo2 expands mammary progenitor cells by facilitating histone H3 K4 methylation. *J Cell Biol* **185**, 811–826.

[37] Gehrke I, Gandhirajan RK, and Kreuzer KA (2009). Targeting the WNT/β-catenin/TCF/LEF1 axis in solid and haematological cancers: multiplicity of therapeutic options. *Eur J Cancer* **45**, 2759–2767.

[38] Angers S, Thorpe CJ, Biechele TL, Goldenberg SJ, Zheng N, MacCoss MJ, and Moon RT (2006). The KLHL12–Cullin-3 ubiquitin ligase negatively regulates the Wnt–β-catenin pathway by targeting Dishvelled for degradation. *Nat Cell Biol* **8**, 348–357.

[39] Li Y, Lu W, King TD, Liu CC, Bijur GN, and Bu G (2010). Dkk1 stabilizes Wnt co-receptor LRP6: implication for Wnt ligand-induced LRP6 down-regulation. *PloS One* **5**, e11014.

[40] Wang K, Zhang Y, Li X, Chen L, Wang H, Wu J, Zheng J, and Wu D (2008). Characterization of the Kremen-binding site on Dkk1 and elucidation of the role of Kremen in Dkk-mediated Wnt antagonism. *J Biol Chem* **22**, 23371–23375.

[41] Morris EJ, Ji JY, Yang F, Di Stefano L, Herr A, Moon NS, Kwon EJ, Haigis KM, Näär AM, and Dyson NJ (2008). E2F1 represses β-catenin transcription and is antagonized by both pRB and CDK8. *Nature* **25**, 552–556.

[42] Gao X, Wen J, Zhang L, Li X, Ning Y, Meng A, and Chen YG (2008). Dapper1 is a nucleocytoplasmic shuttling protein that negatively modulates Wnt signaling in the nucleus. *J Biol Chem* **283**, 35679–35688.

[43] Sampson EM, Haque ZK, Ku MC, Tevosian SG, Albanese C, Pestell RG, Paulson KE, and Yee AS (2001). Negative regulation of the Wnt–β-catenin pathway by the transcriptional repressor HBP1. *EMBO J* **20**, 4500–4511.

[44] Quéré R, Andradottir S, Brun AC, Zubarev RA, Karlsson G, Olsson K, Magnusson M, Cammenga J, and Karlsson S (2011). High levels of the adhesion molecule CD44 on leukemic cells generate acute myeloid leukemia relapse after withdrawal of the initial transforming event. *Leukemia* **25**, 515–526.

[45] Bowman TV, Tropouki E, and Zon LI (2012). Linking hematopoietic regeneration to developmental signaling pathways: a story of BMP and Wnt. *Cell Cycle* **11**, 424–425.

[46] Staal FJ, Noort Mv M, Strous GJ, and Clevers HC (2002). Wnt signals are transmitted through N-terminally dephosphorylated β-catenin. *EMBO Rep* **31**, 63–68.

[47] Lin X, Rinaldo L, Fazly AF, and Xu X (2007). Depletion of Med10 enhances Wnt and suppresses Nodal signaling during zebrafish embryogenesis. *Dev Biol* **303**, 536–548.

[48] Langdon YG and Mullins MC (2011). Maternal and zygotic control of zebrafish dorsoventral axial patterning. *Annu Rev Genet* **45**, 357–377.

[49] Schier AF (2003). Nodal signaling in vertebrate development. *Annu Rev Cell Dev Biol* **19**, 589–621.

[50] Siapati EK, Papadaki M, Kozaou Z, Rouka E, Michali E, Savvidou I, Gogos D, Kyriakou D, Anagnostopoulos NI, and Vassilopoulos G (2010). Proliferation and bone marrow engraftment of AML blasts is dependent on β-catenin signaling. *Br J Haematol* **152**, 164–174.

[51] Fauth F, Weidmann E, Martin H, Schneider B, Sonnhoff S, and Hoelzer D (2001). AC133 expression on acute myeloid leukemia blasts: correlation to FAB and to CD34 expression and possible implications for peripheral blood progenitor cell purging in AML. *Leuk Res* **25**(3), 191–196.

[52] Austin TW, Solar GP, Ziegler FC, Liem L, and Matthews W (1997). A role for the Wnt gene family in hematopoiesis: expansion of multilineage progenitor cells. *Blood* **89**, 3624–3635.

[53] Wright MH, Calcagno AM, Salcido CD, Carlson MD, Ambudkar SV, and Varticovski L (2008). *Brca1* breast tumors contain distinct CD44$^+$/CD24$^-$ and CD133$^+$ cells with cancer stem cell characteristics. *Breast Cancer Res* **10**, 1–16.

[54] Jin L, Hope KJ, Zhai Q, Smadja-Joffe F, and Dick JE (2006). Targeting of CD44 eradicates human acute myeloid leukemic stem cells. *Nat Med* **12**, 1167–1174.

[55] Angers S and Moon RT (2009). Proximal events in Wnt signal transduction. *Nat Rev Mol Cell Biol* **10**, 468–477.

[56] Duncan AW, Rattis FM, DiMascio LN, Congdon KL, Pazianos G, Zhao C, Yoon K, Cook JM, Willert K, Gaiano N, et al. (2005). Integration of Notch and Wnt signaling in hematopoietic stem cell maintenance. *Nat Immunol* **6**(3), 314–322.

[57] Mödder UI, Oursler MJ, Khosla S, and Monroe DG (2011). Wnt10b activates the Wnt, Notch and NFκB pathways in U2OS osteosarcoma cells. *J Cell Biochem* **112**(5), 1392–1402.

[58] Trompouki E, Bowman TV, Lawton LN, Fan ZP, Wu DC, DiBiase A, Martin CS, Cech JN, Sessa AK, Leblanc JL, et al. (2011). Lineage regulators direct BMP and WNT pathways to cell-specific programs during differentiation and regeneration. *Cell* **147**, 577–589.

[59] Lu FI, Thisse C, and Thisse B (2011). Identification and mechanism of regulation of the zebrafish dorsal determinant. *Proc Natl Acad Sci USA* **108**, 15876–15880.

[60] Hashiguchi M, Shinya M, Tokumoto M, and Sakai N (2008). Nodal/Bozozok-independent induction of the dorsal organizer by zebrafish cell lines. *Dev Biol* **321**, 387–396.

Table W1. Clinical Characteristics and Outcome of AML Patients.

No.	Age, y/Sex	FAB	Cytogenetics*	FLT3	NPM1	WBC, $\times 10^9$/L	MO Blast, %	EML	s-AML	Response to Induction	Relapse	Outcome
1	67/M	M2	45,XY,−7	wt	–	1.7	55	Absent	Yes[†]	CR	Yes	D/first res rel
2	45/M	M1	Complex karyotype	wt	–	1.7	60	Absent	No	CR	No	A/first CR
4	59/M	M4	46,XY,del(20)(q11;q13)	wt	–	3.5	32	Absent	No	CR	No	A/first CR
5	47/F	M4	46,XX	ITD	–	84.6	80	Skin	No	CR	No	A/first CR
6	76/F	M4	47,XX,+11	wt	–	–	–	Absent	Yes[†]	ref dis	n.a.	D/prim ref dis
9	20/M	M0	46,XY	wt	–	3.6	80	Absent	No	CR	Yes	A/second CR
10	62/F	M5a	46,XX	wt	–	69	90	Skin	No	CR	No	A/first CR
13	57/M	M1	46,XY,t(6;9)(p23;q34)	ITD	wt	39.7	89	Absent	No	ref dis	n.a.	D/prim ref dis
14	72/F	M2	46,XX	wt	–	–	–	Absent	No	ref dis	n.a.	D/prim ref dis
16	41/F	M2	46,XX	wt	wt	15.9	45	Absent	No	CR	No	A/first CR
17	29/M	M1	46,XY	ITD	wt	217.7	96	Absent	No	CR	Yes	D/first res rel
19	29/F	M1	46,XX,del(11)(q23)	wt	–	110.6	95	Skin	No	ref dis	Yes	D/first res rel
21	22/M	M1	46,XY	ITD	wt	16.7	75	Absent	No	CR	No	A/first CR
23	65/M	M1	46,XY	wt	wt	12.7	78	Absent	No	CR	Yes	A/second CR
24	59/M	M1	46,XY	wt	Exon 12	20.1	75	Absent	No	CR	Yes	A/first rel
25	39/F	M1	46,XX,del(11)(q23)	wt	wt	15.7	–	Absent	No	ref dis	n.a.	D/prim ref dis
30	41/M	M5a	46,XY	wt	wt	3.6	75	Absent	No	CR	Yes	A/first rel
32	52/F	M2	46,XX	wt	wt	2.7	55	Absent	Yes[†]	CR	No	D/TRM first CR
34	29/M	M0	46,XY,del(11)(q13;q23)	wt	wt	4	86	Absent	No	CR	Yes	D/first res rel
38	59/F	M1	46,XX	wt	Exon 12	1	82	Absent	No	CR	Yes	D/first res rel
39	51/M	n.a.	Complex karyotype	wt	wt	1.2	–	Absent	No	ref dis	n.a.	D/prim ref dis
40	55/F	M2	Complex karyotype	wt	wt	0.8	20	Absent	Yes[‡]	n.a.	n.a.	A/active dis
41	62/F	M4	46,XX	wt	wt	17	30	Skin	Yes[†]	CR	Yes	A/first res rel
42	65/F	M4	46,XX	wt	wt	1.2	60	Adnexal mass	No	ref dis	n.a.	A/prim ref dis
44	56/F	M2	46,XX,t(8;21)(q22;q22)	wt	wt	8.6	65	Absent	No	CR	Yes	A/second rel
46	66/M	M2	46,XY	ITD	wt	26.8	80	Absent	No	PR	n.a.	A/prim ref dis
47	62/F	M2	47,XX,+21	wt	Exon 12	23	12	Absent	Yes[†]	n.a.	n.a.	A/active dis
48	43/M	M5a	46,XY	ITD	Exon 12	63.9	85	Absent	No	CR	Yes	A/second CR
49	68/F	biphen.	45,XX,−7,t(9;22)(q34;q11)	wt	wt	8.1	70	Absent	No	CR	Yes	A/second CR
50	61/F	M4	Complex karyotype	wt	wt	8.8	35	Absent	No	ref dis	n.a.	D/prim ref dis
51	15/F	M5b	46,XX	wt	wt	118	84	CNS	No	CR	Yes	D/first res rel
52	33/M	M2	46,XY	wt	Exon 12	20.9	40	Absent	No	CR	No	A/first CR
53	51/F	M1	46,XX	wt	Exon 12	81.1	77	Absent	No	CR	No	A/first CR

A, alive; CR, complete remission; PR, partial remission; D, dead; ref dis, refractory disease; res rel, resistant relapse; biphen, biphenotypic; TRM, transplant-related mortality; s-AML, secondary AML; EML, extramedullary leukemia; n.a., not applicable.

*At diagnosis.

[†] Myelodysplastic AML.

[‡] Therapy-related AML.

Table W2. Top 10 Dysregulated KEGG Pathways in AC133$^+$ AML Cells.

Term	No. of Genes	*P*
Oxidative phosphorylation	78	9.9×10^{-7}
Focal adhesion	107	7.0×10^{-3}
Neurotrophin signaling pathway	70	7.3×10^{-3}
Ribosome	51	1.0×10^{-2}
Calcium signaling pathway	94	1.1×10^{-2}
Adherens junction	45	1.3×10^{-2}
Long-term potentiation	40	1.6×10^{-2}
Axon guidance	71	1.9×10^{-2}
WNT signaling pathway	80	2.2×10^{-2}
Ubiquitin-mediated proteolysis	73	2.3×10^{-3}

No. of genes is referred to KEGG pathway.

P is obtained through the modified Fisher exact test (EASE score in DAVID).

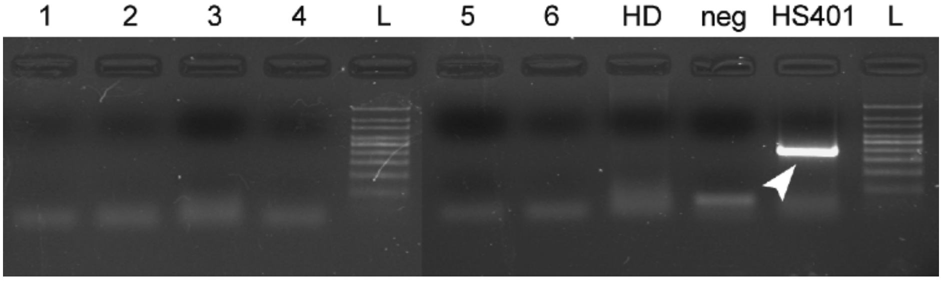

Figure W1. Nodal expression analysis on BM samples from AML patients. RT-PCR analysis has been performed to investigate the level of Nodal expression in AML samples from six different patients (lanes 1 to 6). The analysis has also been performed on BM specimen sampled from a healthy donor (lane HD), and monitored for quality with a positive control (lane HS401, human embryonic stem cell line HS401) and a no cDNA negative control (lane neg). A 100-bp molecular weight DNA ladder (Genespin) has been loaded onto the gel for amplicon sizing (lane L). The analysis pointed out the complete lack of *Nodal* expression in all the six samples tested, as well as, unsurprisingly, in the healthy donor. Arrowhead indicates the size of the Nodal-specific PCR product (392 bp) obtained with the following pair of primers: HuNODAL_ff2: 5′AGGGCGAGTGTCCTAATCCT and HuNODAL_rr: 5′CAGACTCCACTGAGCCCTTC. To further increase the sensitivity of the assay, we have subjected the PCRs to a second round of amplification using a semi-nested approach with the same reverse primer and with a nested forward primer (HuNODAL_ff1: 5′GAGGAGTTTCATCCGACCAA). The semi-nested PCR confirmed the total absence of *Nodal* expression in all the six samples analyzed, with the expected 366-bp product detected exclusively in the positive control (not shown, figure available upon request). To further increase the strength of the data, we have performed the same analysis on a second set of seven AML BM specimens, resulting in the exact same outcome (not shown, figure available upon request). GAPDH was used as internal control to test the good quality of all the cDNAs used in the experiments (not shown, figure available upon request).

ELSEVIER

Neurobiology of Aging 32 (2011) 1994–2005

NEUROBIOLOGY
OF
AGING

www.elsevier.com/locate/neuaging

Mutational screening and zebrafish functional analysis of *GIGYF2* as a Parkinson-disease gene

Ilaria Guella[a,1], Anna Pistocchi[b,1], Rosanna Asselta[a], Valeria Rimoldi[a], Anna Ghilardi[b], Francesca Sironi[c,d], Luca Trotta[c,d], Paola Primignani[c], Michela Zini[d], Anna Zecchinelli[d], Domenico Coviello[c], Gianni Pezzoli[d], Luca Del Giacco[b,**], Stefano Duga[a,*], Stefano Goldwurm[d]

[a] *Dipartimento di Biologia e Genetica per le Scienze Mediche, Università degli Studi di Milano, Milan, Italy*
[b] *Dipartimento di Biologia, Università degli Studi di Milano, Milan, Italy*
[c] *Medical Genetics Laboratory, Foundation IRCCS "Ospedale Maggiore Policlinico, Mangiagalli e Regina Elena", Milan, Italy*
[d] *Parkinson Institute, Istituti Clinici di Perfezionamento, Milan, Italy*

Received 1 July 2009; received in revised form 20 December 2009; accepted 21 December 2009
Available online 8 January 2010

Abstract

The Grb10-Interacting GYF Protein-2 (*GIGYF2*) gene has been proposed as the Parkinson-disease (PD) gene underlying the *PARK11* locus. However, association of *GIGYF2* with PD has been challenged and a functional validation of *GIGYF2* mutations is lacking.

In this frame, we performed a mutational screening of *GIGYF2* in an Italian PD cohort. Exons containing known mutations were analyzed in 552 cases and 552 controls. Thereafter, a subset of 184 familial PD cases and controls were subjected to a full coding-exon screening. These analyses identified 8 missense variations in 9 individuals (4 cases, 5 controls).

Furthermore, we developed a zebrafish model of *gigyf2* deficiency. Abrogation of *gigyf2* function in zebrafish embryos did not lead to a drastic cell loss in diencephalic dopaminergic (DA) neuron clusters, suggesting that *gigyf2* is not required for DA neuron differentiation. Notably, *gigyf2* functional abrogation did not increase diencephalic DA neurons susceptibility to the PD-inducing drug MPP+.

These data, together with those recently reported by other groups, suggest that *GIGYF2* is unlikely to be the *PARK11* gene.

Keywords: Parkinson disease; *PARK11*; *GIGYF2*; Mutational screening; Zebrafish; Morpholino oligonucleotide; MPP+

1. Introduction

Parkinson disease (PD) is a neurodegenerative disorder characterized by the selective and progressive loss of dopaminergic (DA) neurons in the substantia nigra (SN) (Olanow et al., 2009). Although only 5–10% of patients have a monogenic form of PD, several loci (*PARK1–PARK15*) responsible for rare forms of autosomal dominant or recessive PD (Lesage and Brice, 2009) were identified, leading, in at least 5 cases, to the discovery of the causative gene (*SNCA*, *parkin*, *PINK1*, *DJ1*, *LRRK2*) (Bonifati et al., 2003; Kitada et al., 1998; Paisán-Ruíz et al., 2004; Polymeropoulos et al., 1997; Valente et al., 2004).

The *PARK11* locus (2q36-37) was initially identified by a whole-genome linkage analysis in familial PD patients (Pankratz et al., 2002, 2003a,b). This result was not replicated in a different PD population (Prestel et al., 2005), however, the same region was confirmed by a genome-wide association study (Maraganore et al., 2005). In addition, a region overlapping the *PARK11* locus was linked to a familial form of Dementia with Lewy Bodies (Bogaerts et al., 2007).

---

[*] Corresponding author at: Department of Biology and Genetics for Medical Sciences, Medical Faculty, University of Milan, Via Viotti 3/5, 20133 Milan, Italy. Tel.: +39 02 503 15842; fax: +39 02 503 15864.

[**] Corresponding author at: Department of Biology, Division of Zoology and Cytology, University of Milan, Via Celoria 26, 20133 Milan, Italy. Tel.: +39 02 503 14789; fax: +39 02 503 14781.

E-mail addresses: luca.delgiacco@unimi.it (L. Del Giacco), stefano.duga@unimi.it (S. Duga).

[1] These authors contributed equally to the work.

0197-4580/$ – see front matter © 2009 Elsevier Inc. All rights reserved.
doi:10.1016/j.neurobiolaging.2009.12.016

Recently, *GIGYF2* (Grb10-Interacting GYF Protein-2) was proposed as the *PARK11* PD-susceptibility gene (Lautier et al., 2008). Sequence analysis of the gene (Lautier et al., 2008) revealed 7 different genetic variants in 12 of 249 unrelated familial PD patients from Italy and France; the same mutations were absent in 227 controls.

Although *GIGYF2* represents a good candidate for PD, given its potential involvement in insulin and insulin-like growth factor (IGF) signaling (Dufresne and Smith, 2005), several further studies did not confirm its association with PD (Bras et al., 2009; Di Fonzo et al., 2009; Guo et al., 2009; Meeus et al., 2009; Nichols et al., 2009; Sutherland et al., 2009; Tan et al., 2009; Vilariño-Güell et al., 2009; Zimprich et al., 2009). Moreover, a functional validation of *GIGYF2* mutations is still lacking, mainly because of the toxicity of the recombinant protein in eukaryotic cells (Giovannone et al., 2003), and the gene function is unknown.

Besides conventional cellular and animal models, zebrafish is emerging as a new promising system for studying human neurodegenerative diseases as well as movement disorders (Anichtchik et al., 2008; Bai et al., 2006; Bretaud et al., 2007; Flinn et al., 2008, 2009; Panula et al., 2006). Indeed, the zebrafish DA neuron system has been extensively characterized, showing that zebrafish ventral diencephalic DA neurons are functionally homologous to the mammalian ones in the SN (Rink and Wullimann, 2001). Moreover, orthologs of most human genes have been found in the zebrafish genome, including candidates for PD (Anichtchik et al., 2008; Bai et al., 2006; Bretaud et al., 2007; Flinn et al., 2009).

In this work, we chose to evaluate the role of *GIGYF2* in PD pathogenesis by a combined approach: (1) mutational screening of the gene in an Italian population comprising 238 familial and 314 sporadic PD patients (selected by the same institute that collected the cohort analyzed by Lautier et al., 2008), and an equal number of controls and (2) functional in vivo analysis of the *GIGYF2* ortholog in zebrafish.

2. Materials and methods

2.1. Subjects

We studied 552 subjects with a diagnosis of PD and an equal number of controls who had contributed samples to the DNA Bank of the Parkinson Institute, Istituti Clinici di Perfezionamento, Milan, Italy ("Human genetic bank of patients affected by Parkinson disease and parkinsonisms"; http://www.parkinson.it/dnabank.html).

The clinical diagnosis of PD was established according to the UK Parkinson Disease Society Brain Bank criteria (Hughes et al., 1992, 2001). The diagnosis of PD required the presence of bradykinesia and at least one of the following: resting tremor, rigidity or postural instability; a positive response to dopaminergic therapy; absence of atypical features or other causes of parkinsonism.

Among the 552 PD patients, 318 were male (57.6%), the mean age at onset was 55.2 years (range 14–81; SD ± 11.42), and the mean disease duration was 11.08 years (range 3–41; SD ± 6.37). Two hundred and thirty-eight patients were classified as "familial" having at least one relative among their 1st (142) or 2nd (96) degree family members with a formal diagnosis of PD. The remaining subjects were classified as "sporadic" and were selected consecutively from the DNA Bank. The age at which the patient noticed the first PD symptom was considered to be the age at onset of disease. Presence of the *LRRK2*-G2019S missense substitution was analyzed in all subjects, and 7 patients were carriers of the mutation (Goldwurm et al., 2006). The *parkin* gene was analyzed in all 62 PD patients with onset before or equal to the age of 40 (Sironi et al., 2008). Three patients were found to carry 2 mutations (in the homozygous or compound heterozygous state). These *LRRK2* or *parkin* mutation carriers were not excluded from this study.

With the exception of 4 patients, originating from 3 different countries (2 from Argentina, 1 from Albania, and 1 from Greece), all the affected subjects were Caucasian and of Italian origin.

Controls, unrelated to the patients, were recruited among spouses and care-givers. Among the 552 controls, 178 were males (32.2%), the mean age at withdrawal was 63 years (range 30–84 years, SD ± 10). All controls denied any family history for movement disorders.

The study was approved by the local Ethics Committee. Each participant signed an informed consent prior to participation to the study.

2.2. *GIGYF2* mutation analysis

Mutational screening of the *GIGYF2* isoform b (GenBank accession number NM_015575.3) coding region (exons 5–31) was performed by a combination of high-resolution melting (HRM) analysis (exons 6, 7, 9–13, 15, 18, 20–23, 25, 28, 30, and 31) and direct DNA sequencing (exons 5, 8, 14, 16, 17, 19, 24, 26, 27, and 29).

Genomic DNA extraction was performed from peripheral blood using a semi-automatic extractor (QuickGeneDNA Whole Blood Kit; FUJIFILM Europe GmbH Life Science, Düsseldorf, Germany). DNA samples were quantified spectrophotometrically using a BioPhotometer (Eppendor AG, Hamburg, Germany), standardized for concentration (40 ng/μl for the source, 5 ng/μl for the working dilution) and arrayed into 96-deep-well plates.

Suitable PCR primer couples were designed on the basis of the known genomic sequence of the gene (GenBank accession number NT_005403.16.1) to amplify all exons of interest and their exon–intron boundaries.

For HRM reactions, 7.5 ng of genomic DNA was amplified in a final volume of 10 μl. Reactions were performed in 384-well LightCycler 480 plates (Roche Applied Science, Indianapolis, IN, USA) using the LightCycler 480 HRM Master Mix (Roche). PCR cycling and HRM analysis were performed on a LightCycler 480 (Roche). Amplicons were analyzed with the Gene Scanning Software (Roche). The sensitivity and specificity of heterozygous single-base change detection were tested by screening an amplicon (exon 16) containing the known single nucleotide polymorphism (SNP) rs2305138 with both HRM and direct sequencing. All heterozygous individuals found by DNA sequencing were correctly identified also by HRM analysis, confirming the extremely high sensitivity and specificity of this technique (Taylor, 2009).

For DNA sequencing, PCRs were performed on 10–20 ng of genomic DNA in a 25-μl final volume using the FastStart *Taq* DNA Polymerase (Roche), and following the manufacturer's instructions. Direct sequencing of PCR products, purified by means of MultiScreen $PCR_{\mu 96}$ filter plates (Millipore, Bedford, MA, USA), was performed by the fluorescent dideoxy terminator method (BigDye Terminator Cycle Sequencing Ready Reaction Kit v1.1; Applied Biosystems, Foster City, CA, USA). All reactions were performed using the Mastercycler EPgradient (Eppendorf AG). Sequencing reactions were purified by the Sequencing Reaction Cleanup Kit Montage SEQ_{96} (Millipore), and analyzed by using an ABI-3130XL Genetic Analyzer (Applied Biosystems). The Variant Reporter software was used for mutation detection (Applied Biosystems).

Primer sequences, as well as the specific PCR conditions for each primer couple are available on request. Numbering of mutations is according to cDNA position (GenBank accession number NM_015575.3), starting from the first nucleotide of the ATG start codon.

2.3. Animals

Breeding wild-type fish of the AB strain were maintained at 28 °C on a 14 h light/10 h dark cycle. Embryos were collected by natural spawning, staged according to Kimmel et al. (1995), and raised at 28 °C in fish water (Instant Ocean, 0.1% Methylene Blue) in Petri dishes. Embryonic ages are expressed in somites (s), and hours post fertilization (hpf).

2.4. Zebrafish gigyf2 identification and cDNA cloning

The zebrafish chromosome 2 region spanning the *gigyf2* gene was identified through in silico search of the ENSEMBL zebrafish assembly version 8 (Zv8) using the human GIGYF2 amino-acid sequence as a bait. Based on this sequence, 3 gene-specific primers (gigyf2_ATGff: 5′-CAGCACTGTCAGTAAAAGCA, gigy2_ATGff1: 5′-GAGACTTTCAAGGAAAATGGCG, and gigy2_TGArr: 5′-AAGATCAGCAGCTCTCAAAAGTC) covering the presumptive start and stop codon regions were designed and used to amplify the *gigyf2* cDNA starting from reverse-transcribed total RNA purified from 24 hpf embryos. Reaction products were analyzed by agarose-gel electrophoresis and sequenced.

2.5. Injections

Injections were carried out on 1- to 2-cell stage embryos; the dye tracer rhodamine dextran was also coinjected. To repress *gigyf2* mRNA translation, an ATG-targeting morpholino (MO) was synthesized (Gene Tools, LLC, Philomath, OR, USA): 5′-AGTGTCTGGGTTTCCGCCATTTTCC-3′. The *gigyf2* MO was used at the concentration of 2 ng/embryo and 1.2 ng/embryo in 1 × Danieau buffer (pH 7.6) (Nasevicius and Ekker, 2000). A standard MO oligonucleotide (ctrl MO), designed against human β-thalassemia, was used as injection control. Double gigyf2 MO/gigyf2 mRNA injection was performed with 2 ng of MO and 300 pg of synthetic mRNA per embryo.

2.6. MPP+ (1-methyl-4-phenylpyridinium) exposure

Ctrl MO-injected and *gigyf2* morphant embryos were raised for 24 hpf. At this stage, embryos were manually decorionated and transferred to six-well plates (20 fish per well) for toxin treatment. Embryos were exposed to a solution containing 1 mM MPP+ (Sigma, Poole, UK) and harvested at 48 and 72 hpf for anti-Tyrosine Hydroxylase (anti-TH)-immunohistochemistry. Control embryos received no toxin. All experiments were carried out in triplicate.

2.7. In situ hybridization and immunohistochemistry

Whole-mount in situ hybridization (WISH), was carried out as described (Thisse et al., 1993) on embryos fixed for 2 h in 4% paraformaldehyde (PFA)/phosphate buffered saline (PBS), then rinsed with PBS-Tween, dehydrated in 100% methanol and stored at −20 °C until processing for WISH (Jowett and Lettice, 1994). A 724-bp *gigyf2* fragment obtained by RT-PCR using gyg2_FF (5′-TCTCACTTAAGGTGAGGGC) and gyg2_RR (5′-GTGATTGGAAGAGCTGATGG) primers was cloned into the pGemT-Easy vector (Promega, WI, USA). The recombinant plasmid was linearized by digestion and in vitro transcribed by T7 and SP6 RNA polymerases for sense and antisense RNA probe synthesis, respectively, in presence of digoxigenin-modified nucleotides (Roche). For immunohistochemistry, embryos were exposed to rabbit anti-TH (Chemicon, Temecula, CA, USA), then treated with a biotinylated secondary antibody (Vector Laboratories, Burlingame, CA, USA). Digital images of all embryos were captured using a digital camera (Leica, Heerbrugg, Switzerland).

3. Results

3.1. Mutational screening

In order to investigate the frequency of *GIGYF2* genetic variants in familial and sporadic PD cases, a mutational screening of the gene was performed, using a combination of HRM analysis and direct DNA sequencing. Among the 27 analyzed exons, 17 were selected to be pre-screened by HRM on the basis of the length, presence of known polymorphisms, and sequence characteristics. Samples with aberrant melting profiles were then sequenced to identify the underlying variant.

The study was designed to include 2 phases: in "phase I", exons containing previously reported mutations (i.e. exons 6, 8, 12, 13, 15, 18, and 30) were analyzed in 552 cases (238 familial and 314 sporadic patients), and 552 unrelated controls. In "phase II", a subset of 184 familial PD cases and an equal number of controls were subjected to a full screening of all 27 coding exons.

After completion of phase I, only 2 of the 7 described mutations (Lautier et al., 2008) were found, one (N56S, the most frequently identified across published studies) in a control individual, and the other (N457T) both in a patient and in a healthy subject. Moreover, 2 novel nucleotide variations leading to amino-acid substitutions were found: S273C and D349E, in 2 PD patients.

After completion of phase II, 3 novel genetic variants were identified: the A560V and the A1131V substitutions in 2 control subjects, and the L1209P variation in a PD patient. In addition, the H1171R variant, found by Lautier et al. (2008) in a control individual, was detected in a healthy subject.

Summarizing, this screening identified 8 different missense variations in a total of 9 individuals (4 PD patients and 5 controls) (Table 1).

In addition, 16 synonymous substitutions were found, including 9 described polymorphisms present in dbSNP (Table 2). Moreover, the *GIGYF2* exon 29 screening revealed several insertion/deletion polymorphisms. A total of 7 different alleles were found, confirming the highly polymorphic nature of this exon (Table 2).

3.2. Clinical and family studies

The 4 patients (3 females and 1 male) with a missense variation in *GIGYF2* had a typical idiopathic PD. Clinical features are reported in Table 1. Average age of onset was 55 years and all patients responded to levodopa and developed dyskinesia and/or motor fluctuations as the disease progressed. The 5 control carriers of a *GIGYF2* missense variant were mostly females (4 females and 1 male) and well over the mean age at onset for PD (70 years on average; range: 67–73).

Segregation analysis of the identified missense variations was possible only in 2 kindreds: in patient PD1529's family the affected relative (brother) was heterozygous for the S273C mutation, whereas in patient PD274's family the proband's cousin with PD was wild type for the corresponding mutation (N457T) (Fig. 1).

In addition, we were able to test the affected sister of a proband heterozygous for the V1242I mutation, belonging to the PD cohort analyzed by Lautier et al. (2008) (reported with code 848-Z-0079 in the original paper). The proband's sister did not carry the missense variant.

3.3. Identification of zebrafish gigyf2

Blast analysis of the ENSEMBL zebrafish assembly version 8 (Zv8) using the human gigyf2 protein sequence returned 3 positive hits on chromosomes 2, 7, and 10, respectively. The first one corresponds to the *gigyf2* gene (chromosome 2: nucleotide position 48,388,168-48,440,688), the other 2 represent different orthologs of the mammalian *GIGYF1*, the *GIGYF2* paralog. The 4008 base-long *gigyf2* open reading frame (ORF) encodes a putative protein of 1335 amino acids, which shows 58% of identity to the human protein. The ORF was amplified by RT-PCR using forward and reverse primers spanning the regions of the presumptive start and stop codons.

Comparative genomic analysis revealed a conserved synteny between the chromosome regions hosting human and zebrafish *GIGYF2* (Supplementary Fig. S1).

3.4. Spatio-temporal expression of gigyf2 during embryogenesis

The spatial and temporal distribution of *gigyf2* transcripts was examined by WISH, with digoxigenin-UTP-labeled probes (Thisse et al., 1993). The zebrafish *gigyf2* transcripts were detected starting from the 1-cell stage (data not shown), prior to the onset of zygotic expression (which starts between 2.3 and 5.3 hpf) and are therefore maternally deposited. From blastula until gastrula stages, *gigyf2* mRNA was strongly detected throughout the blastoderm (Fig. 2A–C). At 28 hpf, a marked *gigyf2* expression in the already defined central nervous system (CNS) was detected, whereas a weaker expression was found in the somites (Fig. 2D). At later stages of development (48 hpf), *gigyf2* expression persisted in well-defined structures of the CNS as the diencephalon, the mesencephalon, the cerebellum, and the rhombencephalon (Fig. 2E), and remained detectable in the somites. The additional labeling in the notochord (Fig. 2D) may be due to the extended incubation times with the NBT/BCIP chromogenic substrate (more than 48 h) required to develop the specific signal. Indeed, the staining also appears in the control experiment with the sense probe (data not shown).

The early uniformity in expression and subsequent specific localization of *gigyf2* transcript in neuronal tissues is consistent with a possible role of the gene in the development of the CNS.

3.5. gigyf2-loss-of-function in zebrafish embryos

In order to determine whether *gigyf2* is required for the proper development of diencephalic DA neurons in zebrafish, the protein level was knocked down by injecting a specific *gigyf2* ATG-targeted MO antisense oligonucleotide. In all the experiments, *gigyf2* MO-injected embryos were compared to embryos at the same developmental stage injected with a control MO. The phenotypes observed in *gigyf2* MO-injected embryos were categorized into 3 distinct classes: mild, inter-

Table 1
Genetic and clinical characteristics of individuals carrying *GIGFY2* missense variations.

Subject	Genotype				Phenotype						
	Exon	Nt change[a]	Aa change[b]	Aa change[c]	Affection status	Sex (M/F)	Family history for PD	Age at onset (PD) or at examination (CNT) (y)	Disease duration at examination (y)	UPDRS III[d]	H&Y stage[e]
Entire coding sequence (184 + 184)											
PD1529	12	c.818C>G	p.S273C	p.S295C	PD case	F	Yes	52	9	22	2
PD274	15	c.1370A>C	p.N457T[f]	p.N478T[f]		M	Yes	60	19	34	3
PD2193	29	c.3626T>C	p.L1209P	p.L1230P		F	Yes	52	9	19	2
CNT329	6	c.167A>G	p.N56S[f]	p.N56S[f]	Control	F		69			
CNT479	17	c.1679C>T	p.A560V	p.A581V		F		67			
CNT380	28	c.3392C>T	p.A1131V	p.A1152V		M		70			
CNT351	29	c.3512A>G	p.H1171R[f]	p.H1192R[f]		F		73			
Exons containing previously reported mutations only (368 + 368)											
PD2396	13	c.1047T>A	p.D349E	p.D371E	PD case	F	No	55	10	20	2
CNT730	15	c.1370A>C	p.N457T[f]	p.N478T[f]	Control	F		70			

y = years; M = male; F = female.

[a] Numbering according to GenBank accession number NM_015575.3, starting from the first nucleotide of the ATG start codon.

[b] Numbering according to *GIGYF2* isoform b NP_056390.2.

[c] Numbering according to *GIGYF2* isoform a NP_001096617 (for comparison with Bras et al., 2009).

[d] Unified Parkinson's Disease Rating Scale (UPDRS) (Fahn and Elton, 1987).

[e] Hoehn and Yahr scale (Hoehn and Yahr, 1967).

[f] Previously reported mutations.

Table 2
GIGFY2 polymorphisms.

Exon	Nt change[a]	dbSNP name	Aa change[b]	Aa change[c]	Frequency in patients (%)	Frequency in controls (%)	P[d]	OR (95% CI)
5	c.-4A>C	rs11555646	–	–	29.3	28.7	0.86	1.03 (0.75–1.42)
6	c.129C>T		p.Y43Y	p.Y43Y	0.1	0		
6	c.162A>G		p.K54K	p.K54K	0.1	0.1		
IVS12	IVS12+98insG	rs3217559	–	–	1.6	1.4		
12	c.906A>T		p.S302S	p.S324S	0.1	0		
15	c.1378C>A	rs2289912	p.P460T	p.P482T	2.6	2.8		
15	c.1419T>A		p.P473P	p.P494P	0	0.1		
16	c.1554G>A	rs2305138	p.E518E	p.E539E	5.2	4.3	0.36	1.20 (0.61–2.38)
17	c.1716G>T		p.A572A	p.A593A	1.5	0.5		
25	c.2898G>T		p.S945S	p.S966S	0	0.3		
26	c.2940A>G	rs3816334	p.Q980Q	p.Q1001Q	68.1	71.3	0.34	1.16 (0.85–1.60)
29	c.3629_3631delACA	rs10555297	p.Q1211del	p.Q1232del	61.5	64.6	0.39	1.14 (0.85–1.54)
29	c.3630A>G	rs7563724	p.P1210P	p.P1231P	0.3	0.3		
29	c.3651G>A	rs12328151	p.L1217P	p.L1238P	22.4	23.9	0.63	0.92 (0.65–1.30)
29	c.3963_3983del21		p.L1209_Q1215del	p.L1230_Q1236del	7.1	6	0.65	1.19 (0.66–2.11)
29	c.3984_3985insGCAGCA		p.Q1216_P1217insQQ	p.Q1237_1238insQQ	2.1	3.3		
29	c.4010_4021del12		p.P1225_Q1228del	p.P1246_Q1249del	0.5	0.9		
29	c.4009_4021del13		p.P1225TfsX5	p.P1246TfsX5	0.3	0		
29	c.3973_3996del24		p.Q1213_Q1220del	p.Q1234_Q1241del	0.3	0		
29	c.3984_3985insACA		p.Q1216_P1217insQ	p.Q1237_1238insQ	0.3	0		
31	c.3855G>A	rs34424361	p.S1285S	p.S1306S	0.55	0.86		

OR = Odds Ratio; CI = Confidence Interval.

[a] Numbering according to GenBank accession number NM_015575.3, starting from the first nucleotide of the ATG start codon.

[b] Numbering according to *GIGYF2* isoform b NP_056390.2.

[c] Numbering according to *GIGYF2* isoform a NP_001096617 (for comparison with Bras et al., 2009).

[d] Allelic association of SNPs with a minor allele frequency greater than 5% was calculated using the Fisher's exact test (right-tailed).

mediate, and severe (Fig. 3). The mild phenotype (class 1), consisted of embryos displaying a twist in the terminal part of the tail (Fig. 3B). The intermediate phenotype (class 2), presented embryos with defects in the head and eye structures, encephalic edema, U-shaped somites, and a more twisted tail (Fig. 3C). The severe phenotype (class 3) consisted of embryos with a disrupted body pattern, extensive reduction in the overall body size, and more severe defects in the head region (Fig. 3D). Such a global effect on zebrafish development might complicate distinguishment of the primary consequences of *gigyf2* depletion on DA neurons development and maintenance from secondary effects. To address

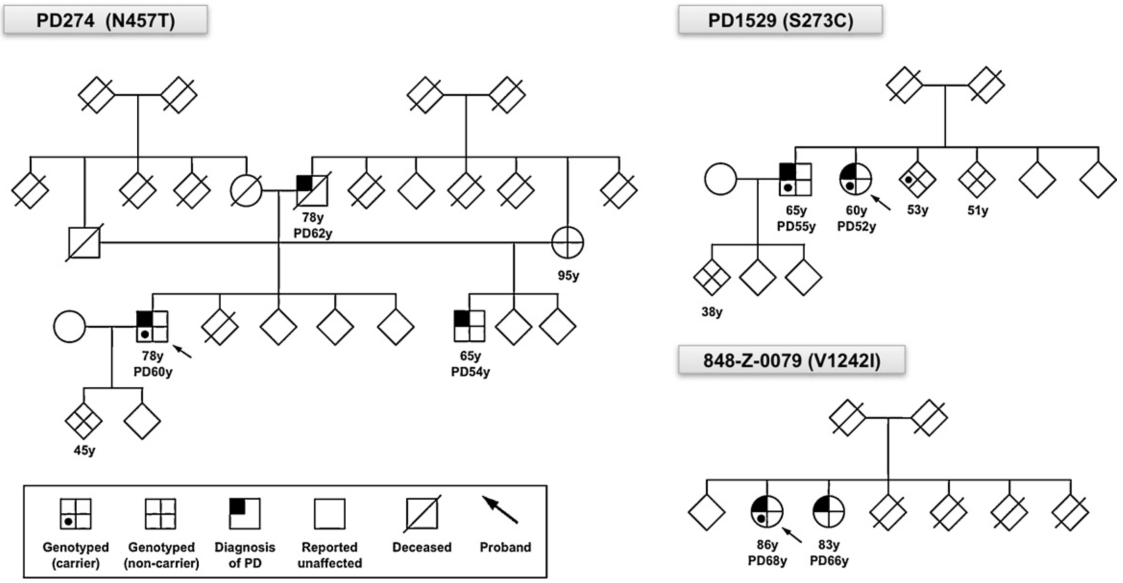

Fig. 1. Segregation of *GIGYF2* variants in pedigrees. The *GIGYF2* variant identified in each family is indicated above the pedigree. Numbers under family member symbols correspond to the best available estimate of current age or the age at death based on information provided by the index cases. Age of onset is the number adjacent to PD. To maintain the anonymity of the pedigree, the gender of non-affected subjects has not been reported.

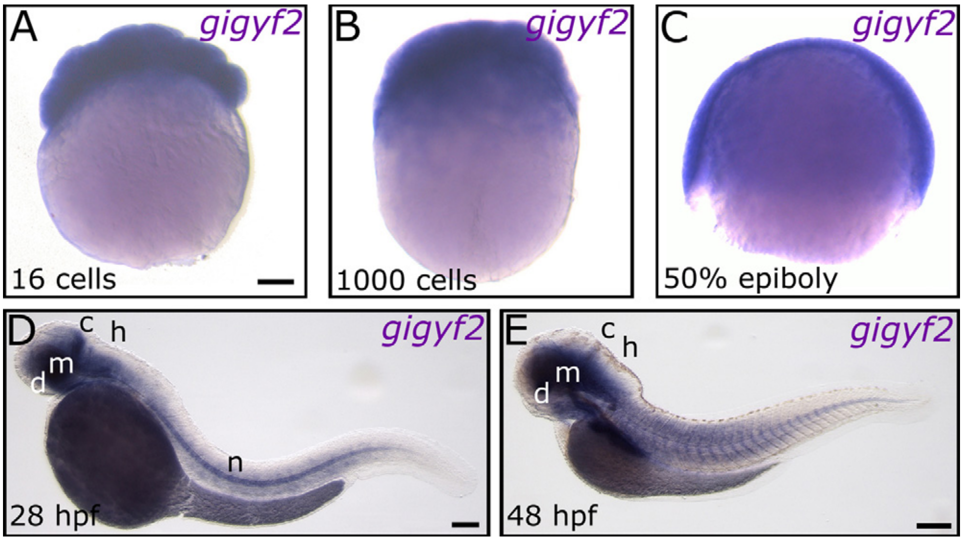

Fig. 2. *gigyf2* spatio-temporal expression pattern analyzed by whole-mount in situ hybridization (WISH). (A and B) *gigyf2* transcript was detected during blastula and (C) gastrula stages throughout the blastoderm. (D and E) At 28 and 48 hpf, *gigyf2* is expressed in the diencephalon (d), the mesencephalon (m), the cerebellum (c), the hindbrain (h), and the somites (s). The labeling in the notochord (n) also appears in the control experiment with the sense probe and may be due to the extended incubation times. Scale bars represent 100 µm.

this issue, a lower *gigyf2* MO dose (1.2 ng/embryo) was used. The lower dose produced milder effects in comparison to the higher one (2 ng/embryo), indicating a dose response to the *gigyf2* MO. Indeed, embryos injected with the lowest MO concentration had a higher frequency of class 1 phenotype (70%, $n = 100$), where the general architecture of the body axis was comparable to controls, as shown by the expression of the neural tube marker *sonic hedgehog* (*shh*) (see Supplementary Fig. S2). Only a minor fraction of the injected embryos showed more severe phenotypes. Therefore, further experiments were performed using the lower dose, except where indicated.

Since PD is characterized by a progressive loss of TH-positive DA neurons, we examined the expression of this marker in *gigyf2* MO embryos by immunohistochemistry. Abrogation of *gigyf2* did not lead to a significant loss of DA neurons in the diencephalic region of 36 and 72 hpf embryos (Fig. 4A–D). To further corroborate these data, we also analyzed the expression of *otp1* and *prox1*, two genes that were previously shown to be involved in the specification and differentiation of zebrafish DA diencephalic neurons in the posterior tuberculum (PT) and in the hypothalamus (Del Giacco et al., 2006, 2008; Pistocchi et al., 2008). *gigyf2* MO did not determine noteworthy changes either in *otp1* or in *prox1* expression patterns (Fig. 4E–H), confirming the lack of influence of *gigyf2* on diencephalic DA neurons development. The same results were obtained by using the higher dose of MO (data not shown).

In order to address whether *gigyf2* is involved in the gastrulation and/or neurulation processes, we analyzed the

Fig. 3. Phenotypical analysis of *gigyf2*-loss-of-function embryos. (A) 48 hpf-control-injected embryos (ctrl MO) compared to the (B, C, and D) *gigyf2* morphants at the same developmental stage. The phenotypes obtained after the injection of 1.2 ng of *gigyf2* MO per embryo were categorized into 3 classes: (B) mild (long-tail twisted in the terminal part), (C) intermediate (short-tail, head and eye defects, edemas, and U-shaped somites), and (D) severe (disrupted body pattern, extensive reduction in the overall body size, severe defects in the head region). Scale bar represents 200 µm.

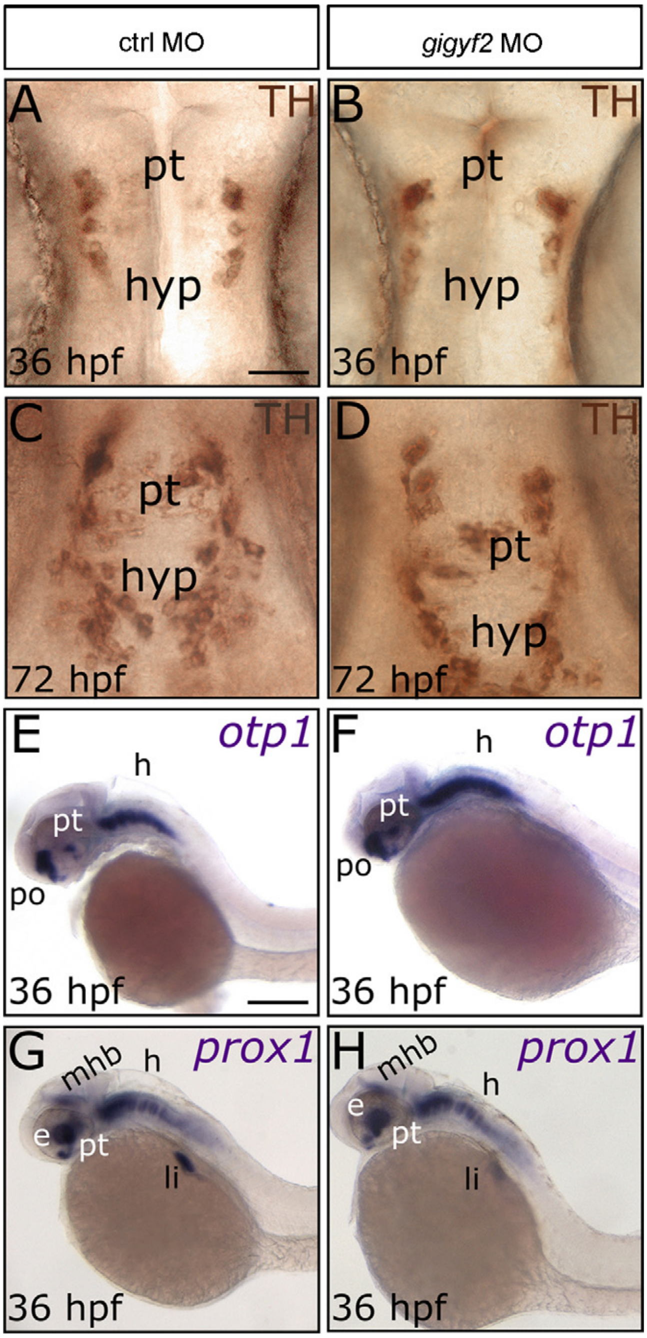

Fig. 4. *gigyf2* is not required for diencephalic DA neurons development and maintenance. (A, B, C, and D) Ventral view, anterior to the top. (E, F, G, and H) Lateral view, anterior is left and dorsal is up. (B and D) Microinjection of *gigyf2* MO does not affect the number of DA neurons, labeled with the TH antibody, in the posterior tuberculum and hypothalamus in comparison to (A and C) ctrl MO-injected embryos at 36 and 72 hpf. (E and F) *otp1* and (G and H) *prox1 w*hole-mount in situ hybridization in control- and *gigyf2* MO-injected embryos at 36 hpf. Abrogation of *gigyf2* does not modify the expression patterns of *otp1* and *prox1*. The following abbreviations are used: posterior tuberculum (pt), hypothalamus (hyp), hindbrain (h), preoptic area (po), midbrain-hindbrain boundary (mhb), eye (e), liver (li). Scale bars represent 20 μm (A) or 100 μm (E).

expression pattern of 2 markers of these critical developmental stages: *goosecoid* (*gsc*), essential to establish the body plan and for the development of the forebrain (Thisse et al., 1994), and *otx2*, important in the early specification of the neuroectoderm (Mori et al., 1994; Simeone, 1998). The expression domains of *otx2* were comparable between controls and *gigyf2* morphants (data not shown), suggesting that *gigyf2* is not involved in the correct specification of the neuroectoderm. Interestingly, about 10% ($n = 50$) of *gigyf2* MO-injected embryos presented an enlarged *gsc* expression domain at the shield stage (see Supplementary Fig. S3), suggestive of a requirement for *gigyf2* function during gastrulation. This percentage might represent the small fraction developing into the most severely affected embryos (classes 2 and 3) reported above.

To demonstrate that embryo alterations were specifically caused by the MO-induced abrogation of *gigyf2* function, we performed a rescue experiment by coinjecting embryos with the *gigyf2* MO and a synthetic full-length *gigyf2* mRNA. In order to avoid complementarity, the injected *gigyf2* mRNA was transcribed from a cDNA previously mutagenized in the MO's recognition site; 80% of the embryos rescued the normal phenotype (data not shown).

3.6. gigyf2 knockdown does not lead to increased sensitivity to MPP+

Previous studies revealed that the PD-inducing neurotoxins, such as MPP+, can efficiently reduce the number of DA neurons also in zebrafish (Bretaud et al., 2004; Sallinen et al., 2009). In addition, MPP+ has been successfully applied to demonstrate that the knockdown of the zebrafish PD-genes enhances the susceptibility to neurotoxins (Anichtchik et al., 2008; Flinn et al., 2009). To evaluate the possibility that reduced levels of the gigyf2 protein might increase the sensitivity to toxin insults, we exposed *gigyf2*-knockdown and control embryos to MPP+. We did not observe any significant difference in the reduction of the number of DA neurons at 48 (data not shown) and 72 hpf (Fig. 5) after exposure to the neurotoxin, indicating that *gigyf2* functional abrogation does not increase the susceptibility of the DA diencephalic neurons to MPP+.

4. Discussion

After the nomination of *GIGYF2* as the PD-gene underlying the *PARK11* locus, several studies quickly followed in the literature (Bras et al., 2009; Di Fonzo et al., 2009; Guo et al., 2009; Meeus et al., 2009; Nichols et al., 2009; Sutherland et al., 2009; Tan et al., 2009; Vilariño-Güell et al., 2009; Zimprich et al., 2009), invariantly challenging the original positive findings of Lautier et al. (2008). Unfortunately, the majority of these replication studies focused on sporadic PD patients, notwithstanding the fact that both the *PARK11* locus and the *GIGYF2* gene were pointed out by

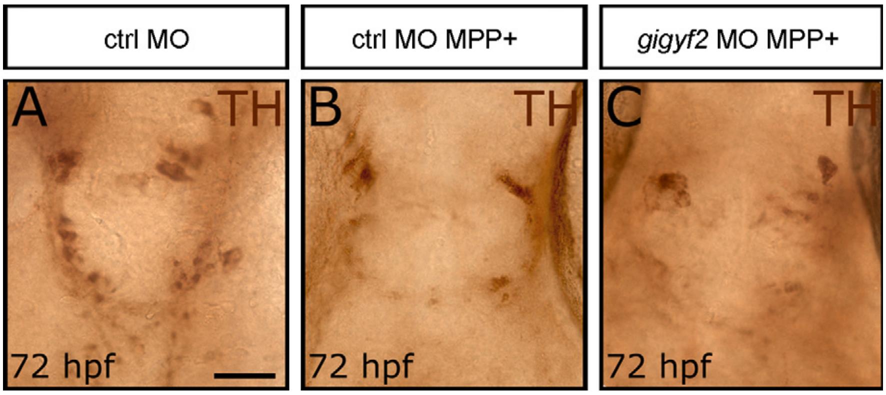

Fig. 5. *gigyf2* knockdown does not lead to increased sensitivity to MPP+ in zebrafish larvae. Ventral view, anterior to the top in all panels. TH immunohistochemistry revealed that DA neurons of the ventral diencephalon are reduced following MPP+ treatment in comparison to untreated embryos at the same developmental stage (compare A, MPP+-untreated, to B and C, MPP+-treated embryos). The MPP+-induced loss of DA neurons is not increased following *gigyf2* MO injection (compare B to C). Scale bar represents 20 μm.

studying familial PD. Even the work by Nichols et al. (2009), although describing a full-exon screening in 96 probands belonging to the original series of families that generated the linkage to *PARK11*, did not allow an unbiased comparison of the frequency of missense mutations in cases vs. controls, because of the lack of data on healthy subjects. Therefore, the current genetic data arguing against the involvement of *GIGYF2* mutations in PD pathogenesis are still to be considered incomplete. Moreover, no experimental studies have been performed to explore the impact of the identified *GIGYF2* mutations at the protein level.

In this frame, we investigated the involvement of *GIGYF2* in PD pathogenesis by a comprehensive mutational screening in a relatively large Italian population of 184 familial PD patients and in an equal number of healthy controls. Moreover, exons bearing previously reported missense variants were analyzed in 368 additional patients (54 familial and 314 sporadic) and controls. Besides representing the largest *GIGYF2* replication study on familial PD, our work has the additional advantage to have been performed on a cohort of patients selected by the same clinical centre that collected the Italian cases studied in the Lautier's paper (Lautier et al., 2008).

The combination of phase I (analysis of selected exons) and phase II (full exons screening) genotyping revealed a fairly homogeneous distribution of missense variations between cases and controls (Table 3). In particular, we found 8 different missense substitutions in a total of 9 individuals (4 PD patients and 5 controls). Considering only the 184 patients with familial PD whose *GIGYF2* coding region was fully analyzed, a mutation rate inconsistent with the one reported by Lautier et al. (2008) was found (1.6% in cases and 2.2% in controls vs. 5.7 and 0.8%, respectively).

In 2 out of the 4 carrier patients' families, we were able to perform a segregation analysis of the identified missense variations; in addition, we tested the affected sister of a proband belonging to the PD cohort reported by Lautier et al. (2008). Combining our results with those already reported in the literature (Lautier et al., 2008; Nichols et al., 2009), co-segregation of *GIGYF2* missense variants has been observed in 7 out of 13 analyzed families. This is equal to what would be expected by chance.

Table 3
Meta-analysis of *GIGYF2* mutation frequencies.

Study	Population	No. of cases	No. of controls	Collective frequency of missense variants		*P*
				Cases (%)	Controls (%)	
Lautier et al.	Italian	123	131	1.62	0	0.04
	French	126	96	0.40	0	0.38
Bras et al.	Portuguese	267	451	0.75	1.66	0.14
	North American	460	460	1.09	0.43	0.11
Meeus et al.	Belgian	305	360	0.16	0	0.12
This paper	Italian	184	184	0.54	0.27	0.56
Combined analysis		1465	1682	0.68	0.59	0.19 OR 1.50, 95% CI 0.81–2.77

The meta-analysis was conducted using allele frequency data from case/control full-exon screenings reported in the literature (Bras et al., 2009; Lautier et al., 2008; Meeus et al., 2009), including the present study. Non-synonymous variations found in both cases and controls across all the studies were excluded from the meta-analysis. OR = Odds Ratio; CI = Confidence Interval.

Pulling together all genetic screenings performed so far on *GIGYF2*, a total of 44 missense variations spread on the entire gene were found. No null alleles, either resulting from nonsense, frameshift, or splicing defects were described. Limiting the analysis to case/control whole-coding-region screenings (Bras et al., 2009; Lautier et al., 2008; Meeus et al., 2009), including the present work, and excluding the 5 variations found in both cases and controls across all the studies, the collective frequency of missense substitutions was comparable between PD patients and healthy individuals (0.68% vs. 0.59%, respectively; meta-analysis OR, 1.50; 95% CI, 0.81–2.77; $P = 0.19$) (Table 3).

Considering that several obstacles hamper a classical in vitro analysis of the structural and functional consequences of *GIGYF2* missense mutations, the pathogenic impact of the identified sequence variants was investigated in silico using the PMut algorithm (Ferrer-Costa et al., 2005). The percentage of predicted deleterious mutations calculated by this software was even lower in cases (50%) compared to controls (72.7%). Despite the substantial limitations of this in silico approach, this finding adds to the evidences arguing against a role of *GIGYF2* missense variations in the pathogenesis of PD.

The most straightforward approach to explore the role of *GIGYF2* in PD, besides genetics, would be to perform functional experiments in cell lines or in vivo. Given the already mentioned difficulties in setting up a cellular model to study the function of this gene and its potential implication in neurodegeneration and DA survival, we decided to generate a vertebrate model of *GIGYF2* insufficiency in zebrafish.

Zebrafish *gigyf2* is highly homologous to the human counterpart and its genomic organization is strongly conserved, as confirmed by the synteny between the chromosome regions hosting the 2 orthologs in fish and humans. Interestingly, *gigyf2* is also expressed in the ventralmost part of the diencephalon, the region hosting the DA neurons functionally homologous to mammalian SN neurons (Rink and Wullimann, 2001). These findings prompted us to assess the potential involvement of *gigyf2* in the determination of the DA phenotype by means of gene function abrogation. The obtained results indicate that *gigyf2* is dispensable for the proper development of the DA system and its deficiency does not determine the degeneration of the already differentiated DA neurons.

As previously demonstrated in zebrafish, the knockdown of the PD candidate genes *PINK1* and *parkin* increases the susceptibility to DA neuron loss after exposure to MPP+ (Anichtchik et al., 2008; Flinn et al., 2009). Therefore, we explored the effects of MPP+ on the differentiation and maintenance of diencephalic DA neurons in *gigyf2*-dysfunctional embryos. The absence of additional DA neuronal loss in *gigyf2* morphants in a PD-inducing environment suggests that *gigyf2* alterations might not represent a genetic predisposition to DA neurons vulnerability, a finding of significance in the ascertainment of the pathogenic role of *GIGYF2* in PD onset.

Taken together, these results strengthen the conclusions of the mutational screening, which did not evidence any connection of *GIGYF2* genetic variations with PD. However, due to *gigyf2* ubiquitous expression in the CNS, we cannot exclude further roles in neurogenesis. Furthermore, zebrafish *gigyf2* functions might be crucial earlier during development, as suggested by the generalized and dramatic effects exerted by higher doses of *gigyf2* MO and by the alteration of the expression pattern of the gastrulation marker *gsc*. Interestingly, no *GIGYF2* nonsense or frameshift mutations have been identified in this work or by others in humans, supporting the hypothesis that the complete inactivation of the gene might be incompatible with embryonic development.

Conflict of interest statement

All the authors declare no actual or potential conflicts of interest.

Acknowledgments

We thank the patients and their relatives for their contributions. The financial support of the "Fondazione Grigioni per il Morbo di Parkinson" is gratefully acknowledged.

The DNA samples were from the "Human Genetic Bank of Patients Affected by Parkinson Disease and Parkinsonisms" of the Parkinson Institute, Istituti Clinici di Perfezionamento, Italy (http://www.parkinson.it/dnabank.htm). This biobank is supported by the Italian Telethon Foundation (grant no. GTB07001) and by the "Fondazione Grigioni per il Morbo di Parkinson".

Appendix A. Supplementary data

Supplementary data associated with this article can be found, in the online version, at doi:10.1016/j.neurobiolaging.2009.12.016.

References

Anichtchik, O., Diekmann, H., Fleming, A., Roach, A., Goldsmith, P., Rubinsztein, D., 2008. Loss of PINK1 function affects development and results in neurodegeneration in zebrafish. J. Neurosci. 28 (33), 8199–8207.

Bai, Q., Mullett, S., Garver, J., Hinkle, D., Burton, E., 2006. Zebrafish DJ-1 is evolutionarily conserved and expressed in dopaminergic neurons. Brain Res. 1113 (1), 33–44.

Bogaerts, V., Engelborghs, S., Kumar-Singh, S., Goossens, D., Pickut, B., van der Zee, J., Sleegers, K., Peeters, K., Martin, J., Del-Favero, J., Gasser, T., Dickson, D., Wszolek, Z., De Deyn, P., Theuns, J., Van Broeckhoven, C., 2007. A novel locus for Dementia with Lewy bodies: a clinically and genetically heterogeneous disorder. Brain 130 (Pt 9), 2277–2291.

Bonifati, V., Rizzu, P., van Baren, M., Schaap, O., Breedveld, G., Krieger, E., Dekker, M., Squitieri, F., Ibanez, P., Joosse, M., van Dongen, J., Vanacore, N., van Swieten, J., Brice, A., Meco, G., van Duijn, C., Oostra, B., Heutink, P., 2003. Mutations in the DJ-1 gene associated with autosomal recessive early-onset parkinsonism. Science 299 (5604), 256–259.

Bras, J., Simón-Sánchez, J., Federoff, M., Morgadinho, A., Januario, C., Ribeiro, M., Cunha, L., Oliveira, C., Singleton, A., 2009. Lack of replication of association between GIGYF2 variants and Parkinson disease. Hum. Mol. Genet. 18 (2), 341–346.

Bretaud, S., Allen, C., Ingham, P., Bandmann, O., 2007. p53-dependent neuronal cell death in a DJ-1-deficient zebrafish model of Parkinson's disease. J. Neurochem. 100 (6), 1626–1635.

Bretaud, S., Lee, S., Guo, S., 2004. Sensitivity of zebrafish to environmental toxins implicated in Parkinson's disease. Neurotoxicol. Teratol. 26 (6), 857–864.

Del Giacco, L., Pistocchi, A., Cotelli, F., Fortunato, A., Sordino, P., 2008. A peek inside the neurosecretory brain through orthopedia lenses. Dev. Dyn. 237 (9), 2295–2303.

Del Giacco, L., Sordino, P., Pistocchi, A., Andreakis, N., Tarallo, R., Di Benedetto, B., Cotelli, F., 2006. Differential regulation of the zebrafish orthopedia 1 gene during fate determination of diencephalic neurons. BMC Dev. Biol. 6, 50.

Di Fonzo, A., Fabrizio, E., Thomas, A., Fincati, E., Marconi, R., Tinazzi, M., Breedveld, G., Simons, E., Chien, H., Ferreira, J., Horstink, M., Abbruzzese, G., Borroni, B., Cossu, G., Libera, A., Fabbrini, G., Guidi, M., De Mari, M., Lopiano, L., Martignoni, E., Marini, P., Onofrj, M., Padovani, A., Stocchi, F., Toni, V., Sampaio, C., Barbosa, E., Meco, G., The Italian Parkinson Genetics Network, Oostra, B., Bonifati, V., 2009. GIGYF2 mutations are not a frequent cause of familial Parkinson's disease. Parkinsonism Relat. Disord.

Dufresne, A., Smith, R., 2005. The adapter protein GRB10 is an endogenous negative regulator of insulin-like growth factor signaling. Endocrinology 146 (10), 4399–4409.

Fahn, S., Elton, R.L., 1987. Unified Parkinson's Disease Rating Scale. In: Fahn, S., Marsden, C.D., Calne, D.B., Goldstein, M. (Eds.), Recent Developments in Parkinson's Disease. MacMillan Health Care Information, Florham Park.

Ferrer-Costa, C., Gelpí, J., Zamakola, L., Parraga, I., de la Cruz, X., Orozco, M., 2005. PMUT: a web-based tool for the annotation of pathological mutations on proteins. Bioinformatics 21 (14), 3176–3178.

Flinn, L., Bretaud, S., Lo, C., Ingham, P., Bandmann, O., 2008. Zebrafish as a new animal model for movement disorders. J. Neurochem. 106 (5), 1991–1997.

Flinn, L., Mortiboys, H., Volkmann, K., Köster, R., Ingham, P., Bandmann, O., 2009. Complex I deficiency and dopaminergic neuronal cell loss in parkin-deficient zebrafish (Danio rerio). Brain 132 (Pt 6), 1613–1623.

Giovannone, B., Lee, E., Laviola, L., Giorgino, F., Cleveland, K., Smith, R., 2003. Two novel proteins that are linked to insulin-like growth factor (IGF-I) receptors by the Grb10 adapter and modulate IGF-I signaling. J. Biol. Chem. 278 (34), 31564–31573.

Goldwurm, S., Zini, M., Di Fonzo, A., De Gaspari, D., Siri, C., Simons, E., van Doeselaar, M., Tesei, S., Antonini, A., Canesi, M., Zecchinelli, A., Mariani, C., Meucci, N., Sacilotto, G., Cilia, R., Isaias, I., Bonetti, A., Sironi, F., Ricca, S., Oostra, B., Bonifati, V., Pezzoli, G., 2006. *LRRK2* G2019S mutation and Parkinson's disease: a clinical, neuropsychological and neuropsychiatric study in a large Italian sample. Parkinsonism Relat. Disord. 12 (7), 410–419.

Guo, Y., Jankovic, J., Zhu, S., Le, W., Song, Z., Xie, W., Liao, D., Yang, H., Deng, H., 2009. GIGYF2 Asn56Ser and Asn457Thr mutations in Parkinson disease patients. Neurosci. Lett. 454 (3), 209–211.

Hoehn, M., Yahr, M., 1967. Parkinsonism: onset, progression and mortality. Neurology 17 (5), 427–442.

Hughes, A., Daniel, S., Kilford, L., Lees, A., 1992. Accuracy of clinical diagnosis of idiopathic Parkinson's disease: a clinico-pathological study of 100 cases. J. Neurol. Neurosurg. Psychiatry 55 (3), 181–184.

Hughes, A., Daniel, S., Lees, A., 2001. Improved accuracy of clinical diagnosis of Lewy body Parkinson's disease. Neurology 57 (8), 1497–1499.

Jowett, T., Lettice, L., 1994. Whole-mount in situ hybridizations on zebrafish embryos using a mixture of digoxigenin- and fluorescein-labelled probes. Trends Genet. 10 (3), 73–74.

Kimmel, C., Ballard, W., Kimmel, S., Ullmann, B., Schilling, T., 1995. Stages of embryonic development of the zebrafish. Dev. Dyn. 203 (3), 253–310.

Kitada, T., Asakawa, S., Hattori, N., Matsumine, H., Yamamura, Y., Minoshima, S., Yokochi, M., Mizuno, Y., Shimizu, N., 1998. Mutations in the parkin gene cause autosomal recessive juvenile parkinsonism. Nature 392 (6676), 605–608.

Lautier, C., Goldwurm, S., Dürr, A., Giovannone, B., Tsiaras, W., Pezzoli, G., Brice, A., Smith, R., 2008. Mutations in the GIGYF2 (TNRC15) gene at the PARK11 locus in familial Parkinson disease. Am. J. Hum. Genet. 82 (4), 822–833.

Lesage, S., Brice, A., 2009. Parkinson's disease: from monogenic forms to genetic susceptibility factors. Hum. Mol. Genet. 18 (R1), R48–R59.

Maraganore, D., de Andrade, M., Lesnick, T., Strain, K., Farrer, M., Rocca, W., Pant, P., Frazer, K., Cox, D., Ballinger, D., 2005. High-resolution whole-genome association study of Parkinson disease. Am. J. Hum. Genet. 77 (5), 685–693.

Meeus, B., Nuytemans, K., Crosiers, D., Engelborghs, S., Pals, P., Pickut, B., Peeters, K., Mattheijssens, M., Corsmit, E., Cras, P., De Deyn, P., Theuns, J., Van Broeckhoven, C., 2009. GIGYF2 has no major role in Parkinson genetic etiology in a Belgian population. Neurobiol. Aging, doi:10.1016/j.neurobiolaging.2009.02.016.

Mori, H., Miyazaki, Y., Morita, T., Nitta, H., Mishina, M., 1994. Different spatio-temporal expressions of three otx homeoprotein transcripts during zebrafish embryogenesis. Brain Res. Mol. Brain Res. 27 (2), 221–231.

Nasevicius, A., Ekker, S., 2000. Effective targeted gene 'knockdown' in zebrafish. Nat. Genet. 26 (2), 216–220.

Nichols, W., Kissell, D., Pankratz, N., Pauciulo, M., Elsaesser, V., Clark, K., Halter, C., Rudolph, A., Wojcieszek, J., Pfeiffer, R., Foroud, T., 2009. Variation in GIGYF2 is not associated with Parkinson disease. Neurology 72 (22), 1886–1892.

Olanow, C., Stern, M., Sethi, K., 2009. The scientific and clinical basis for the treatment of Parkinson disease (2009). Neurology 72 (21 Suppl. 4), S1–S136.

Paisán-Ruíz, C., Jain, S., Evans, E., Gilks, W., Simón, J., van der Brug, M., López de Munain, A., Aparicio, S., Gil, A., Khan, N., Johnson, J., Martinez, J., Nicholl, D., Carrera, I., Pena, A., de Silva, R., Lees, A., Martí-Massó, J., Pérez-Tur, J., Wood, N., Singleton, A., 2004. Cloning of the gene containing mutations that cause PARK8-linked Parkinson's disease. Neuron 44 (4), 595–600.

Pankratz, N., Nichols, W., Uniacke, S., Halter, C., Murrell, J., Rudolph, A., Shults, C., Conneally, P., Foroud, T., 2003a. Genome-wide linkage analysis and evidence of gene-by-gene interactions in a sample of 362 multiplex Parkinson disease families. Hum. Mol. Genet. 12 (20), 2599–2608.

Pankratz, N., Nichols, W., Uniacke, S., Halter, C., Rudolph, A., Shults, C., Conneally, P., Foroud, T., 2002. Genome screen to identify susceptibility genes for Parkinson disease in a sample without parkin mutations. Am. J. Hum. Genet. 71 (1), 124–135.

Pankratz, N., Nichols, W., Uniacke, S., Halter, C., Rudolph, A., Shults, C., Conneally, P., Foroud, T., 2003b. Significant linkage of Parkinson disease to chromosome 2q36-37. Am. J. Hum. Genet. 72 (4), 1053–1057.

Panula, P., Sallinen, V., Sundvik, M., Kolehmainen, J., Torkko, V., Tiittula, A., Moshnyakov, M., Podlasz, P., 2006. Modulatory neurotransmitter systems and behavior: towards zebrafish models of neurodegenerative diseases. Zebrafish 3 (2), 235–247.

Pistocchi, A., Gaudenzi, G., Carra, S., Bresciani, E., Del Giacco, L., Cotelli, F., 2008. Crucial role of zebrafish prox1 in hypothalamic catecholaminergic neurons development. BMC Dev. Biol. 8, 27.

Polymeropoulos, M., Lavedan, C., Leroy, E., Ide, S., Dehejia, A., Dutra, A., Pike, B., Root, H., Rubenstein, J., Boyer, R., Stenroos, E., Chandrasekharappa, S., Athanassiadou, A., Papapetropoulos, T., Johnson, W., Lazzarini, A., Duvoisin, R., Di Iorio, G., Golbe, L., Nussbaum, R.,

1997. Mutation in the alpha-synuclein gene identified in families with Parkinson's disease. Science 276 (5321), 2045–2047.

Prestel, J., Sharma, M., Leitner, P., Zimprich, A., Vaughan, J., Dürr, A., Bonifati, V., De Michele, G., Hanagasi, H., Farrer, M., Hofer, A., Asmus, F., Volpe, G., Meco, G., Brice, A., Wood, N., Müller-Myhsok, B., Gasser, T., 2005. PARK11 is not linked with Parkinson's disease in European families. Eur. J. Hum. Genet. 13 (2), 193–197.

Rink, E., Wullimann, M., 2001. The teleostean (zebrafish) dopaminergic system ascending to the subpallium (striatum) is located in the basal diencephalon (posterior tuberculum). Brain Res. 889 (1–2), 316–330.

Sallinen, V., Torkko, V., Sundvik, M., Reenilä, I., Khrustalyov, D., Kaslin, J., Panula, P., 2009. MPTP and MPP+ target specific aminergic cell populations in larval zebrafish. J. Neurochem. 108 (3), 719–731.

Simeone, A., 1998. Otx1 and Otx2 in the development and evolution of the mammalian brain. EMBO J. 17 (23), 6790–6798.

Sironi, F., Primignani, P., Zini, M., Tunesi, S., Ruffmann, C., Ricca, S., Brambilla, T., Antonini, A., Tesei, S., Canesi, M., Zecchinelli, A., Mariani, C., Meucci, N., Sacilotto, G., Cilia, R., Isaias, I., Garavaglia, B., Ghezzi, D., Travi, M., Decarli, A., Coviello, D., Pezzoli, G., Goldwurm, S., 2008. Parkin analysis in early onset Parkinson's disease. Parkinsonism Relat. Disord. 14 (4), 326–333.

Sutherland, G., Siebert, G., Newman, J., Silburn, P., Boyle, R., O'Sullivan, J., Mellick, G., 2009. Haplotype analysis of the PARK 11 gene, GIGYF2, in sporadic Parkinson's disease. Mov. Disord. 24 (3), 449–452.

Tan, E., Lin, C., Tai, C., Tan, L., Chen, M., Li, R., Lim, H., Pavanni, R., Yuen, Y., Prakash, K., Zhao, Y., Wu, R., 2009. Non-synonymous GIGYF2 variants in Parkinson's disease from two Asian populations. Hum. Genet., doi:10.1007/s00439-009-0678-x.

Taylor, C., 2009. Mutation scanning using high-resolution melting. Biochem. Soc. Trans. 37 (Pt 2), 433–437.

Thisse, C., Thisse, B., Halpern, M., Postlethwait, J., 1994. Goosecoid expression in neurectoderm and mesendoderm is disrupted in zebrafish cyclops gastrulas. Dev. Biol. 164 (2), 420–429.

Thisse, C., Thisse, B., Schilling, T., Postlethwait, J., 1993. Structure of the zebrafish snail1 gene and its expression in wild-type, spadetail and no tail mutant embryos. Development 119 (4), 1203–1215.

Valente, E., Abou-Sleiman, P., Caputo, V., Muqit, M., Harvey, K., Gispert, S., Ali, Z., Del Turco, D., Bentivoglio, A., Healy, D., Albanese, A., Nussbaum, R., González-Maldonado, R., Deller, T., Salvi, S., Cortelli, P., Gilks, W., Latchman, D., Harvey, R., Dallapiccola, B., Auburger, G., Wood, N., 2004. Hereditary early-onset Parkinson's disease caused by mutations in PINK1. Science 304 (5674), 1158–1160.

Vilariño-Güell, C., Ross, O., Farrer, M., 2009. Reply: GIGYF2 variants are not associated with Parkinson's disease in Italy. Mov. Disord.

Zimprich, A., Schulte, C., Reinthaler, E., Haubenberger, D., Balzar, J., Lichtner, P., El Tawil, S., Edris, S., Foki, T., Pirker, W., Katzenschlager, R., Daniel, G., Brücke, T., Auff, E., Gasser, T., 2009. PARK11 gene (GIGYF2) variants Asn56Ser and Asn457Thr are not pathogenic for Parkinson's disease. Parkinsonism Relat. Disord. 15 (7), 532–534.

prox1b Activity Is Essential in Zebrafish Lymphangiogenesis

Luca Del Giacco[1]*, **Anna Pistocchi**[2], **Anna Ghilardi**[1]

1 Department of Biology, Università degli Studi di Milano, Milan, Italy, **2** Division of Regenerative Medicine, San Raffaele Scientific Institute, Milan, Italy

Abstract

Background: The lymphatic vascular system, draining interstitial fluids from most tissues and organs, exerts crucial functions in several physiological and pathological processes. Lymphatic system development depends on *Prox1*, the first marker to be expressed in the endothelial cells of the cardinal vein from where lymph vessels originate. *Prox1* ortholog in the optically clear, easily manipulated zebrafish model has been previously isolated and its contribution to lymphangiogenesis has been clarified. Because of a round of genome duplication occurred at the base of teleosts radiation, several zebrafish genes have been retained in duplicate through evolution. We investigated for the presence of additional *prox1* genes and determined their role in zebrafish lymphangiogenesis.

Methodology/Principal Findings: We isolated a second ortholog, named *prox1b*, and analyzed its expression during development by whole mount *in situ* hybridization (WISH). We detected strong *prox1b* expression in the endothelium of the posterior cardinal vein (PCV) from where lymphatic precursors originate. To analyze *prox1b* involvement in lymphangiogenesis we utilized the fli1:GFP transgenics and followed the formation of the toracic duct (TD), the primary lymph vessel in fish, after *prox1b* knockdown. Our findings clearly demonstrated that the absence of *prox1b* activity severely hampers the formation of the TD.

Conclusions/Significance: This work provides substantial progress toward the understanding of zebrafish lymphangiogenesis. In light of the features shared by the lymphatic systems of zebrafish and higher vertebrates, the establishment of such lymphatic model will provide a powerful tool to study, for instance, disorders of body fluid homeostasis, inflammation and cancer metastasis, and may ultimately contribute to novel therapies.

Citation: Del Giacco L, Pistocchi A, Ghilardi A (2010) *prox1b* Activity Is Essential in Zebrafish Lymphangiogenesis. PLoS ONE 5(10): e13170. doi:10.1371/journal.pone.0013170

Editor: Joy Sturtevant, Louisiana State University, United States of America

Received April 21, 2010; **Accepted** September 9, 2010; **Published** October 18, 2010

Funding: The study was financed by the Fondo per gli Investimenti nella Ricerca Scientifica e Tecnologica (FIRST). The funders had no role in study design, data collection and analysis, decision to publish, or preparation of the manuscript.

Competing Interests: The authors have declared that no competing interests exist.

* E-mail: luca.delgiacco@unimi.it

Introduction

The lymphatic system drains lymph away from tissues and organs back to the bloodstream, and plays a main role in the immune response and fat absorption. In addition, the lymphatic system is implicated in inflammation processes as well as cancer metastasis.

Prox1 homeogene, the vertebrate homolog of *prospero* in *D. melanogaster* [1], regulates cell proliferation, fate determination and differentiation during embryonic development, and triggers the molecular program leading to the formation of the lymphatic system. Indeed, ablation of *Prox1* in mouse, Xenopus, and zebrafish impaired the formation of lymph vessels [2,3,4,5,6,7].

About 350 million years ago, a round of genome duplication occurred at the base of teleosts radiation resulting in two copies of all genes. Some of such copies have been retained in duplicate through evolution [8]. In view of this evidence, we searched for additional *Prox1* orthologs in zebrafish. Interestingly, while we were conducting the experiments reported in this work, a paper describing the isolation and the expression patterns of two *prox1* genes in the fish medaka has been published [9].

Here, we isolated a second zebrafish ortholog, named *prox1b* (to distinguish it from the first identified one, from now on designated *prox1a*), and showed that *prox1b* knockdown impedes the formation of the toracic duct (TD), the primary fish lymph vessel [10].

Results and Discussion

prox1b cloning and gene structure

Blast analysis of the ENSEMBL zebrafish assembly version 6 (Zv6) using zebrafish *prox1a* full-length cDNA sequence returned two positive hits on chromosome 17, corresponding to the previously characterized *prox1a* [11], and *prox2* [12] genes, and one hit on chromosome 7, this last one mapping at chromosome location 19,523,485 – 19,537,485 and never reported before. The 3,558-bp mRNA sequence is identified by the GenBank accession number FJ544314 (Figure 1). The encoded protein is related to the prospero transcription factors family, being characterized by the atypical homeodomain and two prospero domains, PD1 and PD2 (Figure 1A). This protein represents the second zebrafish ortholog of Prox1, producing significant alignments (35% of identity) with all the Prox1 present in the GenBank database, including zebrafish prox1a. *prox1b* coding region is interrupted by three introns, and an additional one is located in the 5′ UTR (Figure 1A), indicating that the structure of the gene has been evolutionarily conserved from zebrafish to mammals.

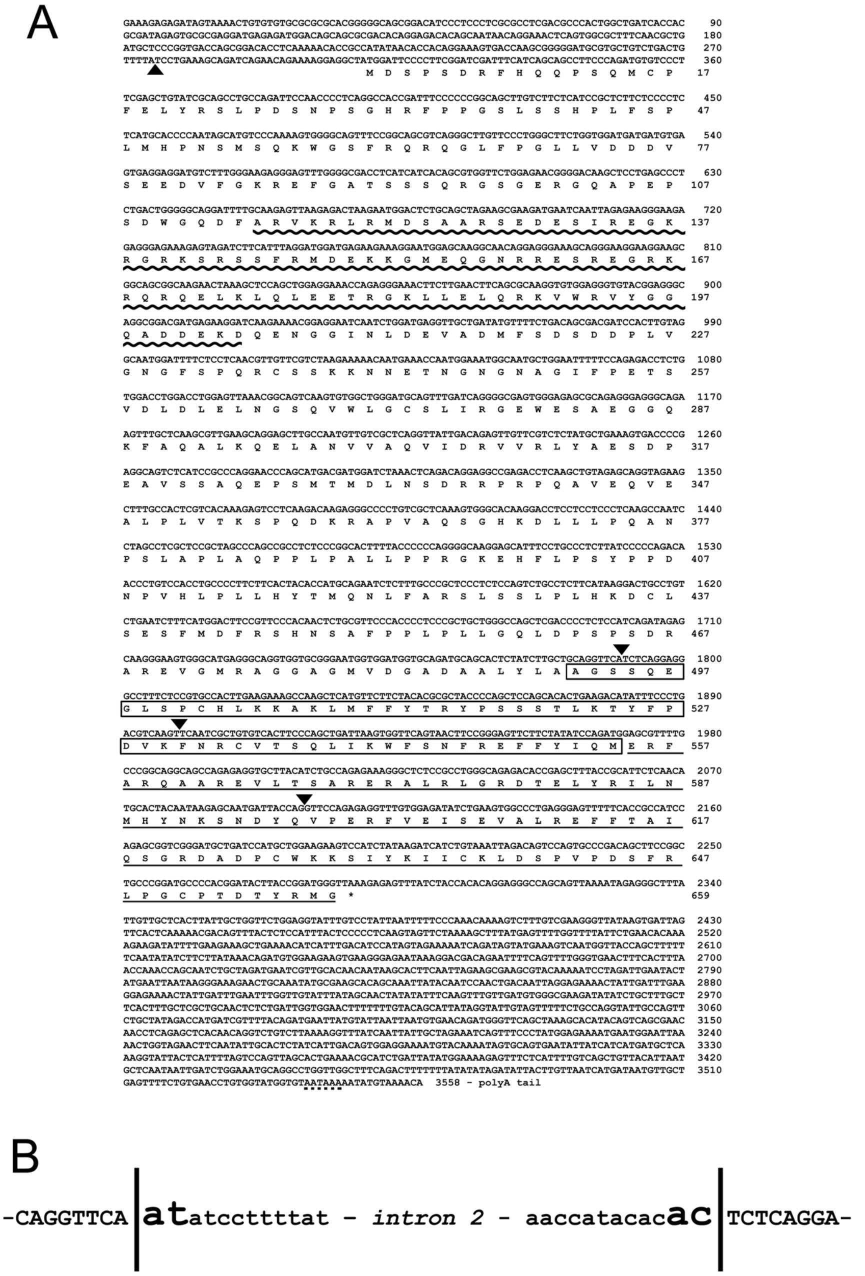

Figure 1. Nucleotide and deduced amino acid sequences of zebrafish *prox1b*. (A) arrowheads show the positions of the introns. The asterisk indicates the stop codon at the end of the open reading frame. A dotted line marks the polyadenylation site. The wave and solid lines mark PD1 and PD2, respectively. The homeodomain is boxed. The sequence has been submitted to the GenBank/EMBL database under accession number FJ544314. (B) *prox1b* contains the U12-dependent intron (intron 2), characterized by the unusual AT/AC splice sites, located at the beginning of the homeobox.
doi:10.1371/journal.pone.0013170.g001

[12,13]. However, zebrafish *prox1b* gene does not show synteny with mammalian *Prox1*, as for the recently identified medaka *prox1b* gene [9]. Analogously to all the vertebrate *Prox* genes, as well as *Drosophila prospero*, *prox1b* contains the U12-dependent intron (intron 2), characterized by the unusual AT/AC splice sites, located at the beginning of the homeobox (Figure 1B) [12,13].

Role of *prox1b* in zebrafish lymphangiogenesis

Prox1 is a master gene controlling the processes of budding, migration and proliferation of lymphangioblasts [2,3,4,5,6,7]. In zebrafish, its contribution to lymphangiogenesis has been demonstrated by means of *prox1a* knockdown [4]. In this context, we examined the possible involvement of *prox1b* in lymphangiogenesis. The first signal of gene activity appeared in the central nervous system (CNS) starting from somitogenesis (10 s stage, Figure 2A), where *prox1b* expression persists during development (Figure 2B,C,D,G) (a more detailed analysis of *prox1b* mRNA distribution in the nervous system will be discussed elsewhere). Interestingly, at 48 hours post-fertilization (hpf), we detected intense *prox1b* staining at the level of the posterior cardinal vein (PCV) and of the sprouts emanating from this

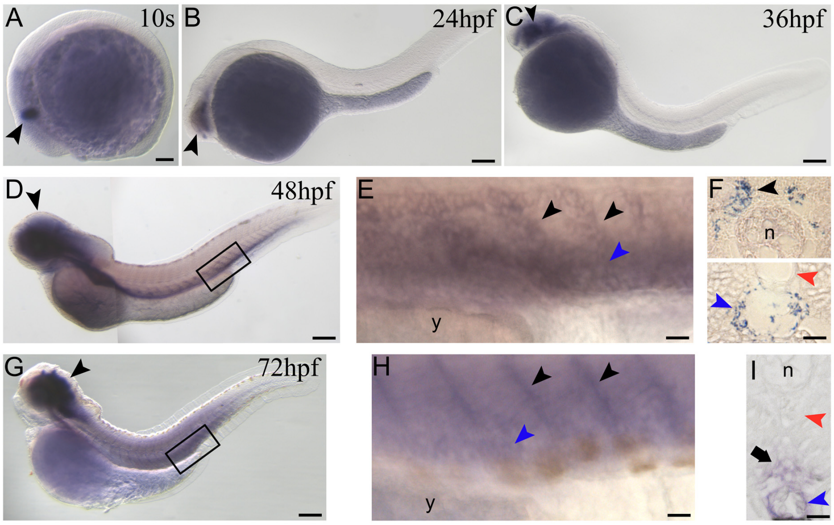

Figure 2. *prox1b* embryonic expression pattern analyzed by *in-situ* hybridization. (A) the first *prox1b* signal appears at 10 somite (s) stage in the central nervous system (CNS) (black arrowhead). (B) at 24hpf and (C) 36 hpf *prox1b* expression continues to be restricted to the CNS of the embryos (black arrowheads). (D) at 48 hpf *prox1b* mRNA is still detectable in the CNS, and is now expressed in the posterior cardinal vein (PCV) and the sprouts emanating from this vessel into the intersegmental space (black box). (E) magnification of the region boxed in D; PCV (blue arrowhead) and vein sprouts (black arrowheads) are indicated. (F) cross sections of 48 hpf-*prox1b*-hybridized embryos. (F, bottom) *prox1b* is expressed in the endothelial cells of the vein wall (blue arrowhead), and not in the dorsal aorta (DA) (red arrowhead). (F, top) *prox1b* signal is also visible on both sides of the trunk (black arrowhead), adjacent to the notochord (n). (G) at 72 hpf *prox1b* expression pattern is comparable to the 48 hpf stage, being the signal detectable in the CNS (black arrowhead), in the PCV and the sprouts emanating from the PCV (black box). (H) magnification of the region boxed in G; PCV (blue arrowhead) and vein sprouts (black arrowheads) are indicated. (I) cross section of a 72 hpf-*prox1b*-hybridized embryo. The endothelial cells of the PCV are still labelled (blue arrowhead), while the signal is completely absent from the DA territory (red arrowhead). *prox1b* is now expressed in the space comprised between the DA and the PCV (arrow), where the TD forms starting from around 72 hpf. y, yolk. Scale bars represent 100 µm (A,B,C,D,G) or 20 µm (E,F,H,I).
doi:10.1371/journal.pone.0013170.g002

vessel into the intersegmental space (Figure 2D,E). The analysis of transversal sections of hybridized embryos revealed that *prox1b* is indeed expressed in the endothelial cells of the vein wall (Figure 2F, bottom), from where lymphatic precursor emerge to migrate towards the horizontal myoseptum region. Later on, according to previous studies, these lymphatic precursors will migrate from the horizontal myoseptum to a position ventral to the dorsal aorta (DA) and contribute to the mature TD [4,14]. Notably, we observed the expression of *prox1b* on both sides of the trunk, adjacent to the notochord, at the level of the horizontal myoseptum (Figure 2F, top). Also interesting, the wall of the DA was not marked by *prox1b* expression (Figure 2F, bottom). At 72 hpf *prox1b* signal was still visible at the level of the intersomitic boundaries (Figure 2G,H) and the PCV (Figure 2G,H,I), and appeared in the space comprised between the DA and the PCV (Figure 2I), where the TD forms starting from around 3 days post-fertilization (dpf) [4,14]. It is noteworthy that *prox1b* medaka ortholog mRNA was not detectable until 3 dpf (34 somite stage) and could be seen exclusively in few territories of the CNS during development [9].

The pattern of expression of zebrafish *prox1b* led us to investigate the possible functional role of the gene in lymphangiogenesis. *prox1b* knockdown produced a lymphatic phenotypes that we evaluated searching for the presence/absence of the TD in fli1:GFP transgenic fish [15] at 5 dpf (Figure 3), the developmental stage at which the TD is already fully formed [4,10]. In comparison to control embryos (Figure 3A,E,I), *prox1b* knockdown resulted in the absence of the TD (Figure 3B,F) in 70% of injected embryos (n = 70) (Figure 3J). Interestingly, the lack of the TD determined by the injection of *prox1b*-MO was always associated to mild to severe cardiac edema (Figure 3M,N), resembling the *prox1a*-lymphatic phenotype previously described [4]. A small percentage of the injected embryos displayed impaired circulation, and heart and trunk defects that did not allowed the observation of the vasculature, and for this reason was not included in the final analysis. The specificity of the lymphatic phenotype induced by *prox1b* knockdown was verified through the coinjection of a *prox1b* full-length mRNA properly mutagenized in the region targeted by the morpholino, which rescued the normal phenotype (Fig 3C,G,K). In order to corroborate the role of *prox1b* in lymphangiogenesis, the expression of *lyve1*, a specific molecular marker for lymphatic endothelial cells [14,16], has been assayed (Figure 4). In comparison to control embryos (Figure 4A,C), *lyve1* expression in the trunk of *prox1b* morphants was weak or completely absent at 48 (80%, n = 30; Figure 4B) and 72 hpf (82%, n = 25; Figure 4D), indicating an impairment of lymphatic development.

To ascertain whether *prox1b* might synergize with *prox1a* to promote lymphangiogenesis, we coinjected the two orthologs specific MOs. The simultaneous knockdown of the two genes did not determine more severe phenotypes or the increase of the number of affected embryos in comparison to the *prox1b*-MO single morphants (data not shown). The attempt to use higher MOs concentrations resulted in acute generalized defects that impeded additional analysis of the morphants, as previously reported for the single *prox1a*–MO injection [10]. However, it is remarkable to notice that the *prox1b*-induced lymphatic phenotype could be rescued by means of coinjection with *prox1a* mRNA. Indeed, 75% of the double injected embryos (n = 75) appeared phenotipically normal with a perfectly formed TD (Figure 3D,H,L), highlighting the evolutionary conservation between the two orthologs.

Altogether these data support the indispensable role of *prox1b* in zebrafish lymphangiogenesis, representing a contribution of basic importance for the consolidation of zebrafish as a valuable lymphangiogenic model.

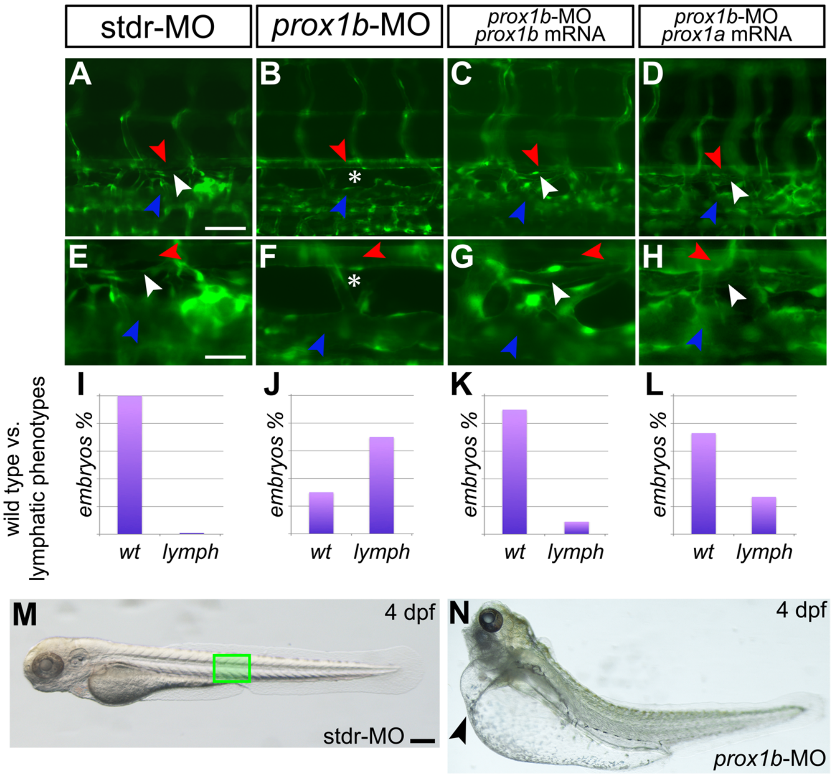

Figure 3. *prox1b* depletion results in the complete loss of the thoracic duct. fli1:GFP expression labels the DA (red arrowheads), the PCV (blue arrowheads), and lymphatic TD (white arrowheads) in 5 dpf embryos. A–D are shown magnified below in E–H. In comparison to control embryos injected with the stdr-MO (A,E), where 100% of the embryos analyzed displays a normal TD (I), the MO directed against *prox1b* (B,F) results in the absence of the TD (asterisks) in 70% of injected embryos (J). (C,G) the specificity of the effect of the *prox1b*-MO is confirmed by the ability of *prox1b* mRNA to rescue the lymphatic phenotype. (K) indeed, MO/mRNA coinjection resulted in about 90% of the embryos showing a normal TD. (D,H) *prox1a* mRNA is able to rescue the lymphatic phenotype induced by *prox1b*-MO injection in about 75% of the embryos analyzed (L). (M) 4 dpf control (stdr-MO) injected embryos compared to the (N) *prox1b* morphant (*prox1b*-MO) at the same developmental stage displaying severe edema (arrowhead). The green box in M indicates the approximate position of the embryo trunk depicted in A–D. Scale bars represent 40 μm (A,B,C,D), 20 μm (E,F,G,H), or 100 μm (M,N).
doi:10.1371/journal.pone.0013170.g003

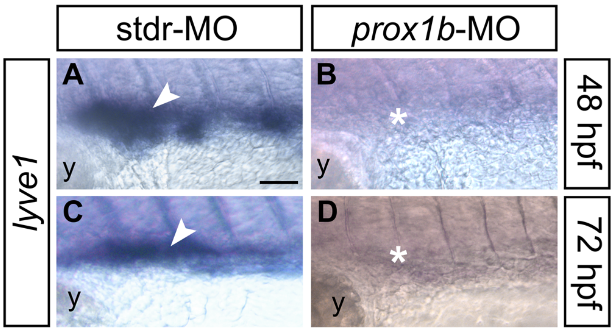

Figure 4. The expression of the lymphatic molecular marker *lyve1* is dramatically reduced in *prox1b* morphants. *lyve1* riboprobe labels developing lymphatic endothelial cells in 48 (A,B), and 72 (C,D) hpf embryos (all lateral views, anterior to the left; the approximate region of the embryo trunk imaged in all panels corresponds to the green box in Figure 3M). In comparison to control embryos injected with the stdr-MO (A,C), that display a normal expression of *lyve1* (white arrowheads), the MO directed against *prox1b* (B,D) results in the absence of *lyve1* signal (white asterisks). y, yolk. Scale bar represents 40 μm.
doi:10.1371/journal.pone.0013170.g004

Methods

Ethics Statement

All embryos were handled according to relevant national and international guidelines.

Fish and Embryos Maintenance

Fish of the AB strain and transgenics for fli:GFP [15] were maintained at 28°C on a 14-hr light/10-hr dark cycle. Embryos were collected by natural spawning and staged according to Kimmel and colleagues [17].

prox1b identification and cDNA cloning

Zebrafish *prox1b* gene was identified through *in-silico* search using *prox1a* full-length cDNA as a bait. Two gene specific primers (*prox1b*F: 5′-CACCGCCATATAACACCACA-3′, and *prox1b*R: 5′-TTAACTGCTGGCCCTCCTGT-3′) have been used to amplify the full-length cDNA. The 3′ UTR have been obtained through RACE technique while the 5′ UTR has been identified searching the GenBank ESTs database.

Whole mount in-situ hybridization (WISH)

WISH was carried out as previously described [18,19]. Histological analysis of previously hybridized embryos was carried out on 8 μm sections.

Injections

Injections were carried out on 1- to 2-cell stage embryos. To repress *prox1b* mRNAs translation, an ATG-targeting morpholino (MO) was synthesized (Gene Tools): 5′-GGGAATCCA-TAGCCTCCTTTTCTGT-3′. *prox1b*-specific MO was used at the concentration of 6 ng per embryo in 1X Danieau buffer (pH 7,6). To repress *prox1a* mRNA translation, a *prox1a*-specific MO was used at the concentration of 8 ng per embryo, as previously reported [4,12,20,21]. As control, we injected 8 ng per embryo of a standard control MO (stdr-MO). MO-mRNA double injection experiments were conducted using 300 pg of capped mRNA per embryo together with the above reported amount of the MO of interest. For live microscopy observation, 5 dpf fli1:GFP transgenic larvae have been anesthetized and monitored under a fluorescent microscope. For the *in-vivo* test of the specificity of *prox1b*-MO, 300 pg per embryo of the *prox1b*-GFP sensor plasmid have been coinjected with 8 ng of *prox1b*-MO or stdr-MO, respectively (Figure S1). The presence/absence of the GFP signal has been monitored under a fluorescent microscope from 24 to 48 hpf.

Supporting Information

Figure S1 prox1b-MO specifically reduces prox1b mRNA translation. For the in-vivo test of the specificity of prox1b-MO, a prox1b-GFP sensor has been generated. (A) The construct contains 96 bp of the 5′ UTR, and the first 432 bp of the prox1b coding sequence (Nprox1b) fused with the GFP open reading frame. The blue bar indicates the region of the mRNA targeted by the prox1b-MO. The construct, obtained by PCR, has been cloned into the pTargeT expression vector (Promega) and used for injection experiments. (B) GFP-positive cells in the trunk (inset and arrowheads) and (C) in the yolk epithelium (arrowheads) are visible following coinjection of the sensor and the stdr-MO. (D) The complete absence of fusion protein expression when the sensor is coinjected with prox1b-MO confirms the specificity of action of the morpholino. Scale bar represents 100 μm.

Found at: doi:10.1371/journal.pone.0013170.s001 (6.42 MB TIF)

Author Contributions

Conceived and designed the experiments: LDG. Performed the experiments: LDG AP Ag. Analyzed the data: LDG. Wrote the paper: LDG.

References

1. Hassan B, Li L, Bremer KA, Chang W, Pinsonneault J, et al. (1997) Prospero is a panneural transcription factor that modulates homeodomain protein activity. Proc Natl Acad Sci U S A 94: 10991–10996.
2. Wigle JT, Oliver G (1999) Prox1 function is required for the development of the murine lymphatic system. Cell 98: 769–778.
3. Ny A, Koch M, Schneider M, Neven E, Tong RT, et al. (2005) A genetic Xenopus laevis tadpole model to study lymphangiogenesis. Nat Med 11: 998–1004.
4. Yaniv K, Isogai S, Castranova D, Dye L, Hitomi J, et al. (2006) Live imaging of lymphatic development in the zebrafish. Nat Med 12: 711–716.
5. Bixel MG, Adams RH (2008) Master and commander: continued expression of Prox1 prevents the dedifferentiation of lymphatic endothelial cells. Genes Dev 22: 3232–3235.
6. Wigle JT, Harvey N, Detmar M, Lagutina I, Grosveld G, et al. (2002) An essential role for Prox1 in the induction of the lymphatic endothelial cell phenotype. EMBO J 21: 1505–1513.
7. Mäkinen T, Norrmén C, Petrova TV (2007) Molecular mechanisms of lymphatic vascular development. Cell Mol Life Sci 64: 1915–1929.
8. Postlethwait JH (2007) The zebrafish genome in context: ohnologs gone missing. J Exp Zool B Mol Dev Evol 308: 563–577.
9. Deguchi T, Fujimori KE, Kawasaki T, Ohgushi H, Yuba S (2009) Molecular cloning and gene expression of the prox1a and prox1b genes in the medaka, Oryzias latipes. Gene Expr Patterns 9: 341–347.
10. Küchler AM, Gjini E, Peterson-Maduro J, Cancilla B, Wolburg H, et al. (2006) Development of the zebrafish lymphatic system requires VEGFC signaling. Curr Biol 16: 1244–1248.
11. Glasgow E, Tomarev SI (1998) Restricted expression of the homeobox gene prox 1 in developing zebrafish. Mech Dev 76: 175–178.
12. Pistocchi A, Bartesaghi S, Cotelli F, Del Giacco L (2008) Identification and expression pattern of zebrafish prox2 during embryonic development. Dev Dyn 237: 3916–3920.
13. Tomarev SI, Zinovieva RD, Chang B, Hawes NL (1998) Characterization of the mouse Prox1 gene. Biochem Biophys Res Commun 248: 684–689.
14. Hogan BM, Bos FL, Bussmann J, Witte M, Chi NC, et al. (2009) Ccbe1 is required for embryonic lymphangiogenesis and venous sprouting. Nat Genet 41: 396–398.
15. Lawson ND, Weinstein BM (2002) *In vivo* imaging of embryonic vascular development using transgenic zebrafish. Dev Biol 248: 307–318.
16. Flores MV, Hall CJ, Crosier KE, Crosier PS (2010) Visualization of embryonic lymphangiogenesis advances the use of the zebrafish model for research in cancer and lymphatic pathologies. Dev Dyn 239: 2128–2135.
17. Kimmel CB, Ballard WW, Kimmel SR, Ullmann B, Schilling TF (1995) Stages of embryonic development of the zebrafish. Dev Dyn 203: 253–310.
18. Thisse C, Thisse B, Schilling TF, Postlethwait JH (1993) Structure of the zebrafish snail1 gene and its expression in wild-type, spadetail and no tail mutant embryos. Development 119: 1203–1215.
19. Jowett T, Lettice L (1994) Whole-mount in situ hybridizations on zebrafish embryos using a mixture of digoxigenin- and fluorescein-labelled probes. Trends Genet 10: 73–74.
20. Liu YW, Gao W, The HL, Tan JH, Chan WK (2003) Prox1 is a novel coregulator of Ff1b and is involved in the embryonic development of the zebra fish interrenal primordium. Mol Cell Biol 23: 7243–7255.
21. Pistocchi A, Gaudenzi G, Carra S, Bresciani E, Del Giacco L, et al. (2008) Crucial role of zebrafish prox1 in hypothalamic catecholaminergic neurons development. BMC Dev Biol 8: 27. doi:10.1186/1471-213X-8-27.